

AD-A170 062

DEVELOPMENT OF ULTRASONIC MODELLING TECHNIQUES FOR THE
STUDY OF SEISMIC M. (U) MASSACHUSETTS INST OF TECH
CAMBRIDGE EARTH RESOURCES LAB M N TOKSOZ ET AL. MAR 86

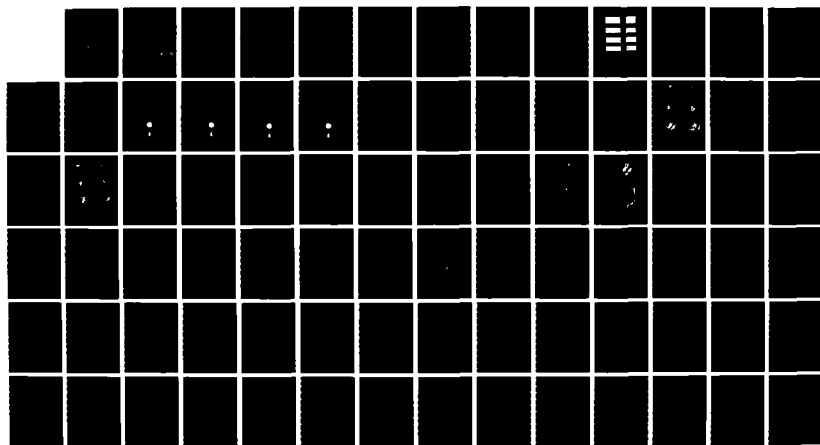
1/1

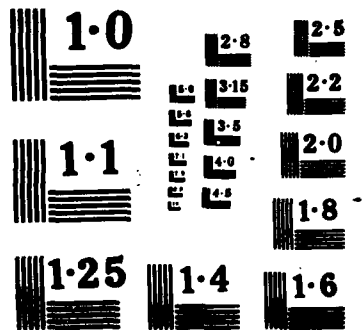
UNCLASSIFIED

AFGL-TR-86-0078 F19628-83-K-0027

F/G 0/11

NL





AFGL-TR-88-0078

DEVELOPMENT OF ULTRASONIC MODELLING TECHNIQUES
FOR THE STUDY OF SEISMIC WAVE SCATTERING DUE TO
CRUSTAL INHOMOGENEITIES

M. Nafi Toksöz
Anton M. Dainty
Edmond E. Charrette

Earth Resources Laboratory
Department of Earth, Atmospheric, and Planetary Sciences
Massachusetts Institute of Technology
Cambridge, MA 02139

Final Report
13 April 1983 - 30 September 1985

March 1986

Approved for public release; distribution unlimited

AIR FORCE GEOPHYSICS LABORATORY
AIR FORCE SYSTEMS COMMAND
DEPARTMENT OF THE AIR FORCE
HANSCOM AFB, MA 01731

DTIC
ELECTE
JUL 23 1986
S B

DTIC FILE COPY

CONTRACTOR REPORTS

This technical report has been reviewed and is approved for publication.

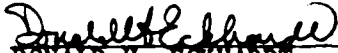


JANET C. JOHNSTON
Contract Manager



HENRY A. OSSING
Chief, Solid Earth Geophysics Branch

FOR THE COMMANDER



DONALD H. ECKHARDT
Director
Earth Sciences Division

This report has been reviewed by the ESD Public Affairs Office (PA) and is releasable to the National Technical Information Service (NTIS).

Qualified requesters may obtain additional copies from the Defense Technical Information Center. All others should apply to the National Technical Information Service.

If your address has changed, or if you wish to be removed from the mailing list, or if the addressee is no longer employed by your organization, please notify AFGL/DAA, Hanscom AFB, MA 01731-5000. This will assist us in maintaining a current mailing list.

Do not return copies of this report unless contractual obligations or notices on a specific document requires that it be returned.

Unclassified

APA 170062

SECURITY CLASSIFICATION OF THIS PAGE (When Data Entered)

REPORT DOCUMENTATION PAGE		READ INSTRUCTIONS BEFORE COMPLETING FORM
1 REPORT NUMBER AFGL-TR-86-0078	2 GOVT ACCESSION NO.	3 RECIPIENT'S CATALOG NUMBER
4 TITLE (and Subtitle) DEVELOPMENT OF ULTRASONIC MODELLING TECHNIQUES FOR THE STUDY OF SEISMIC WAVE SCATTERING DUE TO CRUSTAL INHOMOGENEITIES		5 TYPE OF REPORT & PERIOD COVERED Final Report 13 April 1983-30 September
		6 PERFORMING ORG REPORT NUMBER
7 AUTHOR(s) M. Nafi Toksöz Anton M. Dainty Edmond E. Charrette III		8 CONTRACT OR GRANT NUMBER(s) F19628-83-K-0027
9 PERFORMING ORGANIZATION NAME AND ADDRESS Earth Resources Laboratory Dept. of Earth, Atmospheric, and Planetary Sciences M.I.T., Cambridge, MA 02139		10 PROGRAM ELEMENT PROJECT, TASK AREA & WORK UNIT NUMBERS 61102F 2309G2AP
11 CONTROLLING OFFICE NAME AND ADDRESS Air Force Geophysics Laboratory Hanscom AFB, Massachusetts 01731 Monitor/Janet C. Johnston/LWH		12 REPORT DATE March 1986
		13 NUMBER OF PAGES 79
14 MONITORING AGENCY NAME & ADDRESS (if different from Controlling Office)		15 SECURITY CLASS. of this report Unclassified
		16A DECLASSIFICATION/DOWNGRADING SCHEDULE
15 DISTRIBUTION STATEMENT (of this Report) Approved for public release; distribution unlimited		
17 DISTRIBUTION STATEMENT (of the abstract entered in Block 20, if different from Report)		
18 SUPPLEMENTARY NOTES		
19 KEY WORDS (Continue on reverse side if necessary and identify by block number) ultrasonic modelling, scattering, finite difference method, topographic effects, crustal inhomogeneities, surface waves		
20 ABSTRACT (Continue on reverse side if necessary and identify by block number) The scattering of Rayleigh waves from surface features has been investigated using three-dimensional ultrasonic models at frequencies near 1 MHz and two-dimensional finite difference calculations. The models were constructed of aluminum blocks and an aluminum powder-epoxy composite of lower density and seismic velocity. The aluminum has similar seismic velocities and density to igneous and metamorphic rocks while the composite is similar to sedimentary materials. Kilometers in the earth are scaled to millimeters in the models;		

985

DD FORM 1473

EDITION OF 1 NOV 65 IS OBSOLETE

Unclassified

SECURITY CLASSIFICATION OF THIS PAGE (When Data Entered)

Unclassified

SECURITY CLASSIFICATION OF THIS PAGE(When Data Entered)

this makes 1 MHz in the models equivalent to 1 Hz in the earth, typical of the frequencies observed in regional seismograms. Relief on the models was a few millimeters, the order of a wavelength. The relief was restricted to an isolated circular mesa of composite on a metal block and an isolated circular depression both unfilled and filled with composite. Calculations were made for similar situations by the finite difference method; comparisons indicated a general similarity in the seismograms, allowing us to use the finite difference calculations to gain physical insight into the scattering process. Topography alone produces attenuation due to scattering into reflected surface waves and body waves. Adding low velocity composite to the model considerably changes this picture. The Rayleigh wave energy is strongly trapped in the low velocity material on the surface and produces strong reverberation as it bounces around in the mesa or valley. This effect is suppressed to a certain extent by the attenuating properties of the composite. Analogs of this type of behaviour seem to exist in observed regional seismograms.

Unclassified

SECURITY CLASSIFICATION OF THIS PAGE(When Data Entered)

TABLE OF CONTENTS

REPORT DOCUMENTATION PAGE WITH ABSTRACT	1
I. INTRODUCTION	4
II. ULTRASONIC EXPERIMENTS	6
III. NUMERICAL MODELING	17
IV. COMPARISON BETWEEN PHYSICALLY AND NUMERICALLY MODELED RESULTS	57
APPENDIX: NUMERICAL ANALYSIS	62
REFERENCES	79



Accession	
NTIS	✓
IC T	
Announcement	
Justification	
Distribution	
Availability	
Avail	
Sp	
A-1	

I. INTRODUCTION

Crustal inhomogeneities cause scattering of seismic waves. The effect is particularly pronounced for regional seismograms (distance range 0 - 1000 km) in the frequency band 0.5 - 5 Hz. Surface wave phases such as Rg and Lg are especially affected; such phases are of potential importance for monitoring a Complete Test Ban Treaty (Blandford, 1981). Two methods that can be used to examine this problem quantitatively are physical modeling and the use of theoretical calculations of the elastic wavefield. In this report we attack the problem using these methods.

The original thrust of the investigation was physical modeling at ultrasonic frequencies. The models were constructed out of nickel plates, aluminum blocks and an aluminum powder-epoxy mixture; the metals have elastic velocities and densities similar to igneous and metamorphic rocks commonly found in the crust and the aluminum powder-epoxy mixture is an analog of relatively soft sedimentary rocks such as might be found as valley fill in the Basin and Range province. These analogies are further strengthened by the low attenuation of the metals, similar to igneous and metamorphic rocks, and the high attenuation of the aluminum powder-epoxy mixture, similar to soft sedimentary rocks. Due to these similarities, to scale the model correctly it is only necessary to require that the ratio of the wavelength to the size of the inhomogeneities be the same in the model as in the earth. Since wavelength is proportional to frequency, if a typical model frequency of 1 MHz is to be compared to a frequency of 1 Hz on regional seismograms then millimeters in the model will scale to kilometers in the earth. Using these principles models of tens of centimeters across with surface features a few millimeters in height were constructed. In this investigation we have concentrated on the scattering of Rayleigh waves by surface features such as mesas and sedimentary basins; this should provide an analog to the effects on the fundamental mode Rg.

Initially, under a previous AFGL contract (F19628-81-K-0039), we attempted to build complex models that were analogs to real topographic and geologic situations. The attempt was successful, but the complexity of the resulting seismograms made it difficult to acquire a conceptual understanding of the scattering process. Such an understanding is important to avoid the considerable labor of building a new model for every new area examined and also to allow estimation of effects where some aspect of the geology such as the depth of a sedimentary basin is uncertain. Two approaches to this problem were explored in this investigation. One is to examine simpler models in which the scattering process is less complicated and hence more easily understood. The other is to compare the seismograms from the physical models with theoretical seismograms, in this investigation calculated by the finite difference technique. The theoretical calculations are inevitably for simpler cases than the experimental results, but nonetheless can give great physical insight into the interpretation of the physical ultrasonic modeling.

II. ULTRASONIC EXPERIMENTS

Introduction

In this chapter ultrasonic experiments carried out under this contract and relevant to it will be discussed. All of the experiments examine Rayleigh wave scattering from simple shapes. Simple shapes are used because of our previous experience with more complicated models where difficulty was encountered in interpreting the complicated seismograms that resulted. Thus the focus of our effort has been on elucidating the underlying factors influencing Rayleigh wave scattering from topography by examining simple shapes in conjunction with finite difference calculations to be presented in a subsequent chapter. First a brief presentation of two-dimensional scattering from rectangular mesas is given; this study was carried out under a previous contract (F19628-81-K-0039) but is summarised here because of its relevance to the project, especially the finite difference modeling. Then some three-dimensional models of circular mesas and basins are presented.

Two-dimensional Mountains

A report has already been given on these experiments, so only a brief description will be given (see Nathman, 1980). The medium consisted of a nickei plate with one edge cut into the shape of a rectangular mesa. Magnetostrictive transducers (Chamuel, 1977) were used to couple into this edge; the dominant mode of elastic motion observed was Rayleigh waves with a velocity of 2.776 km/sec and a peak wavelength of nearly 14 mm. Receiving transducers were placed either between the source transducer and the mesa to receive the direct and reflected Rayleigh waves or on the other side of the mesa from the source transducer to record the transmitted waves. Some examples are shown in Figure 1.

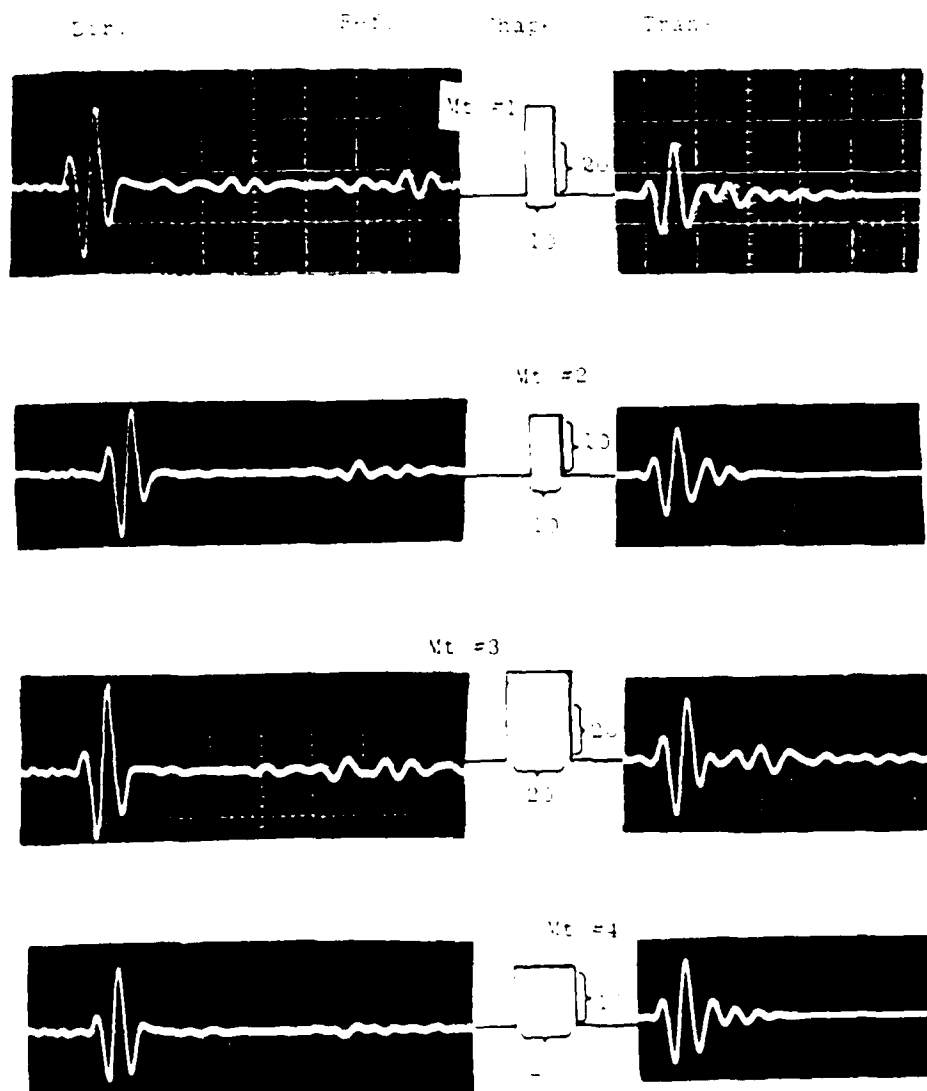


Fig 1: Rayleigh waves reflected and transmitted through two-dimensional mesas. Dimensions are in millimeters; Dir and Refl refer to the pulse before striking the mesa and after reflection, observed on the same side of the mesa as the source. Trans refers to the transmitted pulse observed on the far side of the mesa from the source.

The reflected and transmitted pulse differ from the source ("Direct") pulse in two ways. They are of lesser amplitude: Figure 2 shows the magnitude of the reflection and transmission (displacement) coefficients as a function of frequency. It should be noted that a considerable fraction of the incident Rayleigh energy is scattered into body waves at the mesa and lost from the Rayleigh wave field. The other effect is the presence of reverberation, most easily seen after the main transmitted pulse. This suggests that the Rayleigh energy can travel several different paths when it interacts with the mesa; travel time analysis indicates that the main transmitted pulse seen in Figure 1 is due to energy that "tunnelled" through the base of the mesa, while the later reverberations are due in part to energy that followed the surface over the mesa. This question will be examined again in the discussion of the finite difference results.

Three-dimensional Models

Three-dimensional experiments with circular mesas and basins have been carried out. The experimental set up for one of the mesa experiments is shown in Figure 3. The mesa was built on the surface of a circular aluminum block and was made of an epoxy-aluminum powder mixture. The piezoelectric source transducer produced a Rayleigh wave pulse with a dominant wavelength of 1.23 mm (Bullitt and Toksöz, 1985) and the receiving transducer was placed on the other side of the mesa so as to provide a scattering angle (measured at the center of the mesa) between 0° (directly opposite the source) and 40° . All of the mesa and basin models had the same lateral dimensions shown in Figure 3 with different height or depth of the feature. The basins were either left unfilled or were filled with the epoxy-aluminum powder mixture, simulating a low velocity sedimentary fill.

Seismograms observed for the model of Figure 3 are shown in Figure 4 for scattering angles of 0° , 10° , 20° , 30° and 40° . Again substantial reverberation is observed. Travel times are indicated for the following phases: rp, Rayleigh wave from the source converted

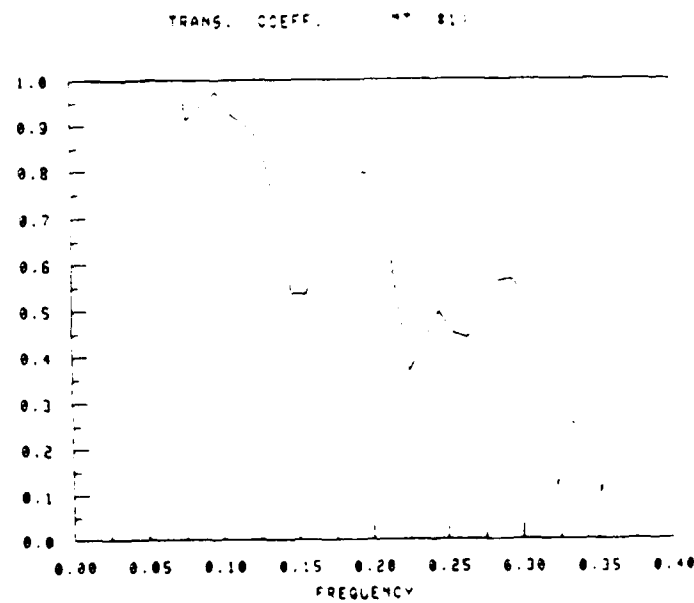
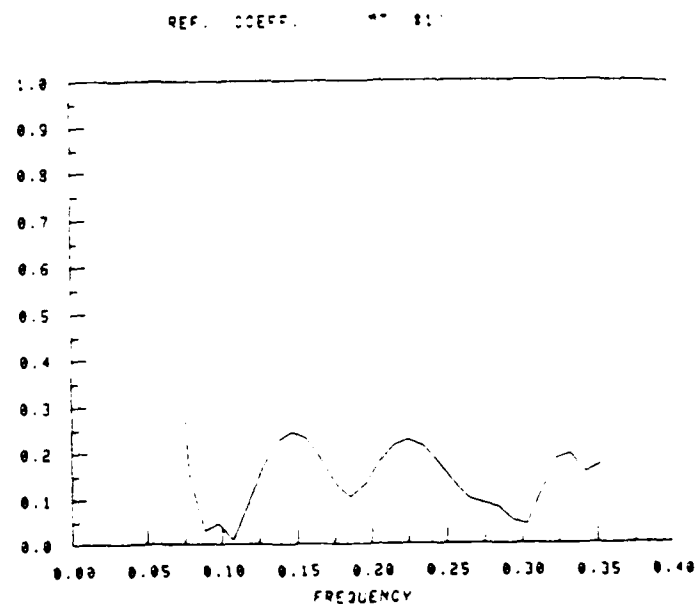


Fig 2: Displacement reflection and transmission coefficients as a function of frequency (MHz) for case 1, Fig 1.

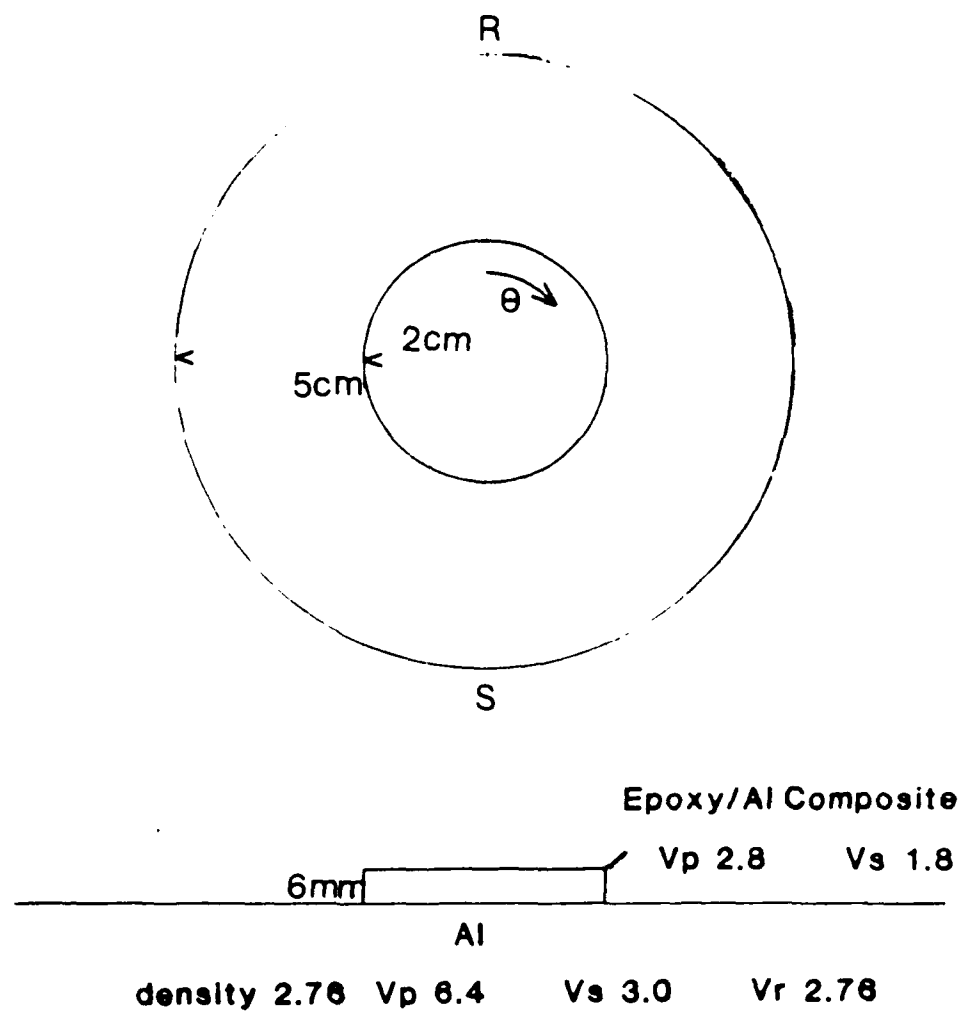


Fig 3: Geometry of three-dimensional models. R indicates the position of the receiver and S the source.

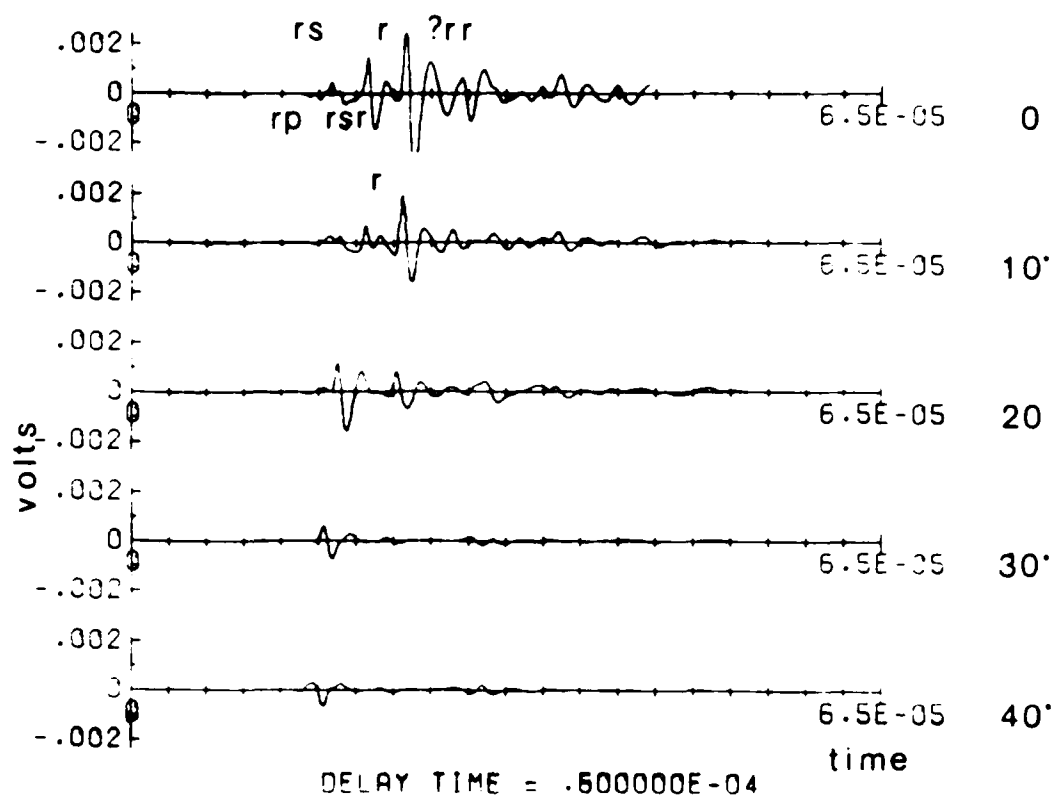


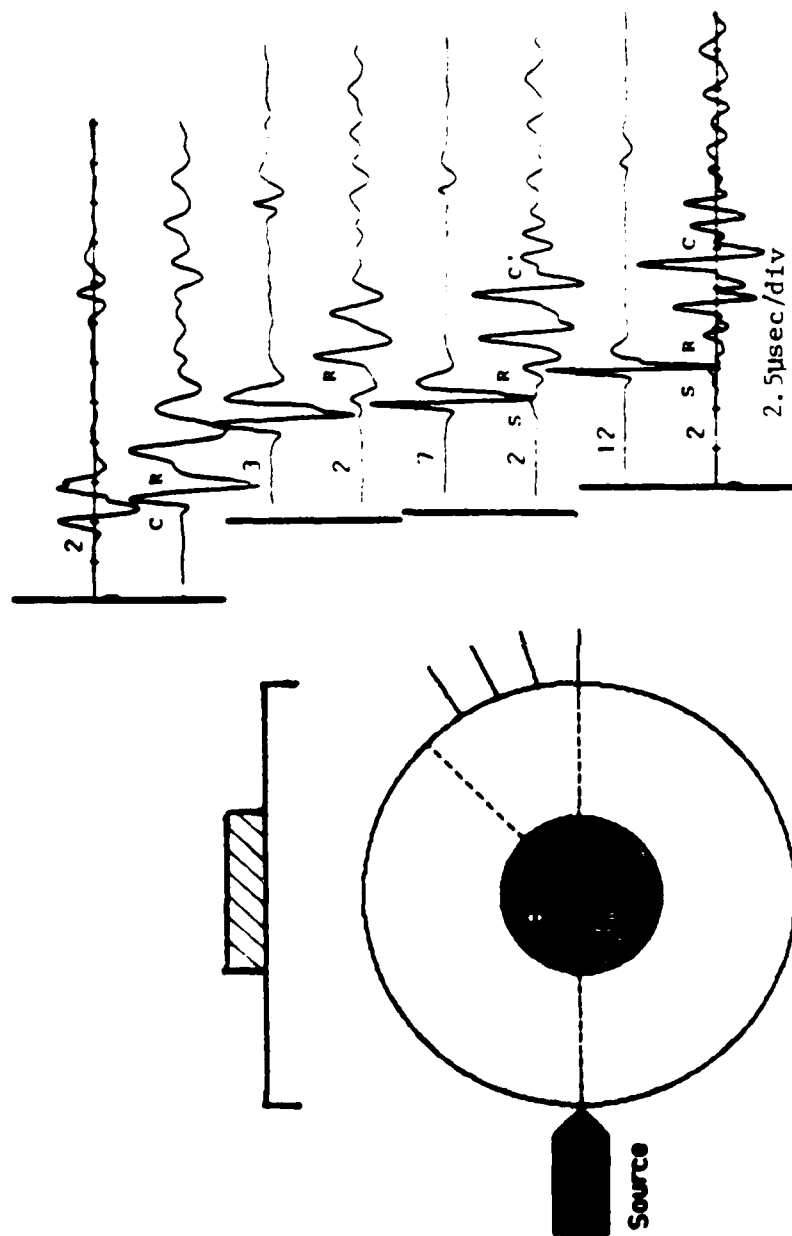
Fig 4: Seismograms for model of Fig 3. Time is in seconds; output of receiving transducer is shown. Scattering angle is indicated on the right. See text for discussion. Mesa is about 5λ high.

to P at the mesa; rs, Rayleigh wave converted to S; rsr, Rayleigh wave converted to S upon striking the mesa, travelling through the mesa as S, converting back to Rayleigh on leaving the mesa (this wave type was the dominant type for the two-dimensional mesas); r, Rayleigh wave that travelled over the mesa from source to receiver; rr, Rayleigh wave that reverberated once within the mesa. All of the seismograms are shown to the same scale. Note the loss of amplitude as the scattering angle increases and the change in relative importance of different phases at different angles.

Figures 5 - 8 show similar experiments for two mesas of different heights and two basins. In these figures a control trace, i.e. the trace observed with no mesa or basin present, is shown for comparison and the traces are amplitude scaled. For the basins, the filled and unfilled (with epoxy-aluminum powder mixture) are shown. In all cases reverberation is observed; for the basins the effect seems to be stronger for the filled case than the unfilled case.

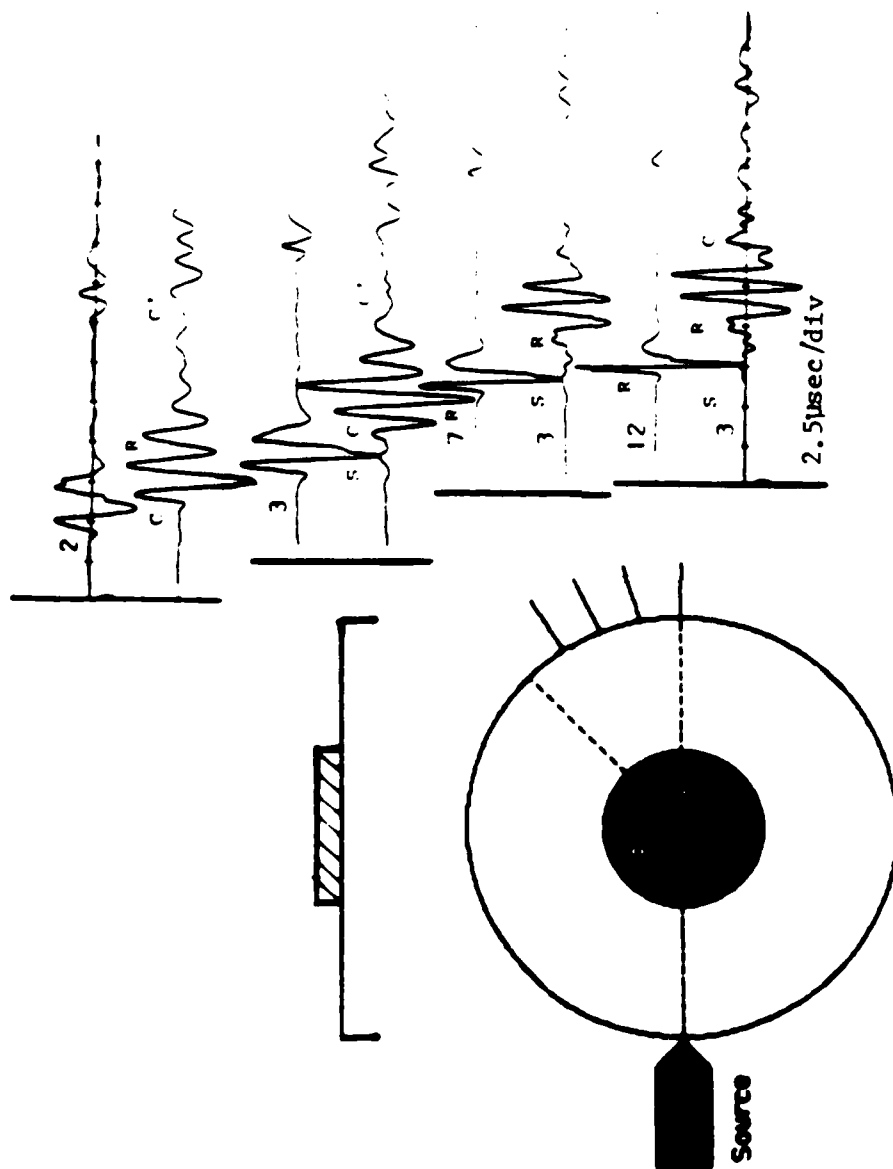
Summary

Rayleigh wave propagation across mesas and basins has been observed for two- and three-dimensional ultrasonic models. The height or depth of the features was of the same order as the wavelength. Two effects were consistently seen. Firstly, the amplitude was diminished upon crossing the structure. For the two-dimensional models it was clear that considerable energy was being scattered into body waves; presumably, the same was true for the three-dimensional case, although signal to noise problems precluded the observation of the scattered body waves. The other important effect was the presence of reverberations due to converted and reflected waves within the structure.



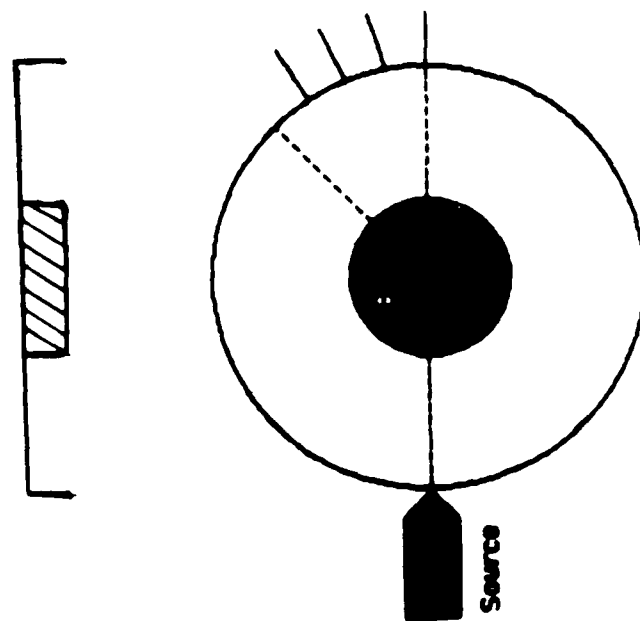
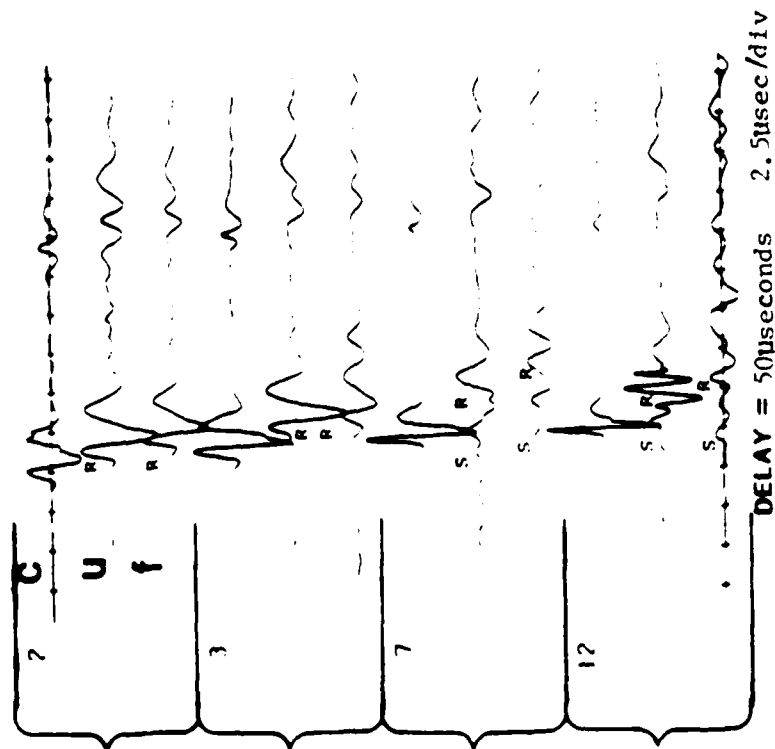
EFFECTS OF A 3mm MESA OF LOW VELOCITY MATERIAL ON THE TRANSMISSION OF RAYLEIGH WAVES. THE TOP TRACE OF EACH TWO TRACE GROUP IS THE CONTROL TRACE.

Fig 5: Mesa is $\approx 2\lambda$ high. Control trace is the seismogram without the mesa. Numbers next to each trace are reduction factors; to find the true relative amplitude multiply the trace amplitude by the factor.



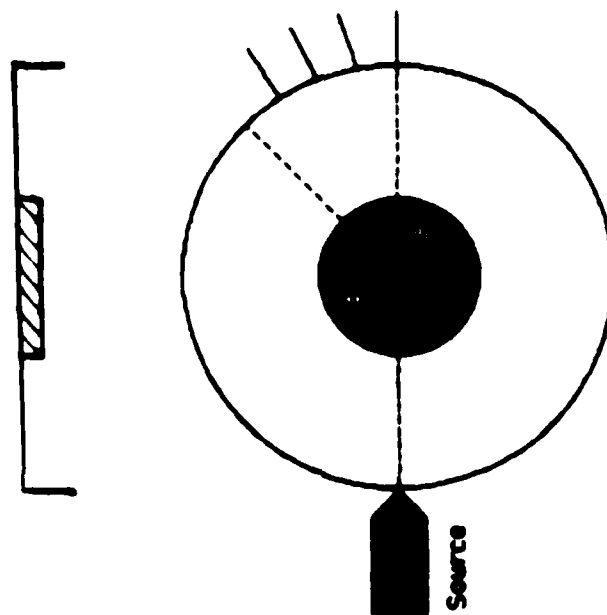
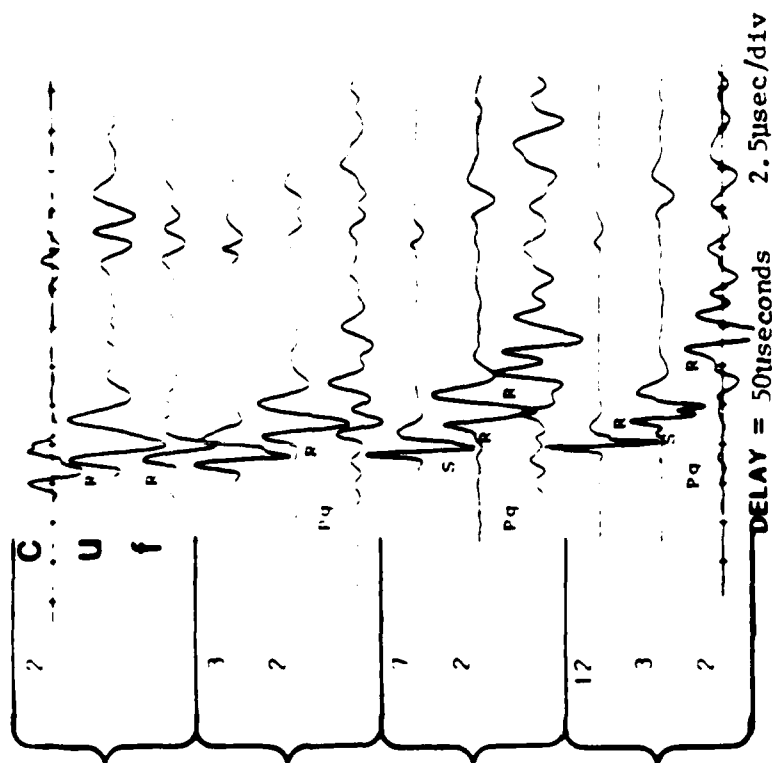
EFFECTS OF A 1.5mm MESA OF LOW VELOCITY MATERIAL ON THE TRANSMISSION OF RAYLEIGH WAVES. THE TOP OF EACH TWO TRACE GROUP IS THE CONTROL TRACE.

Fig 6: Mesa is $\approx 1 \lambda$ high.



EFFECTS OF A 3mm BASIN, BOTH UNFILLED (u) AND FILLED (f), ON TRANSMITTED RAYLEIGH WAVES. PLOTTED AS A FUNCTION OF ANGLE, WITH CONTROL TRACE (c).

Fig 7: Basin is $\approx 2\lambda$ deep.



EFFECTS OF A 1.5mm BASIN, BOTH UNFILLED (u) AND FILLED (f), PLOTTED WITH CONTROL TRACE, AS A FUNCTION OF ANGLE

Fig 8: Basin is $\approx 1\lambda$ deep.

III. NUMERICAL MODELING

Introduction

The finite difference method was used to duplicate the experiments performed above. Inherent storage limitations imposed by our computer facilities prevented us from modeling three-dimensional geometries, but there were aspects of the three-dimensional models which we were able to investigate. The finite difference theory, applications and references comprise a complete sub-field in applied mathematics, and therefore will not be presented here. Instead a detailed outline of the relevant theory, stability and accuracy is given in an Appendix. We will use this section to discuss the results obtained through the use of the finite difference technique.

Variations in velocity and topography have significant effects on the amount of energy scattered by incident Rayleigh waves. In general, larger scale variations in topography or velocity produce larger coefficients of reflection and smaller transmission coefficients. Also, sharp discontinuities are more efficient scatterers of energy than rounded features (Bullitt and Toksöz, 1985). The Figures presented in this chapter are of two types. Figure 10, for example, is a compilation of synthetic seismograms, made by storing both the horizontal and vertical nodal displacements at each time step. Figure 11 shows snapshots in time, where the displacements in the grid are stored at a single time step. In other words, Figure 10 represents the time varying displacement history of a series of points on the free surface and Figure 11 represents a spatial varying displacement map of the entire model, at a single instant in time.

There are many subtleties involved in interpreting both types of diagrams. In Figure 10, an outline of the model being investigated is presented at the bottom of the page. The small square boxes on the surface of the model can be thought of as seismometers. They

are the points on the model where the displacement histories were stored to make the synthetic seismograms. The top part of the diagram is a series of synthetic seismograms, tracing both horizontal and vertical components of the displacement vector. The horizontal and vertical components are plotted at the same scale; the horizontal displacements are smaller than the corresponding vertical displacements. This difference is due to the source function, which is prescribed as having approximately twice as much amplitude in the vertical direction as the horizontal direction. The vertical axis represents time, time is zero at the bottom and increases upwards. The horizontal axis represents distance in units of wavelength. Note the arrival time of the incident Rayleigh wave, (R), migrates upward as the Rayleigh wave moves away from its original location. Then after hitting the scatterer, it is partially reflected, (R'), partially transmitted, (R), and partially scattered to an S wave, (s). The locus of points connecting the first arrivals of a wave will always be steeper for slower moving waves. Since in a constant velocity medium, the incident, reflected and transmitted phases of a wave travel at the same speed, the slopes of these three arrival time curves should all be consistent. This is a useful criteria in identifying wave types, and scattering relationships.

In Figure 11 the displacement fields are captured at successive time steps. The displacement at each grid point is indicated by a line whose length is proportional to the displacement and whose orientation is in the direction of the displacement vector. The waves are marked using the same convention described above. Note for shear waves (s), where the particle displacement is perpendicular to the direction of propagation, the horizontal displacement amplitudes are highest in the part of the wavefront which is traveling vertically. For P waves (p) the situation is the opposite, high horizontal displacement amplitudes occur in the part of the wavefront which is propagating horizontally. Rayleigh waves (R) travel more slowly than P and S waves and typically have higher amplitudes which decrease exponentially with depth. Thus they are most readily

identified at or near the surface.

Step Discontinuities

As mentioned in the previous chapter, the orientation of our investigation was to study simple shapes, then after identifying the important relationships the model was made more complex. In this vein, the step discontinuity was studied first. The coefficients of reflection and transmission were found to depend on both the ratio of the step height to the wavelength and the step direction. Six cases were studied, three having a Rayleigh wave incident on a downstep and three involving a Rayleigh wave traveling up a step.

Downstep:

Step Height = $(1/2)\lambda$:	Figure 9
Step Height = 1λ :	Figures 10, 11
Step Height = $(3/2)\lambda$:	Figure 12

Upstep:

Step Height = $(1/2)\lambda$:	Figure 13
Step Height = 1λ :	Figures 14, 15
Step Height = $(3/2)\lambda$:	Figure 16

In the downstep cases the incident Rayleigh wave travels from left to right. It strikes the upper corner and is partially transmitted (R) partially reflected (R') and partially scattered to an S wave (s). The corner point acts as a point scatterer, that is the S wave moves circularly away from the corner as if the corner was a source. The transmitted portion of the Rayleigh wave continues down the step and scatters in the same manner at the lower corner. The resulting radiation pattern of the S waves is a superposition of the waves from the two corner points, causing a complex interference pattern. There are lobes in the wavefront where energy is concentrated and other portions of the wave front where the energy is greatly diminished. The location of these lobes is a function of step height: Figure 11 shows the case of a one wavelength high step, illustrating the points made

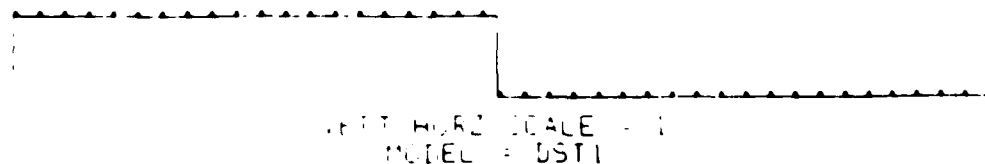
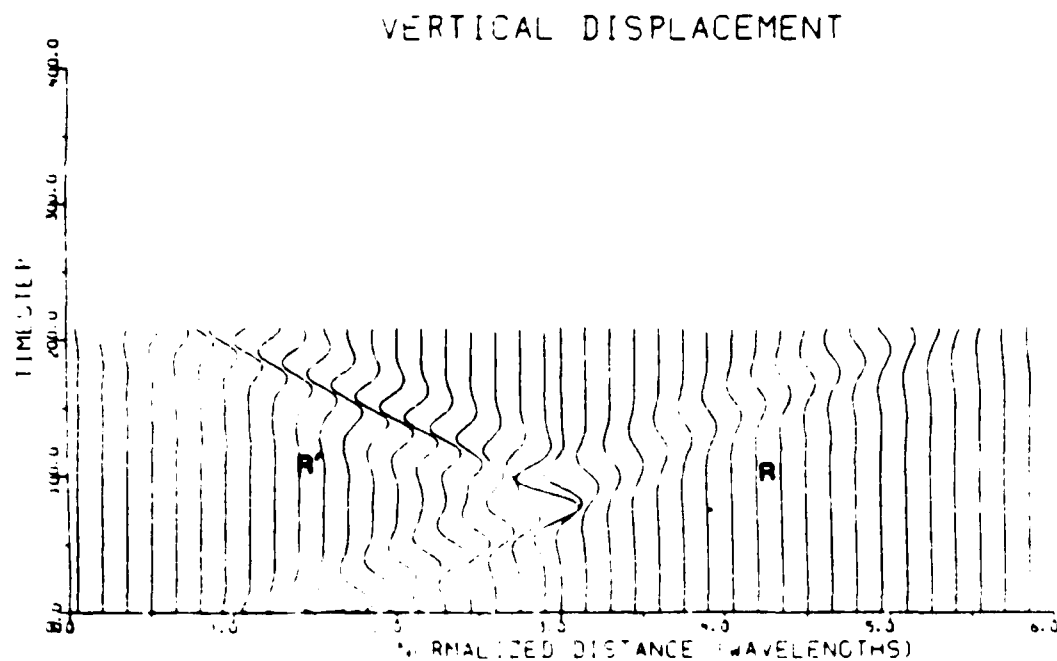
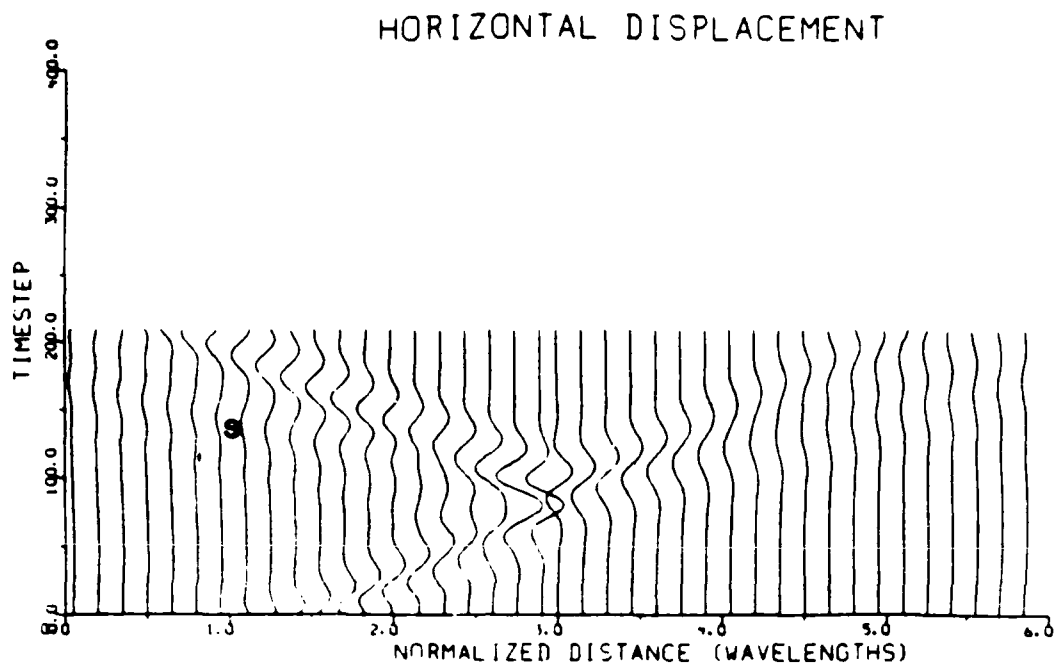


Fig 9: Synthetic surface seismograms for a Rayleigh Wave incident on a $1/2\lambda$ homogeneous downstep geometry. Incident and transmitted Rayleigh wave, (R), reflected Rayleigh wave, (R'), and Rayleigh converted to shear wave, (s) are all present.

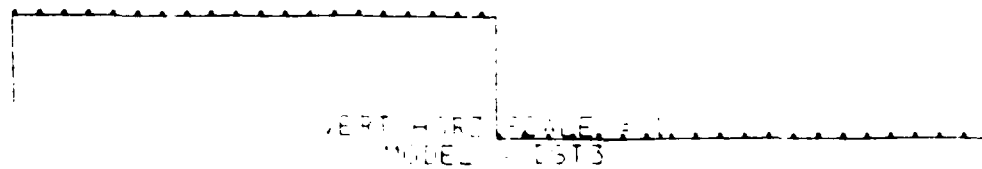
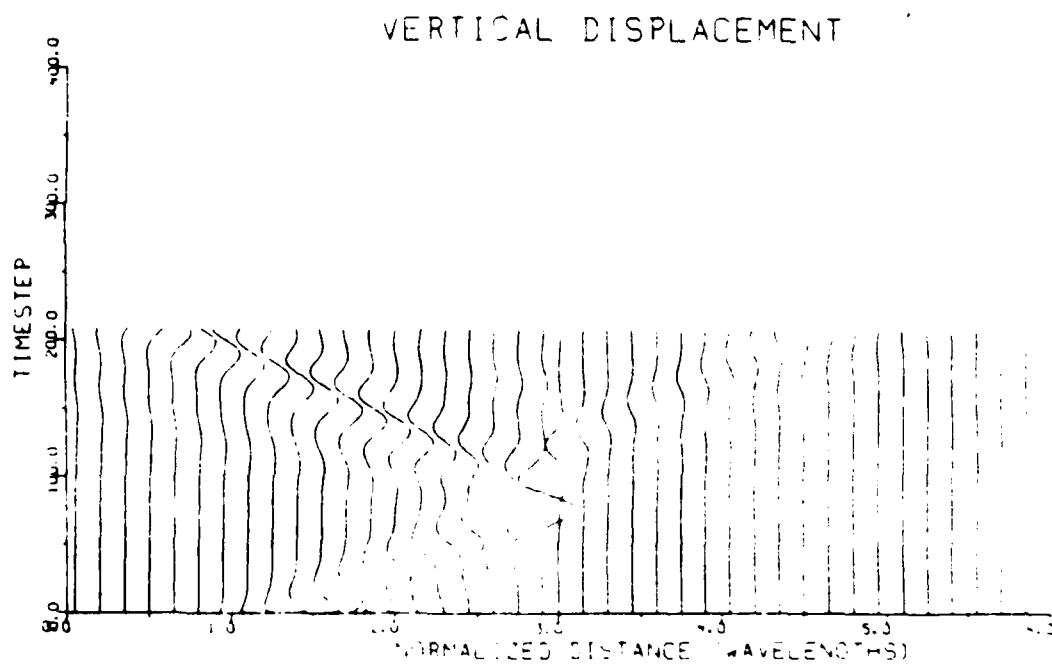
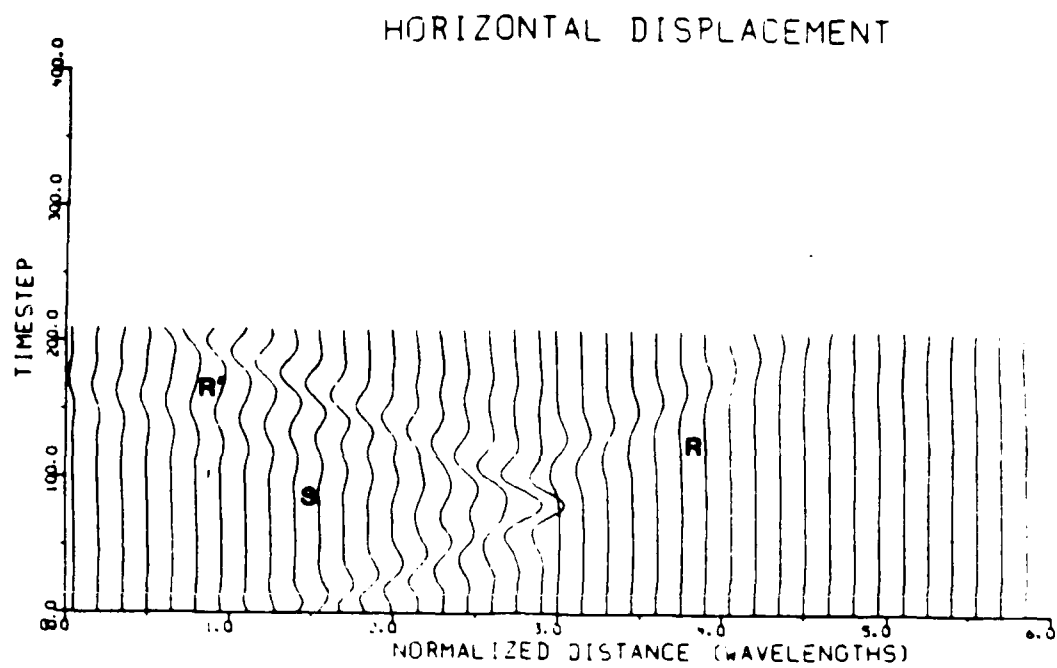


Fig 10: Synthetic surface seismograms for a Rayleigh Wave incident on a 1λ homogeneous downstep geometry.

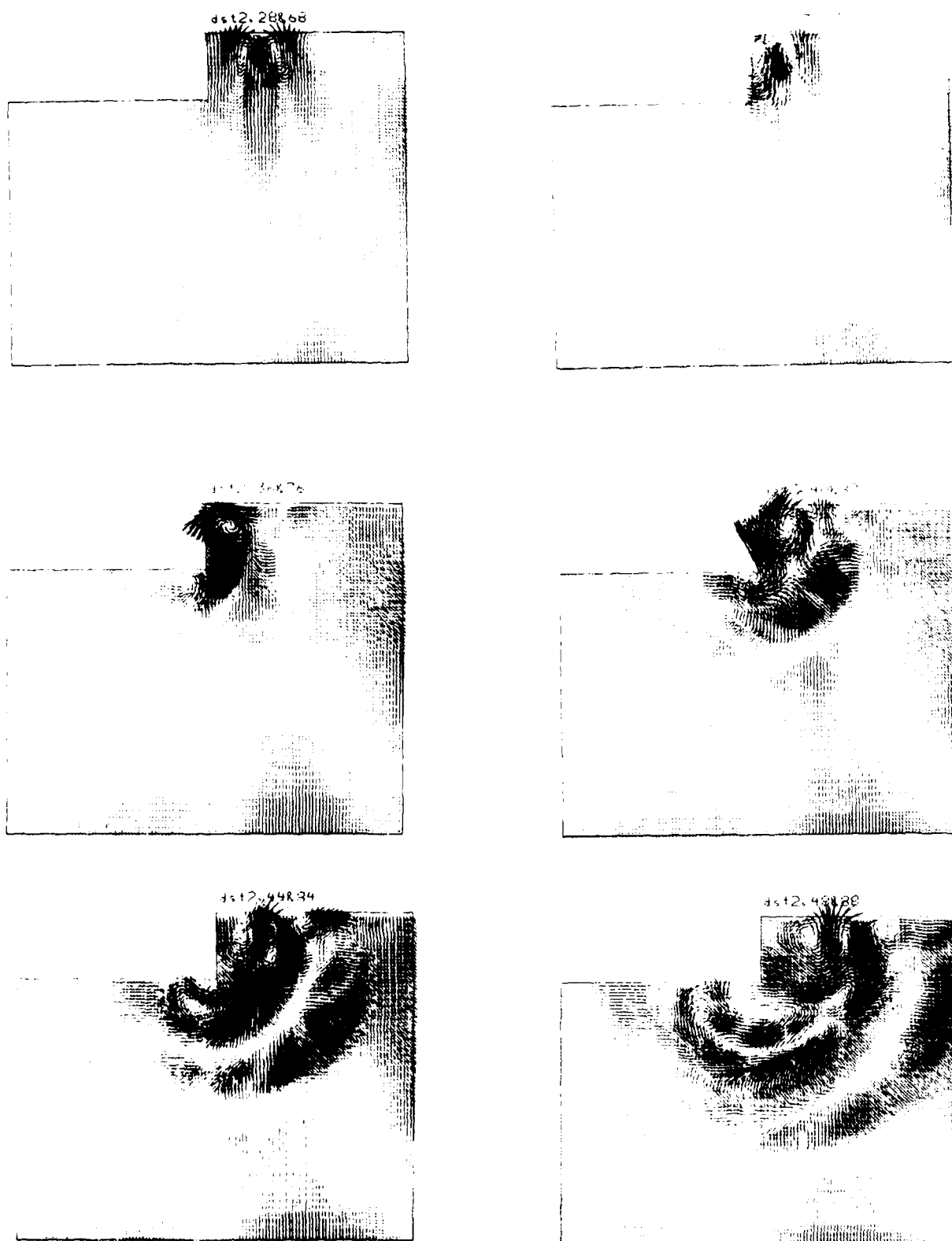
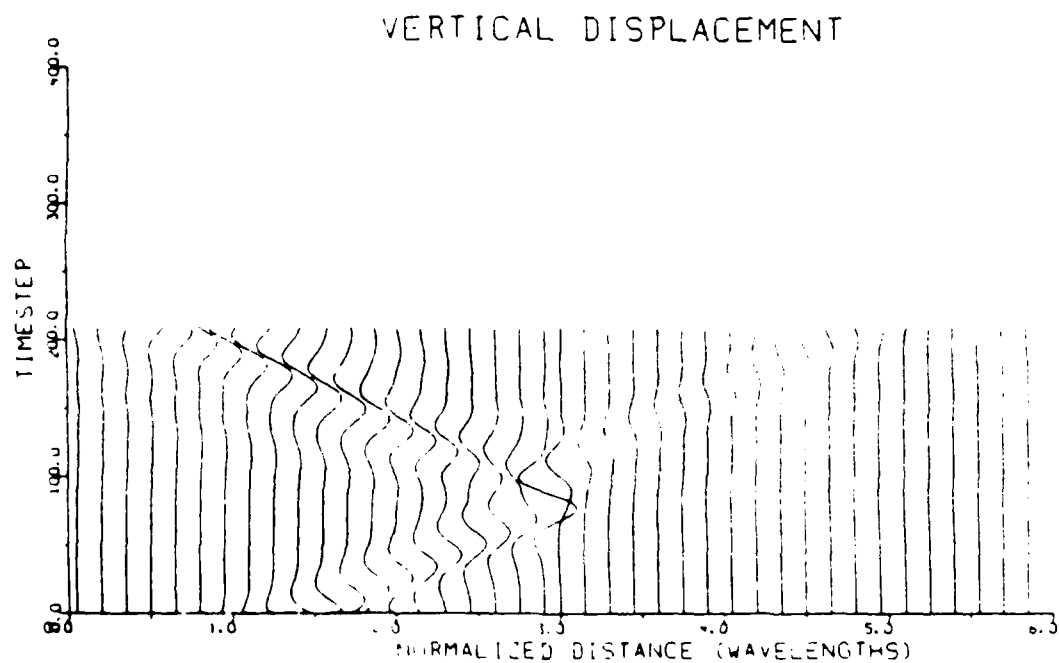
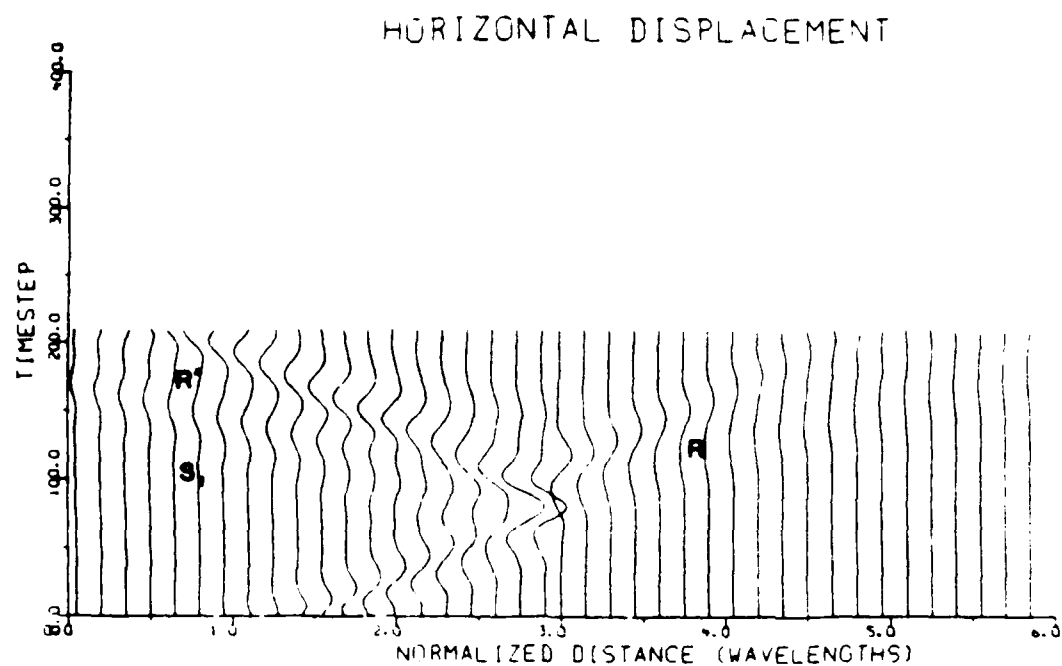
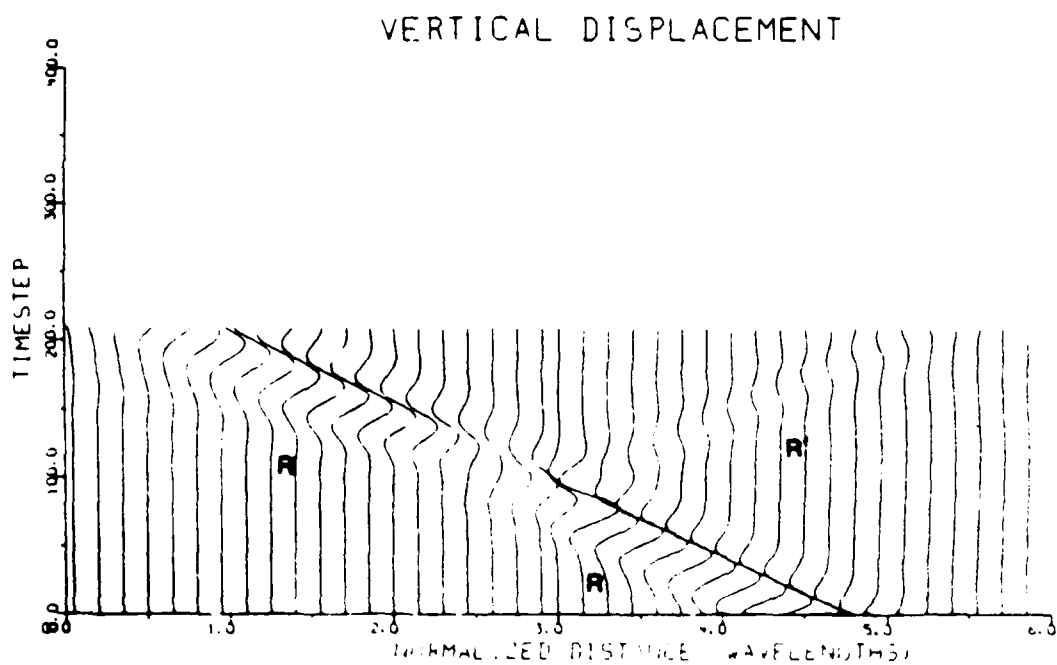
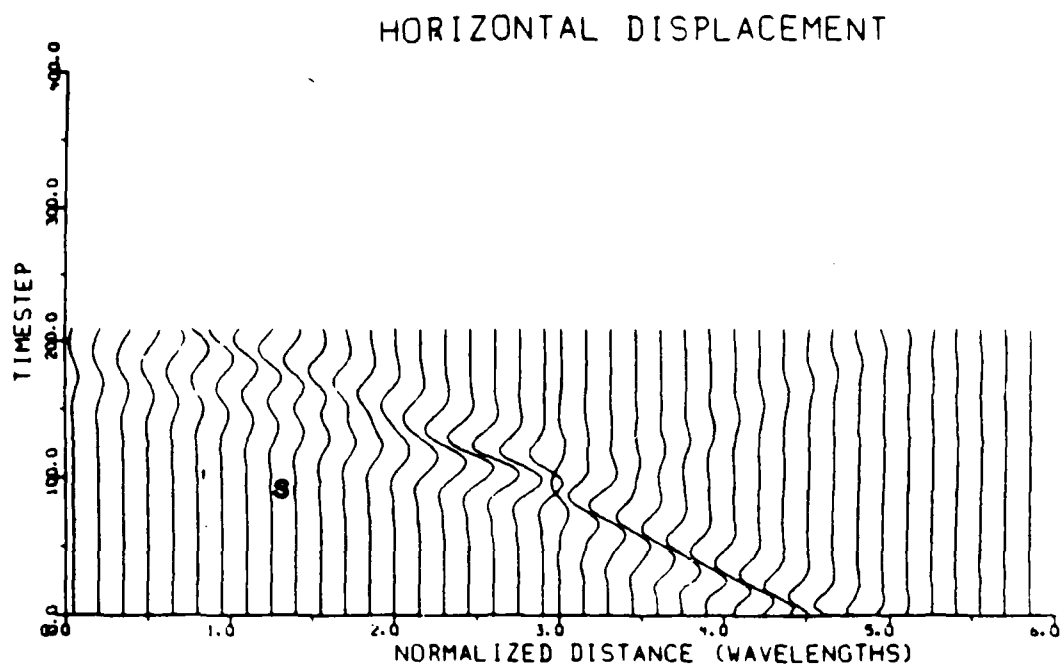


Fig 11: Snapshots of displacements at various times for the 1λ homogeneous downstep geometry. Time increases left to right and downward; at each grid point the displacement vector is represented by an oriented line. Note superposition of the two shear waves radiating from the corner points.



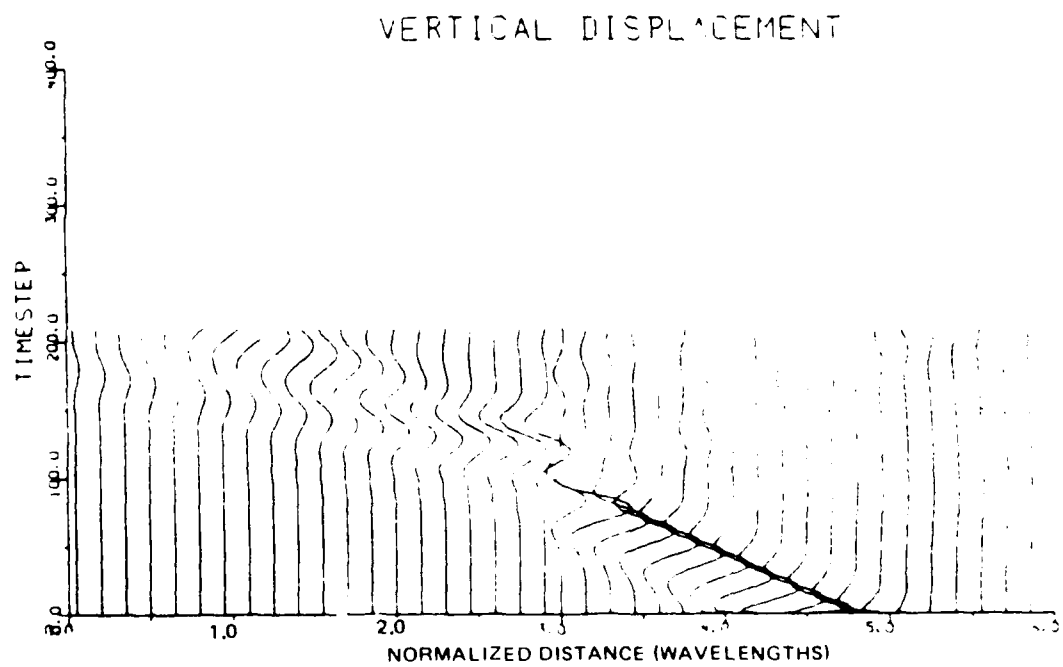
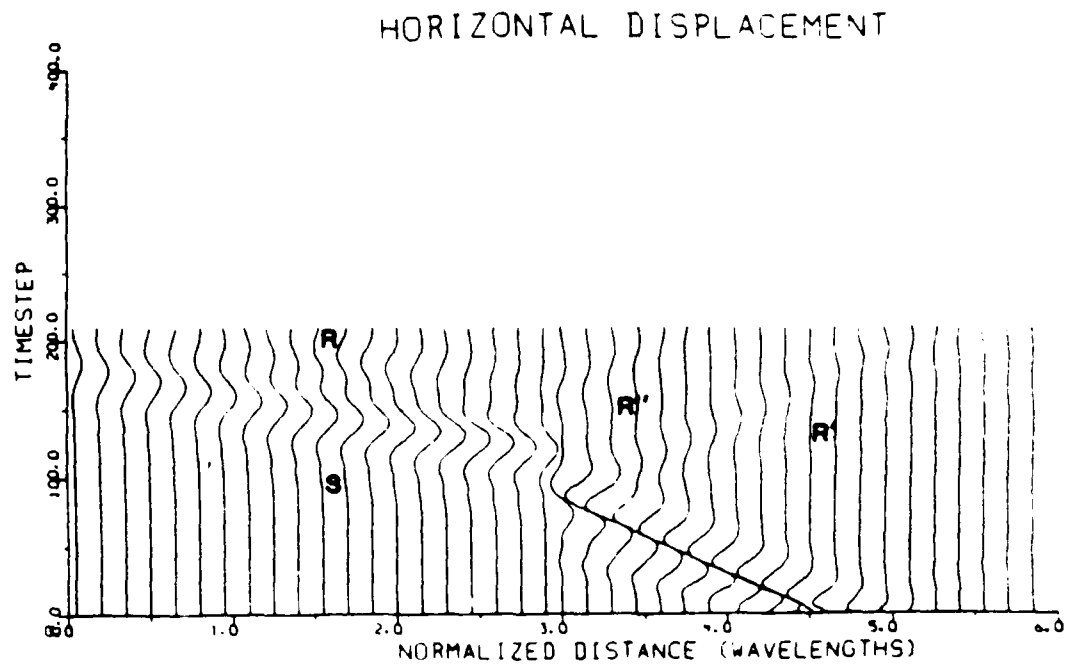
VERT. HORIZ SCALE = 1
MODEL = DST2

Fig 12: Synthetic surface seismograms for a Rayleigh Wave incident on a $3/2\lambda$ homogeneous downstep geometry.



VERT. HORZ. SCALE = 1
MODEL = UST1

Fig 13: Synthetic surface seismograms for a Rayleigh Wave incident on a $1/2\lambda$ homogeneous upstep geometry.



VERT. HORIZ SCALE = 1
MODEL = GST3

Fig 14: Synthetic surface seismograms for a Rayleigh Wave incident on a 1λ homogeneous upstep geometry.

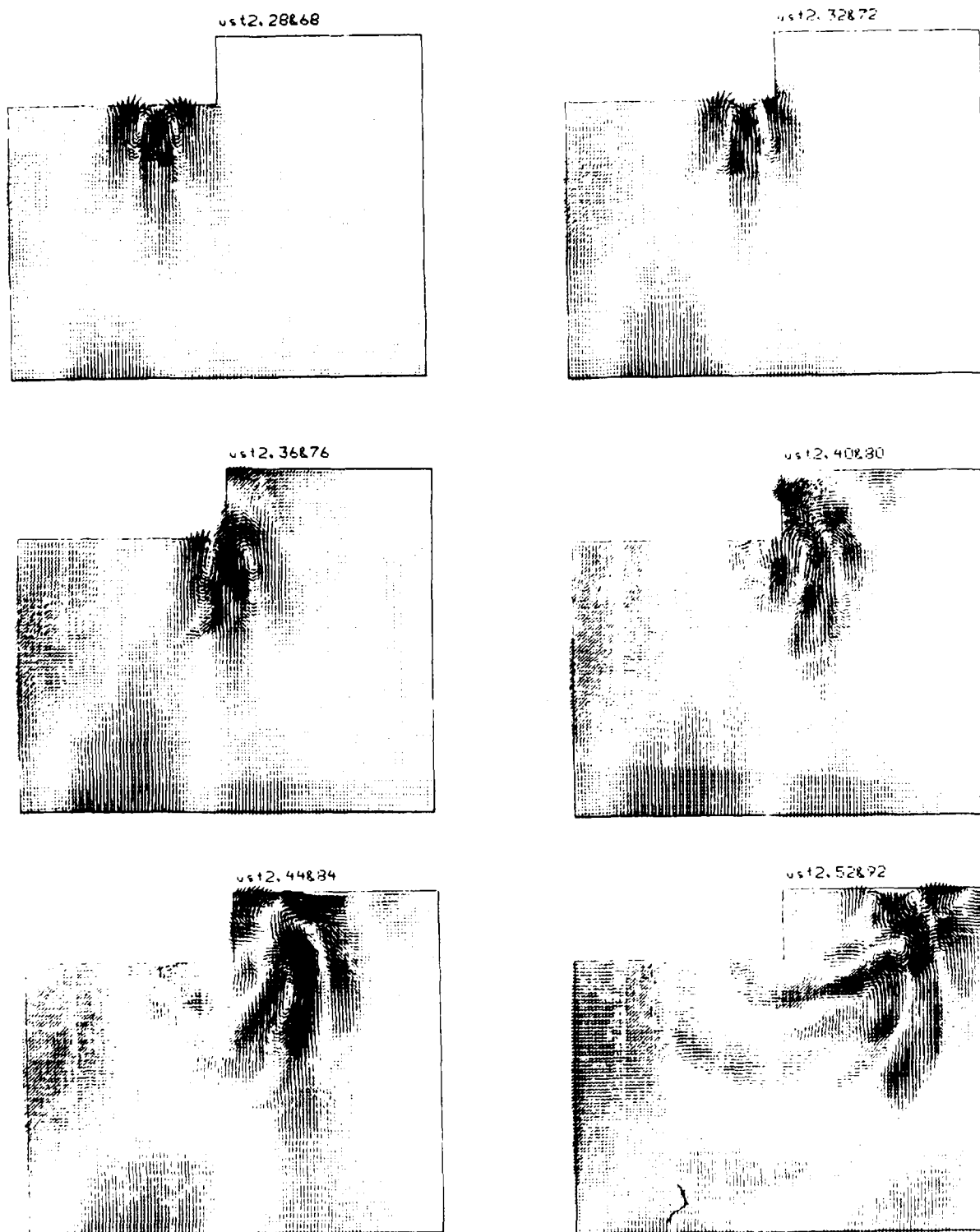


Fig 15: Snapshots of displacements at various times for the 1λ homogeneous unstep geometry.

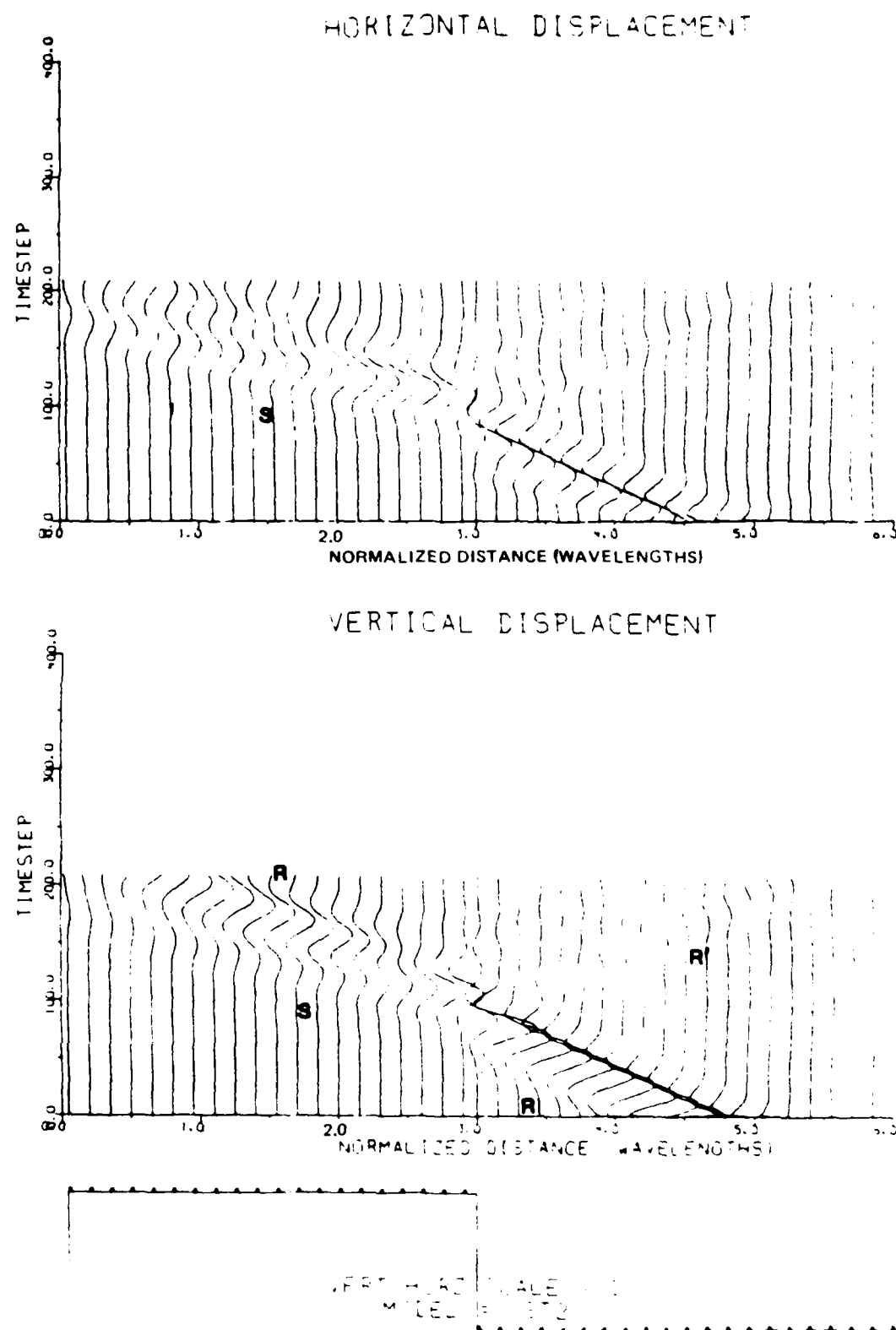


Fig 16: Synthetic surface seismograms for a Rayleigh Wave incident on a $3/2\lambda$ homogeneous upstep geometry.

above. The amount of energy transmitted and reflected by the step is directly related to the step height. As step size increases less Rayleigh wave energy is transmitted, more is reflected and more is scattered into body (S) waves. These relations may be seen by comparing Figures 9, 10 and 12.

Figures 13 - 16 show Rayleigh waves climbing steps of various heights. Here, the incident wave is traveling from right to left. When the surface wave strikes the lower edge of the step, the nature of the scattering is different from the case of the downstep. A larger proportion of the Rayleigh wave is converted to an S wave at the first corner. This S wave travels straight ahead into the medium not evenly distributed in amplitude about the corner, but with the majority of the energy within $\pm 30^\circ$ of the horizontal. The transmitted portion of the Rayleigh wave travels up the vertical face and is again scattered into an S wave at the upper corner. Note in the last frame of Figure 15 the S wave (velocity = 3.2 km/s) pulls away from the bottom of the Rayleigh wave (velocity = 3.0 km/s).

Comparing the two cases, the Rayleigh wave reflection and transmission coefficients appear to be approximately equal for the upstep and downstep cases for the same step height. Therefore, the amount of energy scattered into the model in the form of body waves, mainly S, must be equal. The radiation patterns for the two incidence directions, however, are very different. Energy is scattered to S waves by an upstep geometry in a narrow band around the horizontal, while in a downstep geometry energy is scattered approximately isotropically from the two corner points causing lobes of high and low energy around the wavefront.

Unfilled and Filled Valleys

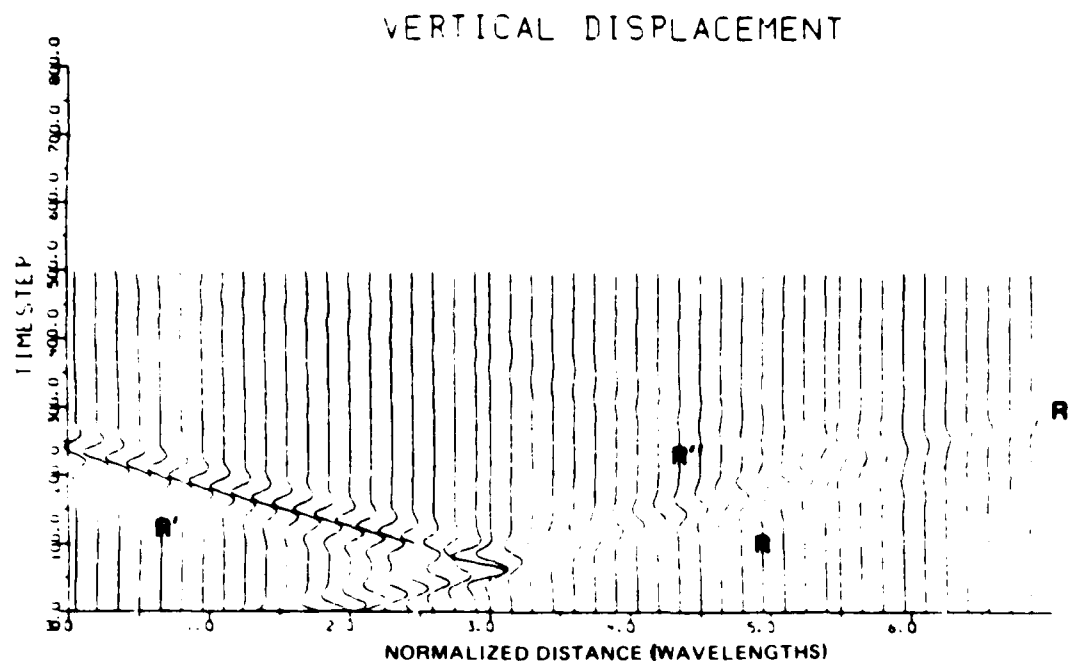
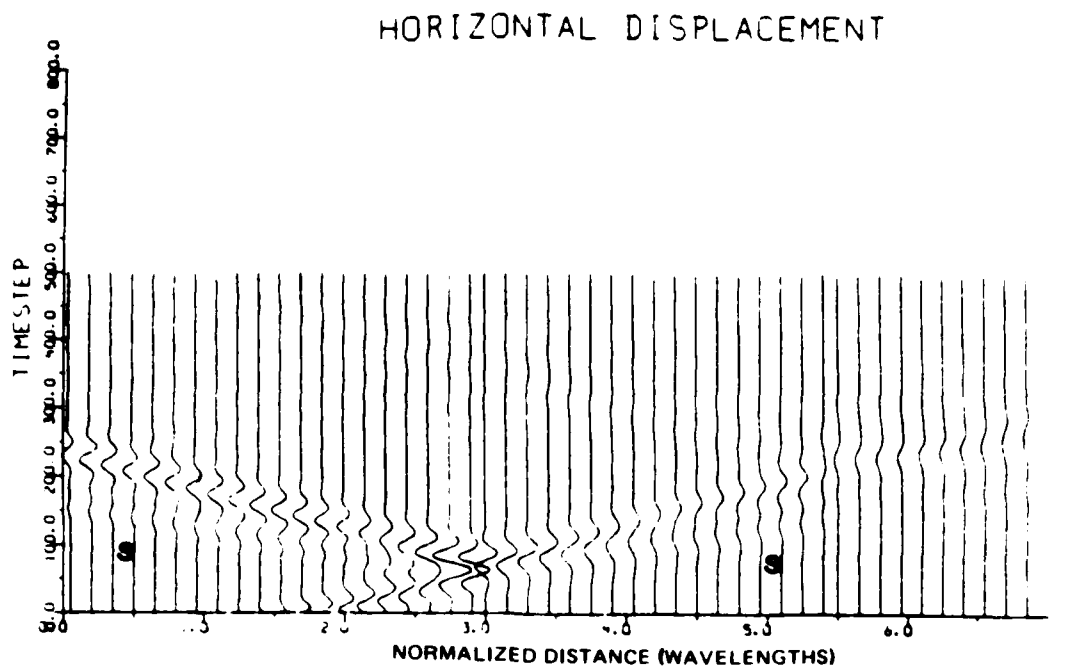
Unfilled and filled valleys were investigated using both physical and numerical techniques. As discussed earlier, numerical modeling was limited to two dimensions, while

physical modeling was extended to three dimensions. In comparing the results of these two modeling techniques, it must be kept in mind that waves traveling over three-dimensional wave paths are not modeled by the numerical technique. However, many of the arrivals observed in the physical model are seen in the numerical model.

Valleys of four depths, $(1/2)\lambda$, 1λ , $(3/2)\lambda$ and 2λ , were modeled. An empty valley is simply a downstep followed by an upstep. As such, one would expect that observations made for simple steps would describe the present problem and that is, in fact, correct. All the features described above are evident in the unfilled valley geometry, as shown by Figures 17 - 21. The incident Rayleigh wave strikes the downside of the trench, is partially reflected, (R'), partially transmitted, (R), and partially scattered to an S wave (s). The Rayleigh wave continues this process around all four of the corners; each time the transmitted Rayleigh wave becomes weaker, thus each scattered phase becomes weaker.

The areas inside the black boxes in Figures 22 - 26 were then filled with low velocity materials having S wave velocity $\beta_f = .44 \times \beta_{HS}$, where β_{HS} is the S wave velocity in the half space. The propagation pattern of the incident Rayleigh wave changes considerably. The amplitude of the reflected Rayleigh wave is much smaller if the valley is filled, and the conversion of surface wave energy to body wave energy is more complex. There are no longer corners to act as point scatterers, and the wavefront entering the slow velocity medium is severely distorted. The deepest filled valley, Figures 25 and 26, offers the clearest view of the scattering pattern. There are other important observations:

- (1) Note the amplitude of the Rayleigh wave, (R), increases as the surface wave enters the slower medium. This occurs because the wavelength of the surface wave decreases in the slower medium, but the energy of the wave stays approximately constant; this point is made most convincingly in Figure 26. This is exactly the same effect as the increase in amplitude of a plane elastic wave crossing an interface at



VERT. HORIZ. SCALE = 1
MODEL = 1.0/1.1

Fig 17: Synthetic surface seismograms for a Rayleigh wave incident on a $1/2\lambda$ deep unfilled straight walled valley in a homogeneous medium. Notice Rayleigh wave reflections at the near, (R'), and far, (R''), side of the valley.

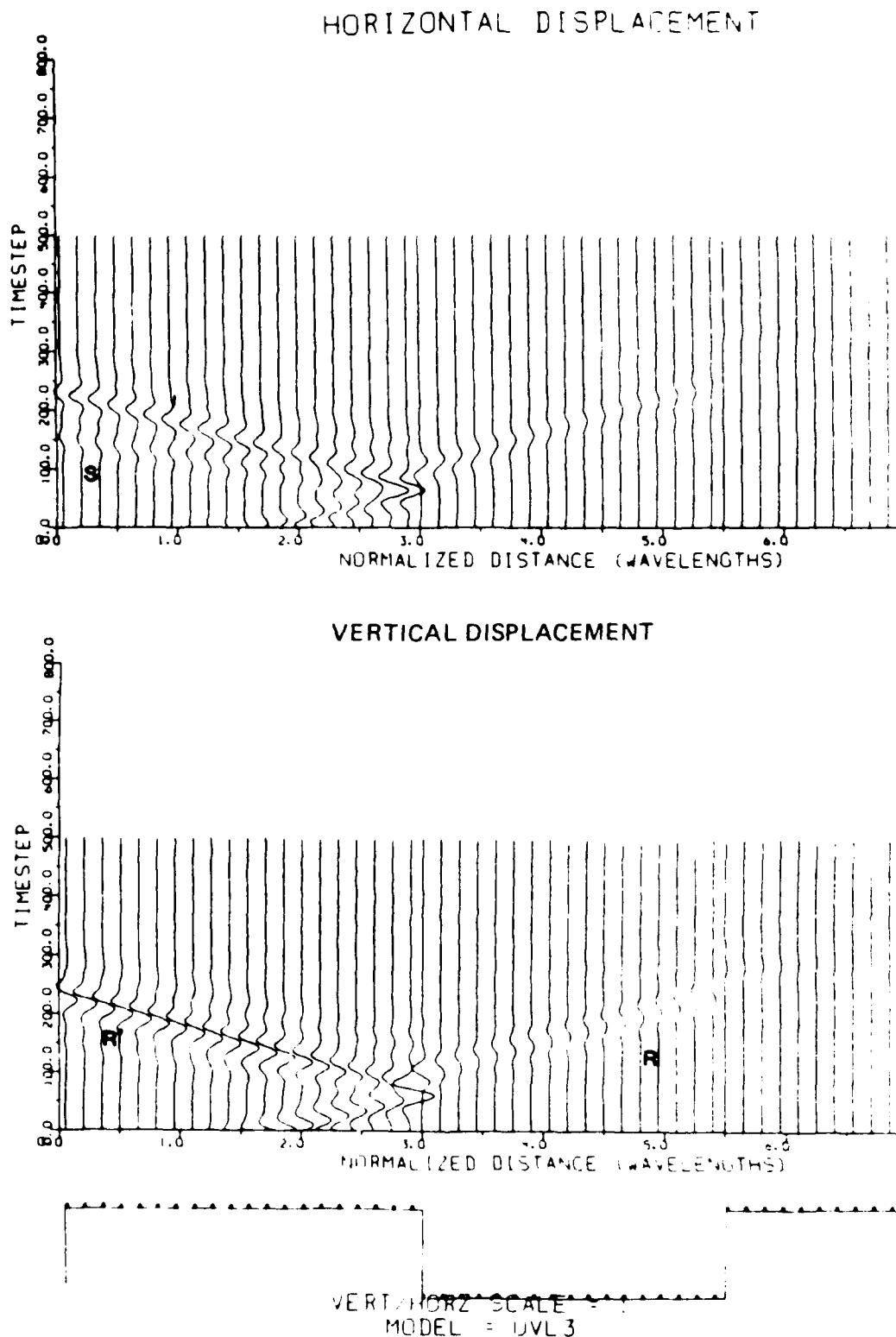


Fig 18: Synthetic surface seismograms for a Rayleigh wave incident on a 1λ deep unfilled straight walled valley in a homogeneous medium. Notice no Rayleigh wave reflections at the far end of the valley. This occurs because less energy enters the basin due to a higher coefficient of reflection at the near side of the valley.

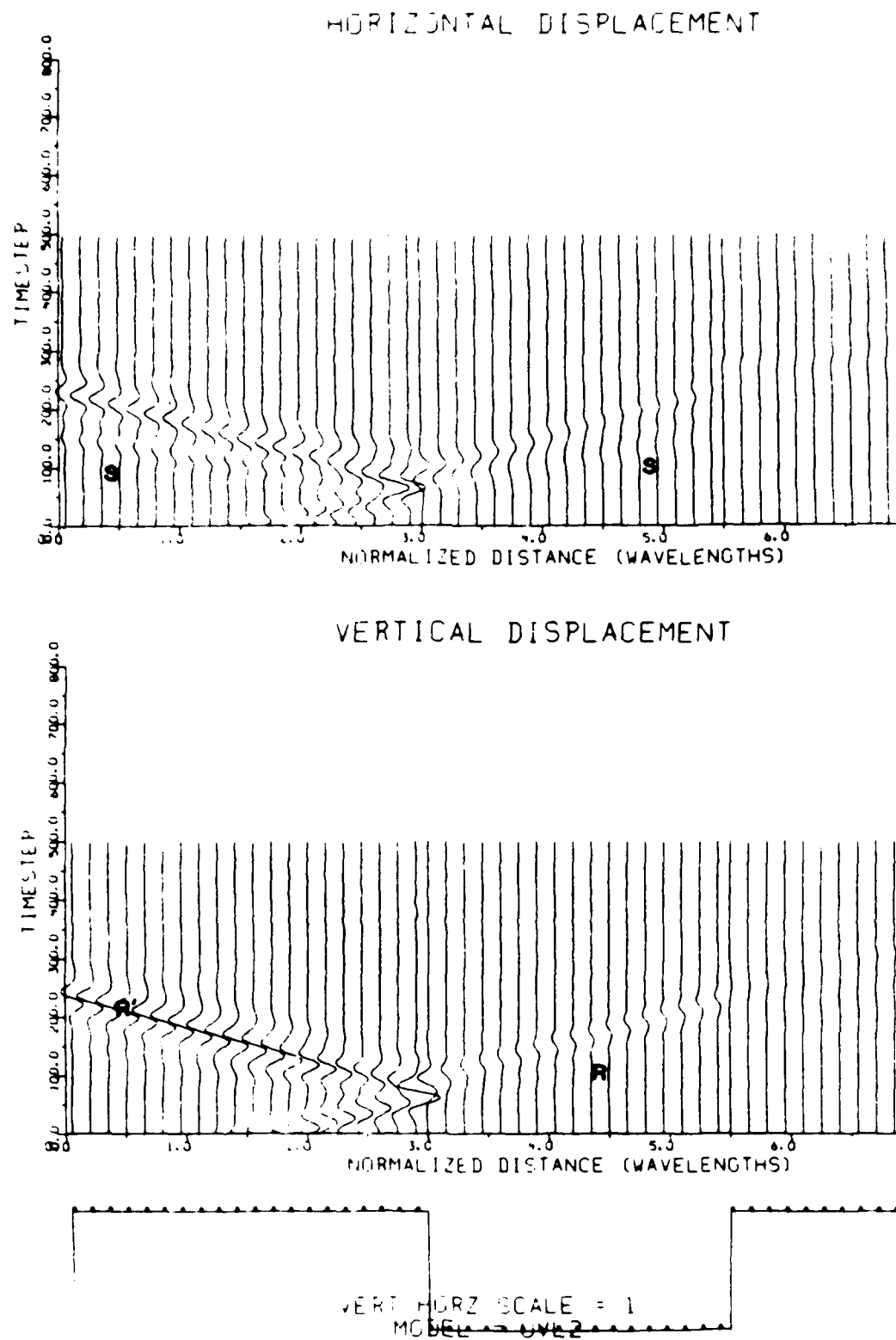


Fig 19: Synthetic surface seismograms for a Rayleigh wave incident on a $3/2\lambda$ deep unfilled valley, in a homogeneous media.

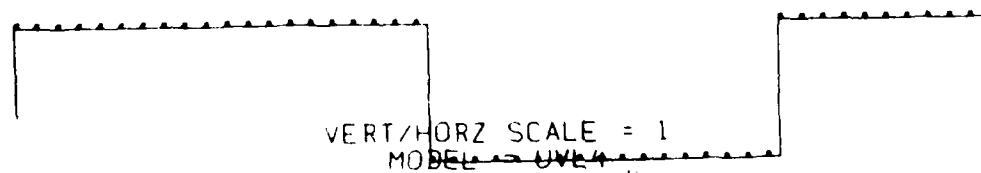
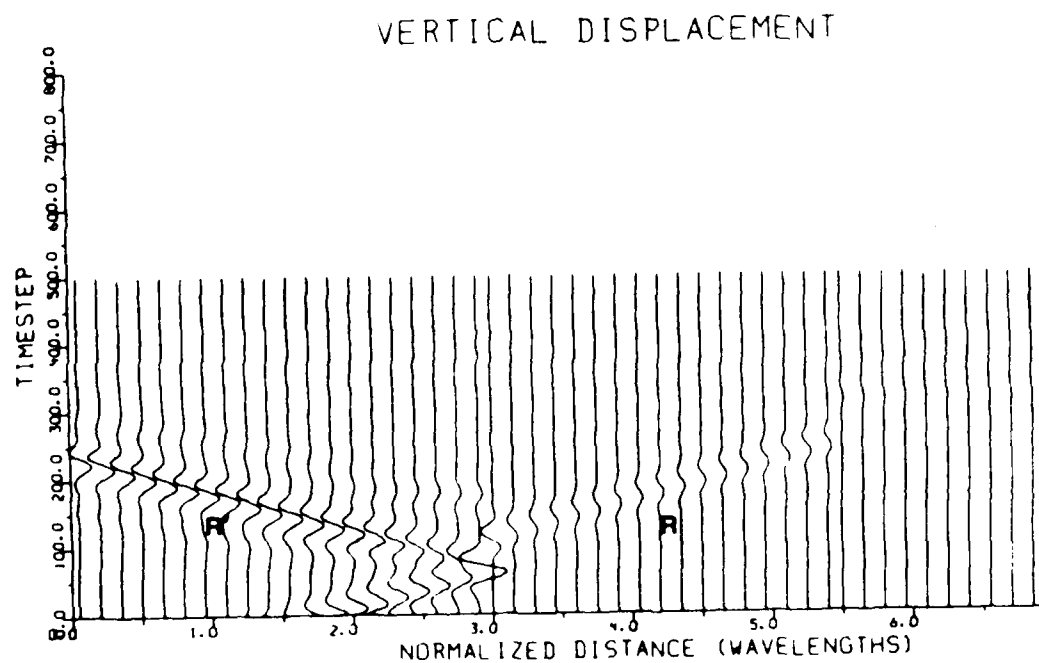
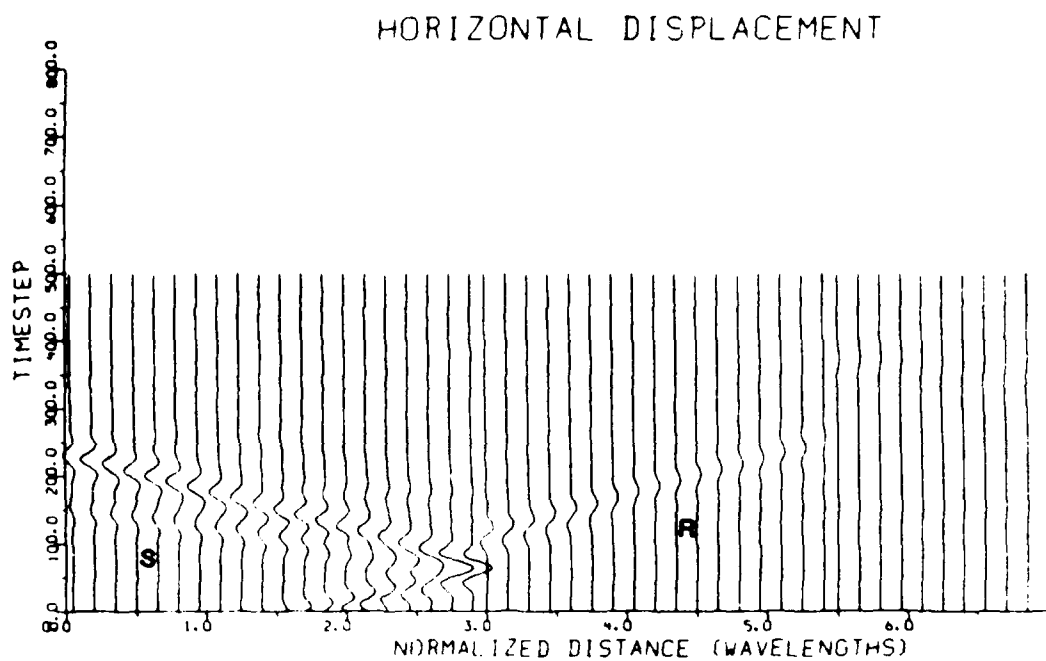


Fig 20: Synthetic surface seismograms for a Rayleigh wave incident on a 2λ deep unfilled valley, in a homogeneous media.

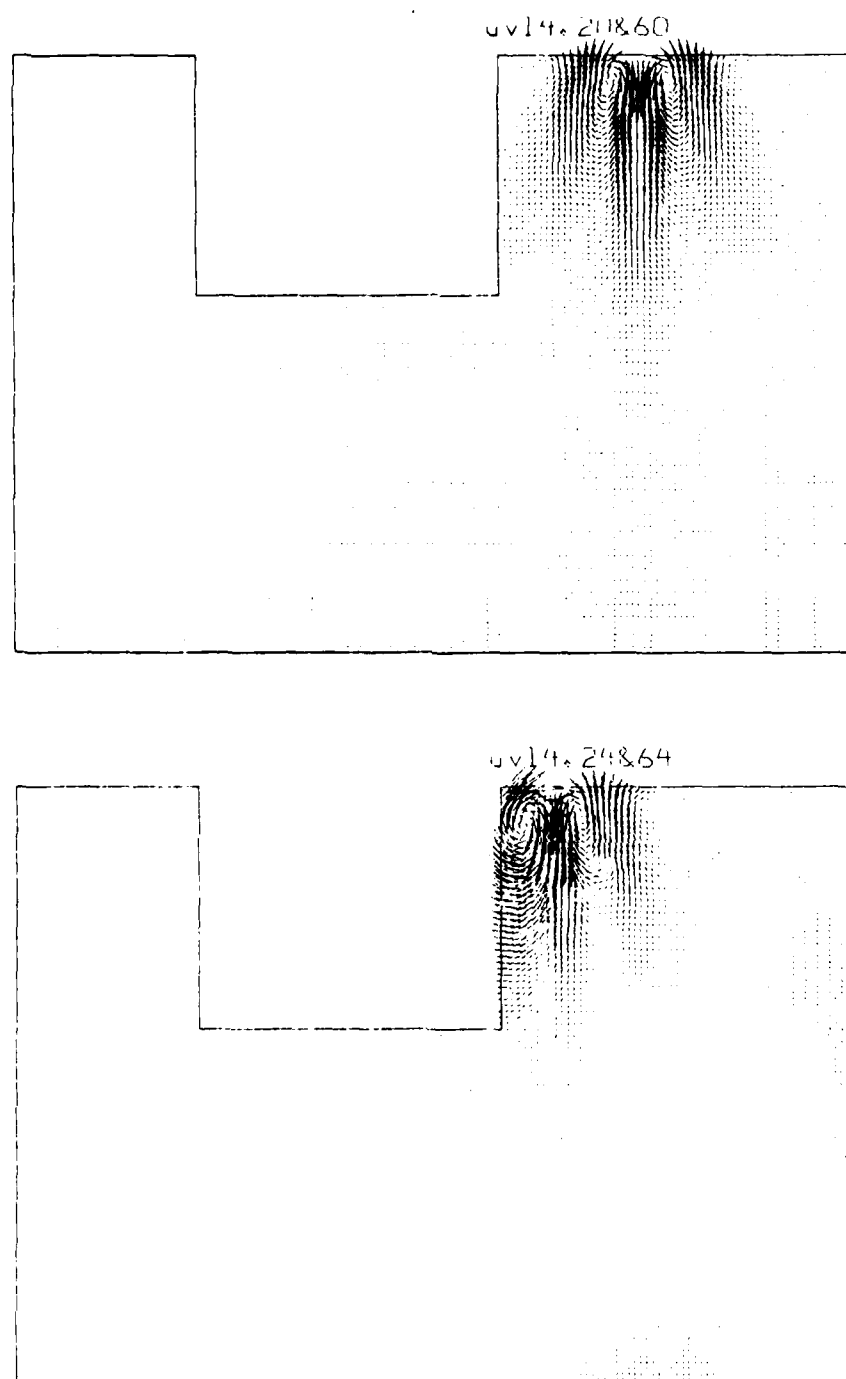
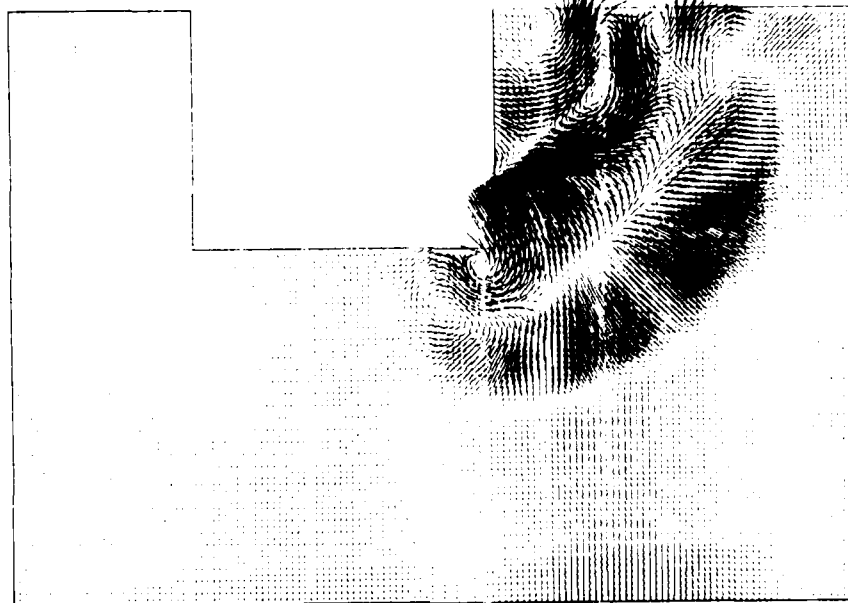


Fig 21: Snapshot displacements at various times, for a 2λ deep valley, in a homogeneous medium.

Qv14. 25868



Qv14. 3 872

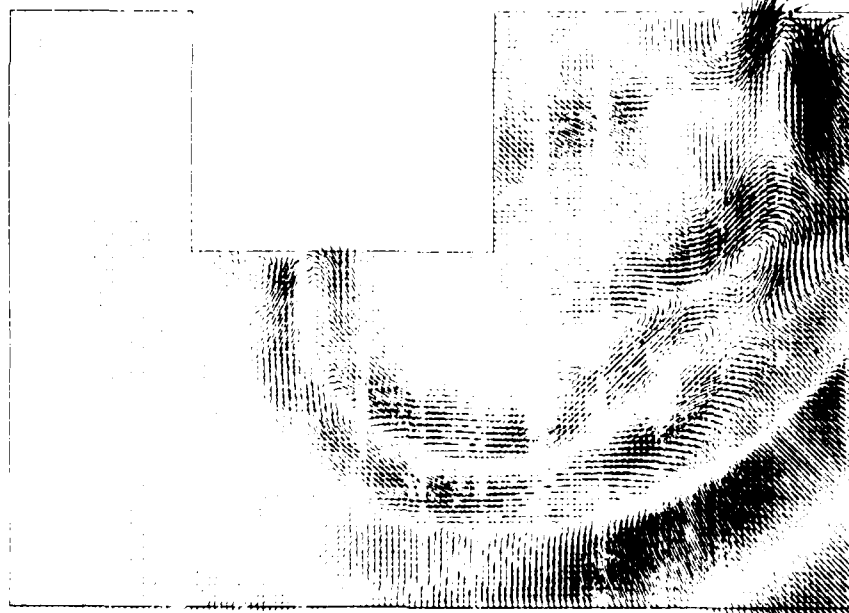
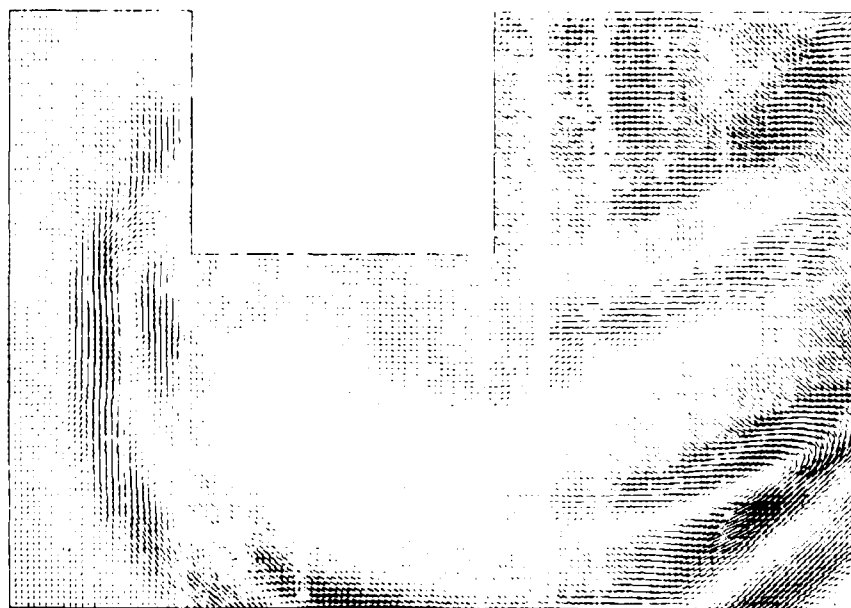


Fig 21: (contd.)

uv14.30&76



uv14.40&80



Fig 21: (contd.)

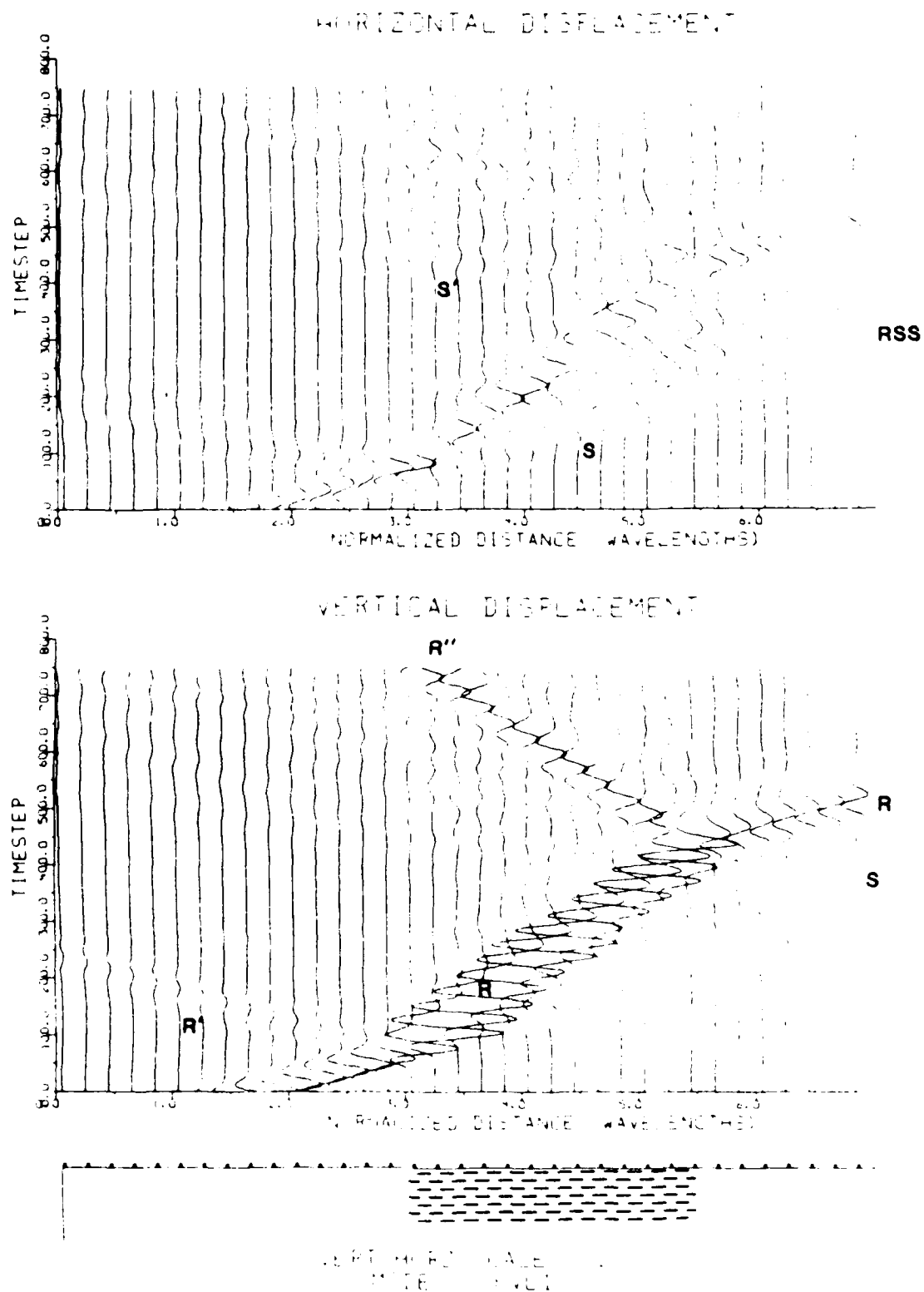


Fig 22: Same as Fig 18, but valley is completely filled with low velocity sediments (cross-hatched area). The ratio of the low velocity to high velocity is 0.44.

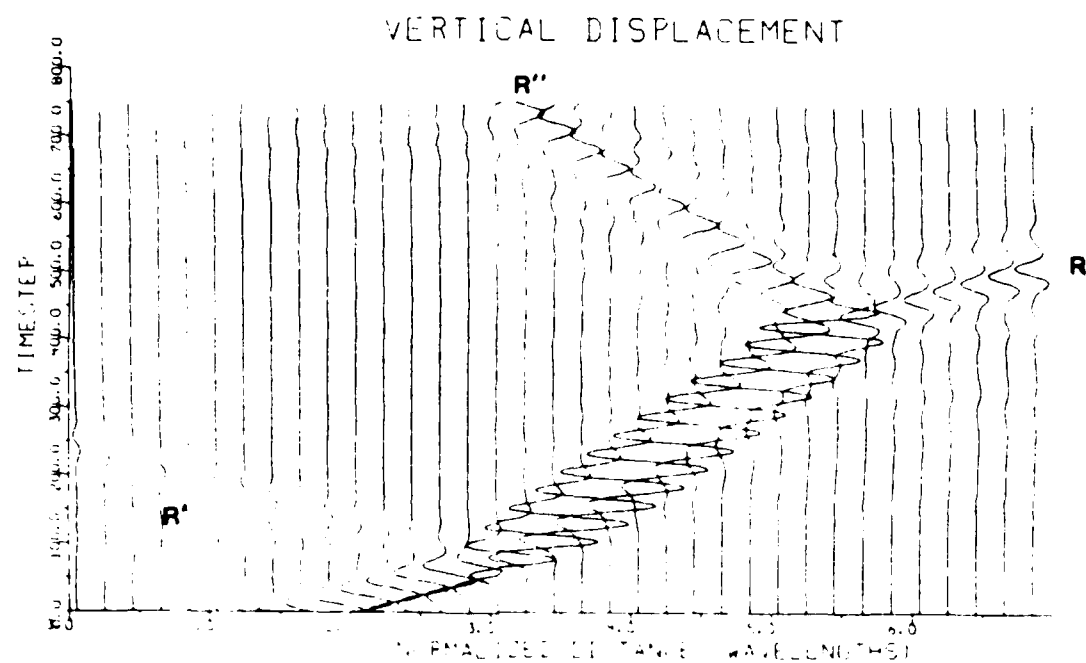
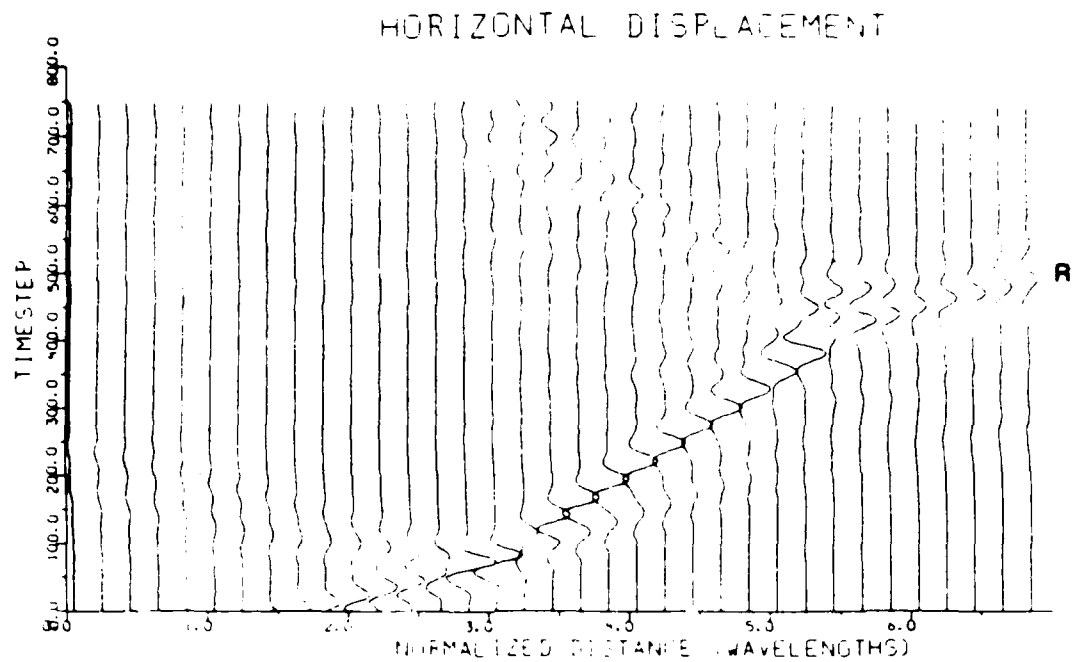


Fig 23: Same as Fig 22, but valley is 1λ deep.

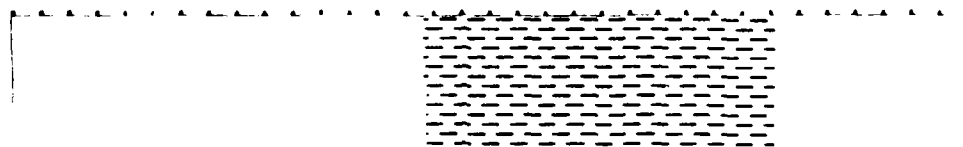
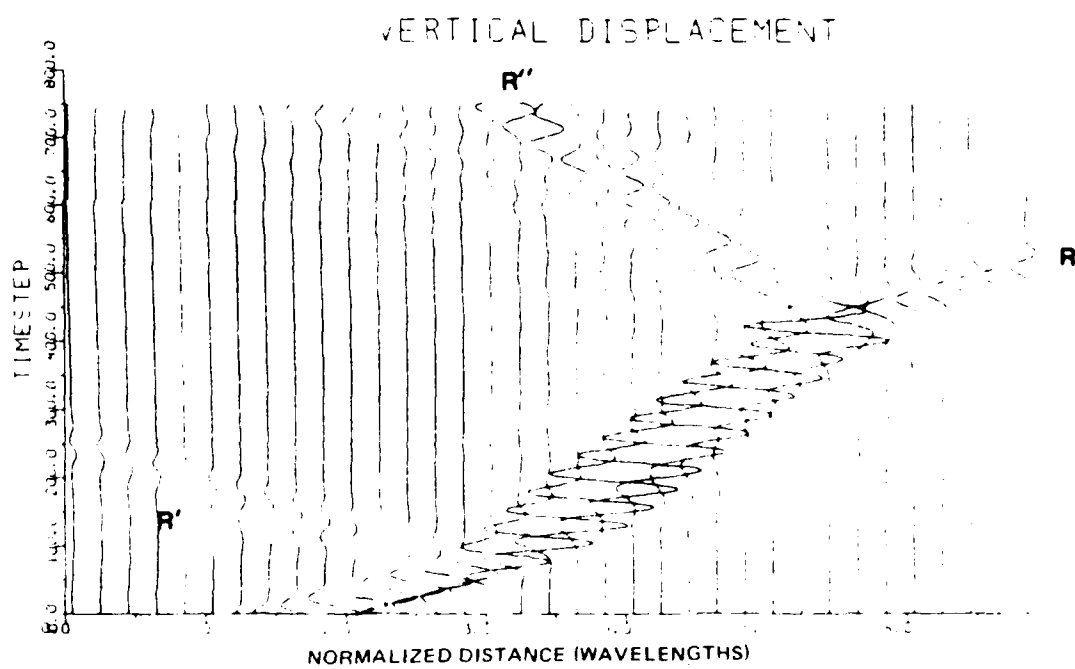
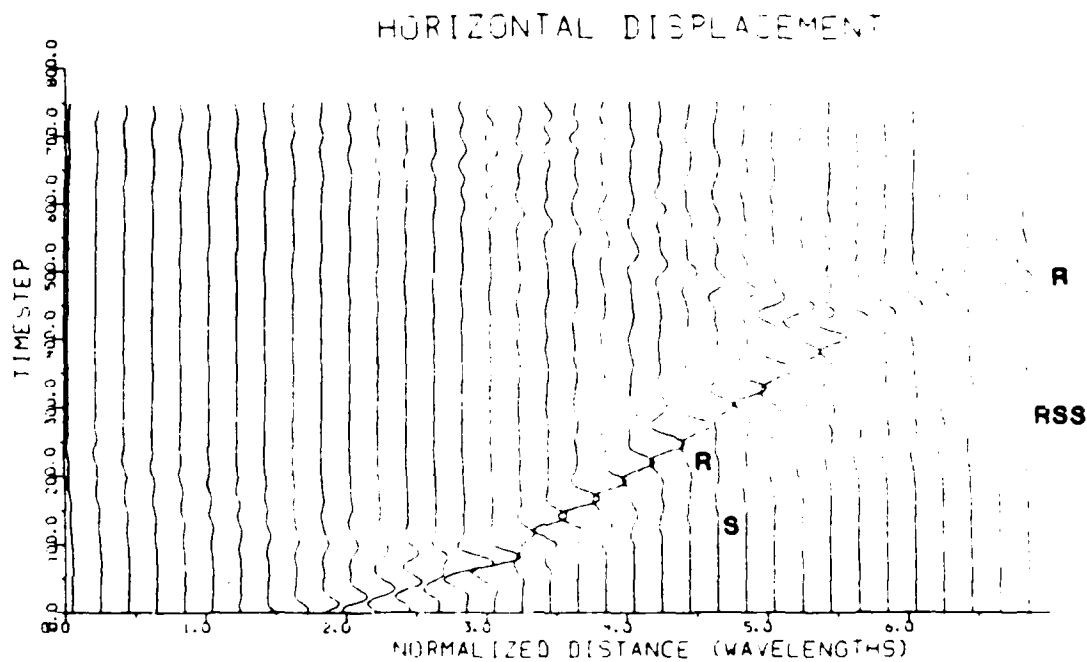


Fig 24: Same as Fig 22, but valley is $3/2\lambda$ deep.

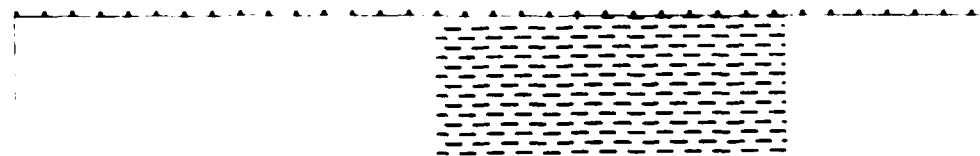
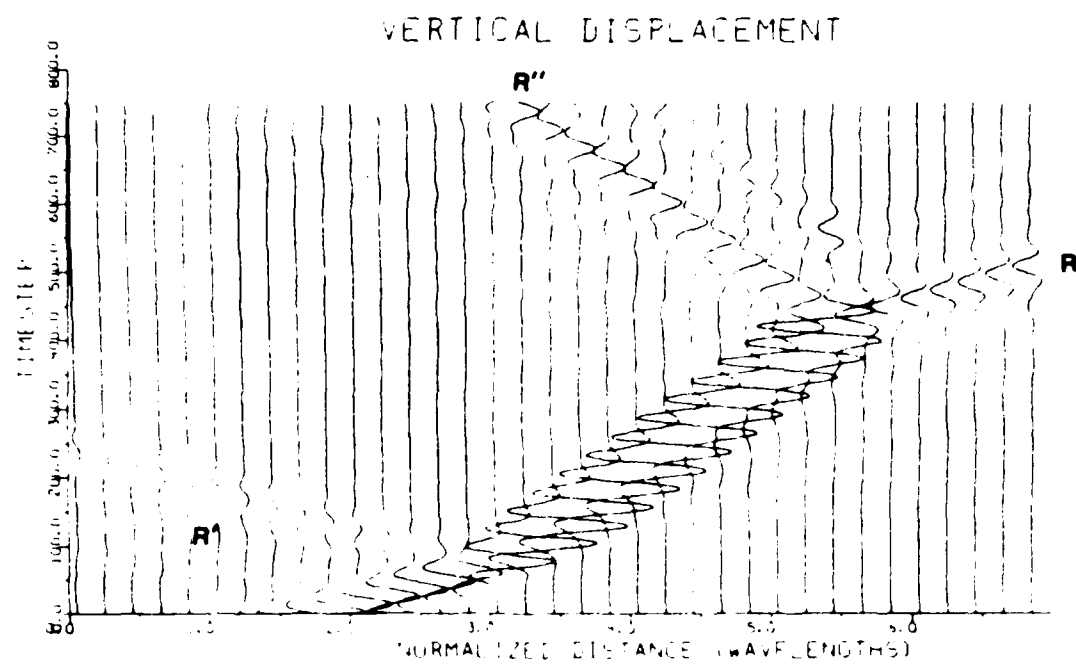
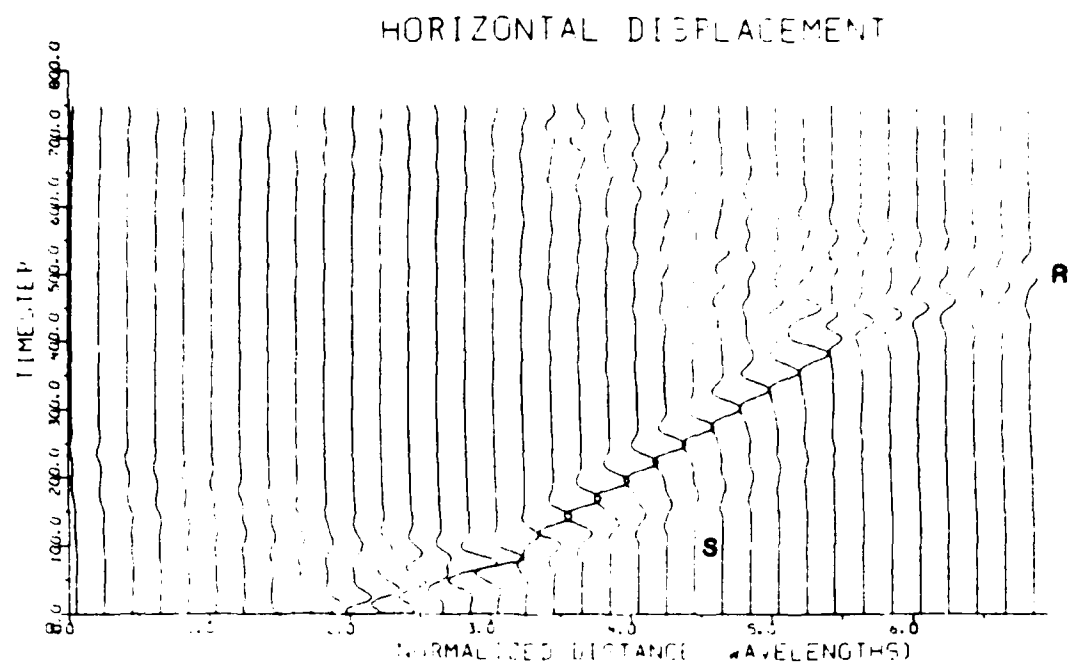


Fig 25: Same as Fig 22, but valley is 2λ deep.

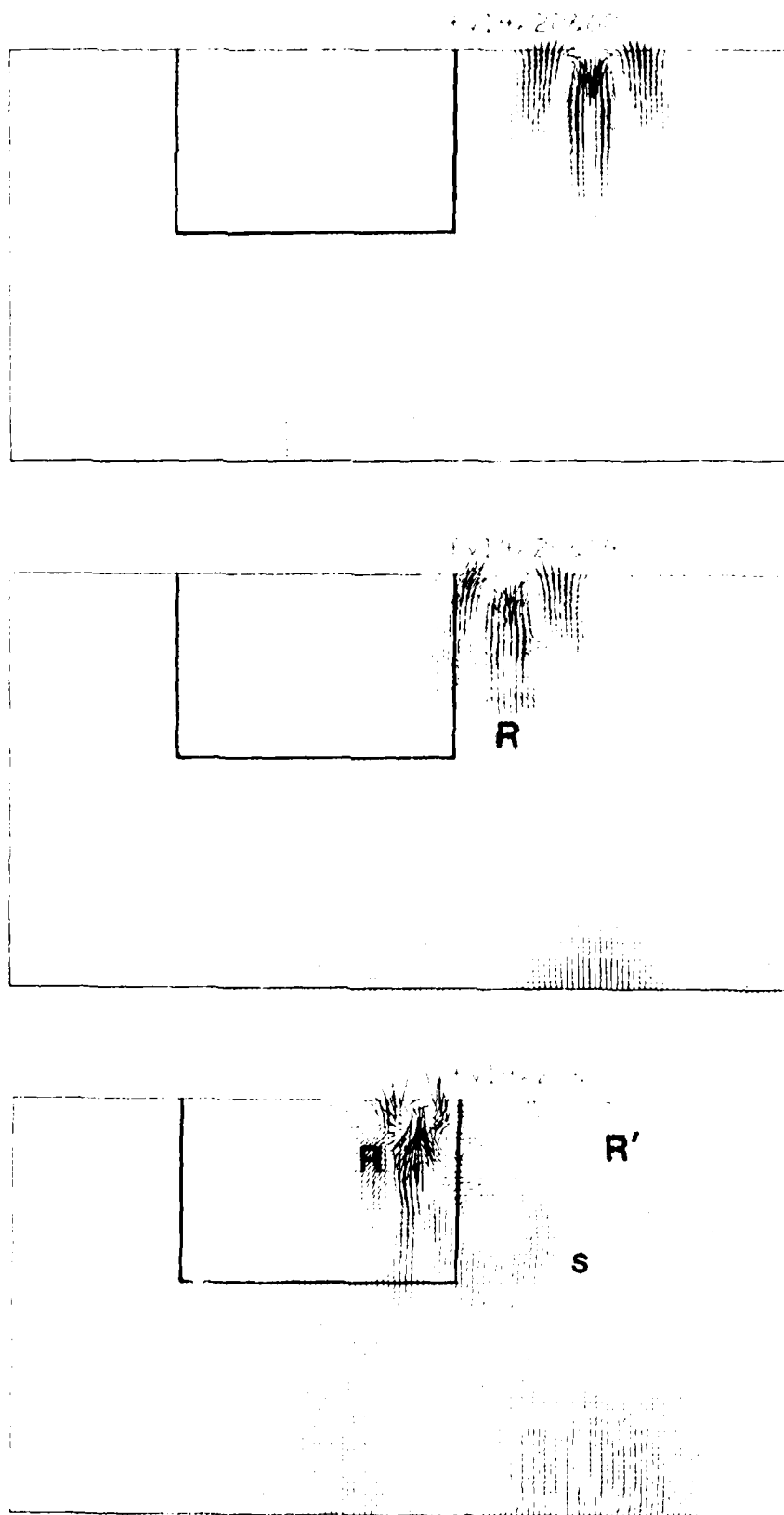
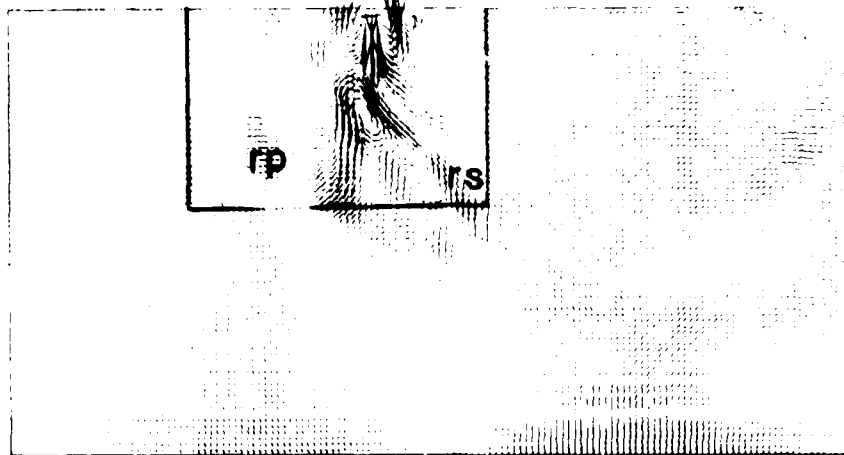
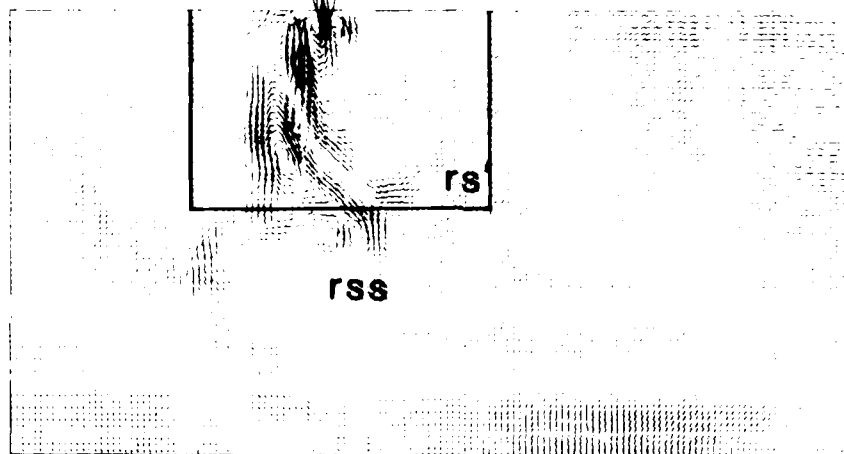


Fig 26: Same as Fig 21, but valley is filled with low velocity sediments (area inside box).

fv14.32872



fv14.36876



fv14.40880

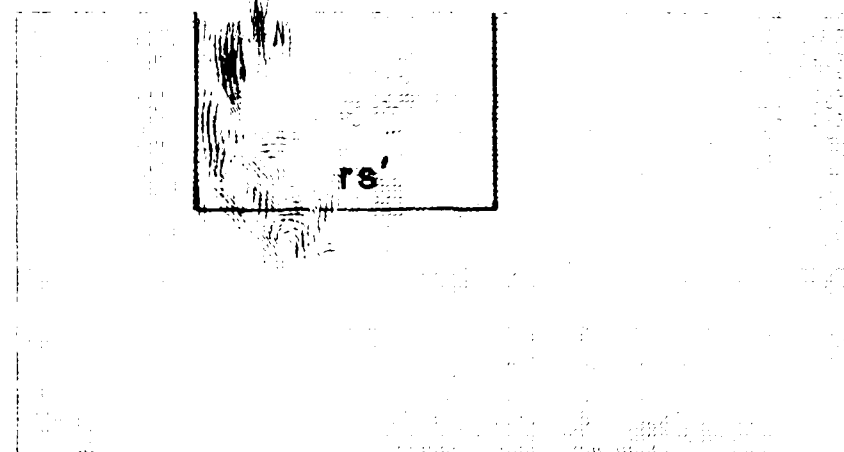


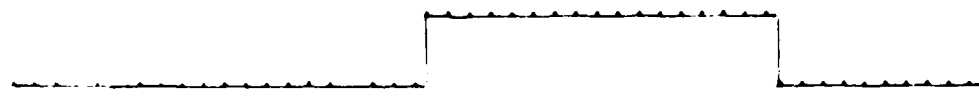
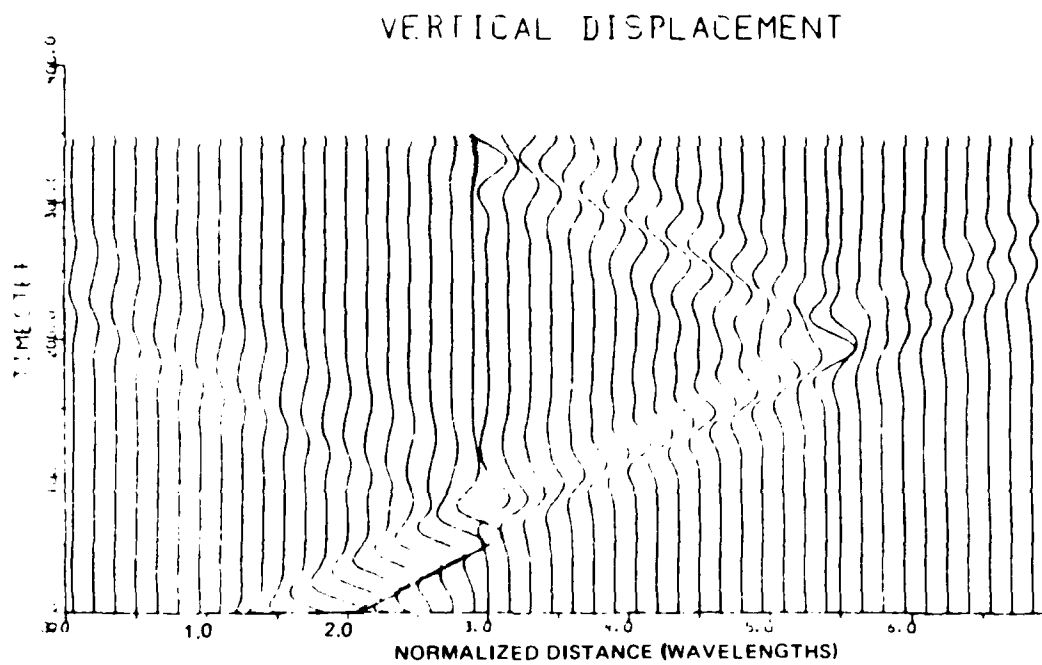
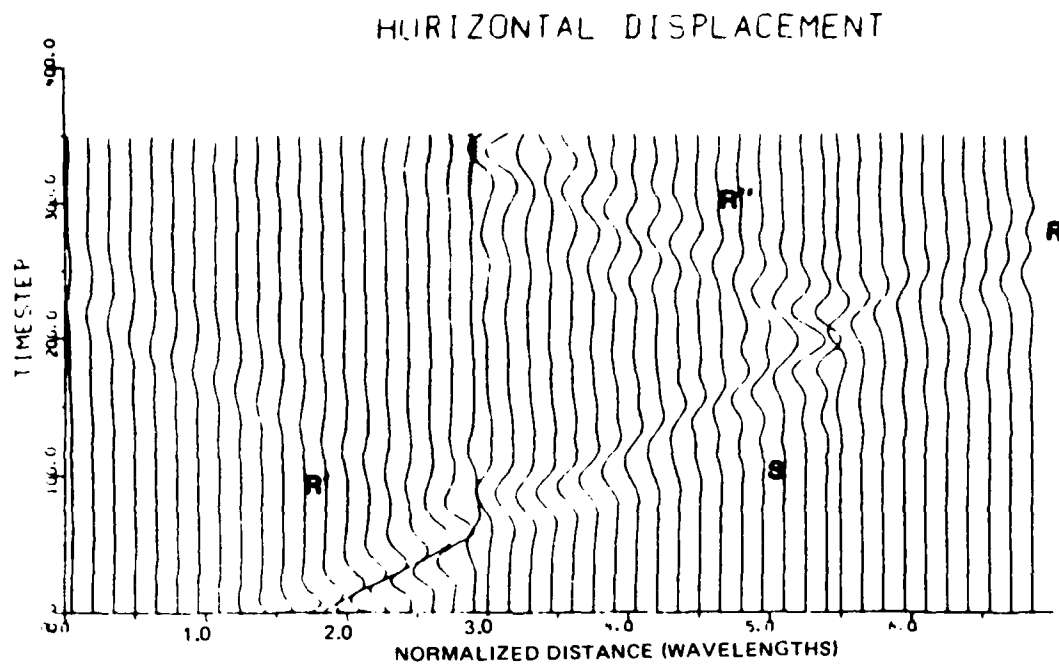
Fig 26: (contd.)

normal incidence from a high impedance medium to a low impedance medium, well known in exploration seismology.

- (2) Some of the Rayleigh wave energy is converted to S waves in both the high and low velocity media [(s) and (rs), Figure 26].
- (3) Subsequently, when the body wave inside the valley hits the lower boundary, it is partially reflected back inside the valley (rs'), and partially transmitted into the higher velocity substrate (rss).
- (4) From Figures 22 - 26 it is plain that a large percentage of the energy in both the horizontal and vertical components which enters the filled valley is trapped and reverberates.
- (5) The complexity of the wavefield increases as the valley becomes shallower. It should be noted all the features described above exist in the shallower valleys (Figures 22 - 24) but are hidden by the multitude of different raypaths.

Homogeneous and Inhomogeneous Mesas

Figures 27 -30 show the results for homogeneous mesas, that is mesas made of the same material as the substrate. Similarly to the valley geometry, the mesa geometry can be constructed by combining an upstep and a downstep. All of the same scattering phenomena discussed in the step geometries are present in the mesa geometry. In addition there is a strong Rayleigh wave produced when the S wave scattered from the first corner, which is strongly "beamed" in the forward horizontal direction due to the upstep, strikes the opposite side of the mesa. This phase is labeled rsr in Figure 29. The phase labelled R travels around the surface of the mesa, producing scattered body waves at each corner. The scattering pattern is more complex if the mesa consists of low velocity material over a high velocity half space, Figures 31 - 34. In this case, the incident Rayleigh wave



VERT HORIZ SCALE = 1
MODEL = M5A1

Fig 27: Synthetic surface seismograms for a $1/2\lambda$ high, homogeneous, straight sided mesa.

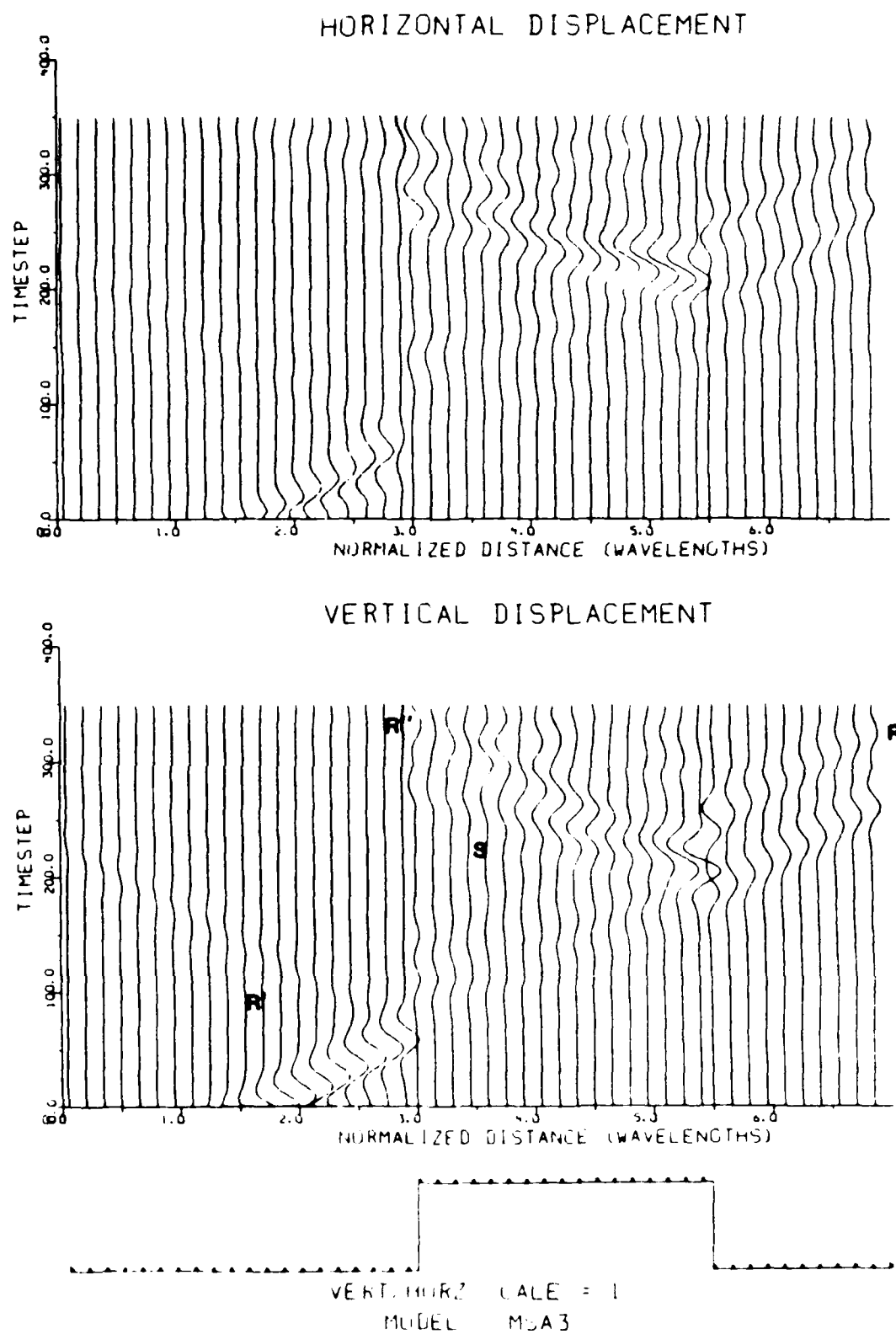


Fig 28: Same as Fig 27, but mesa is 1λ high.

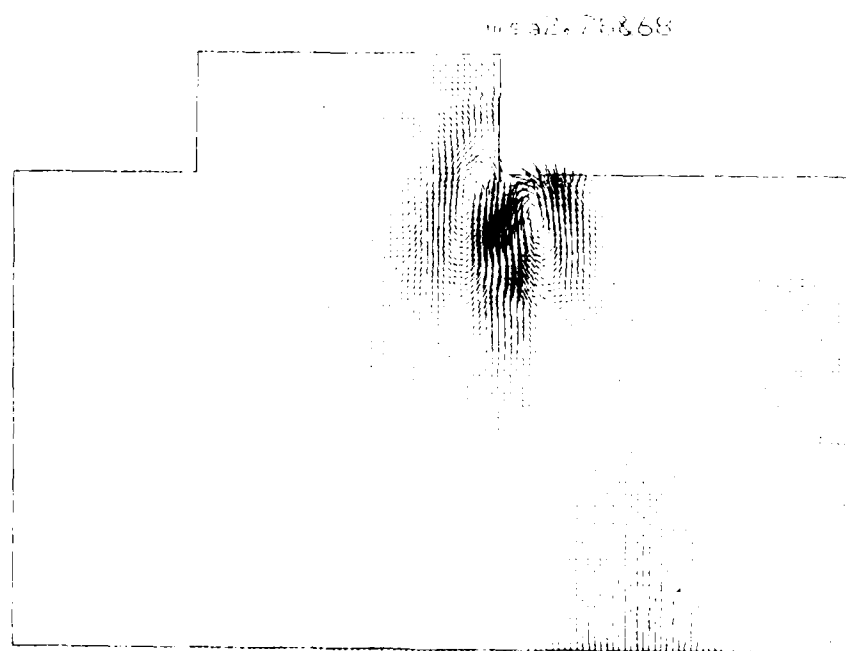
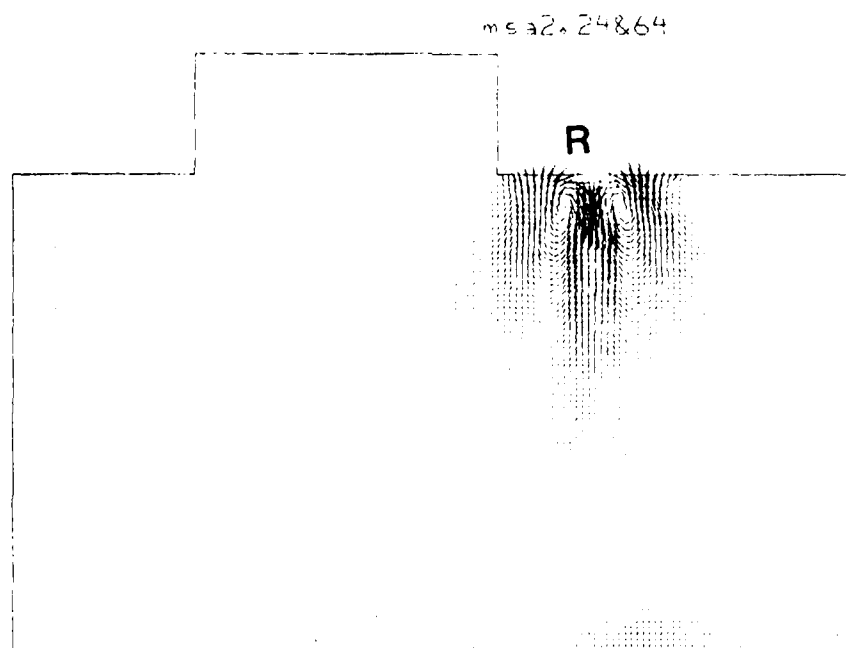
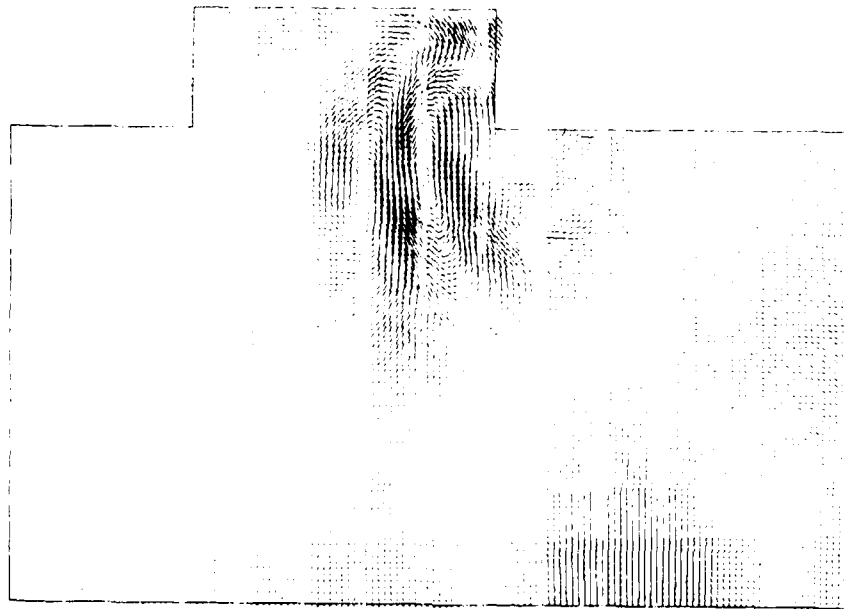


Fig 29: Snapshot displacements for the 1λ high homogeneous mesa.

mesa 32872



R

mesa 32876



Fig 29: (contd.)

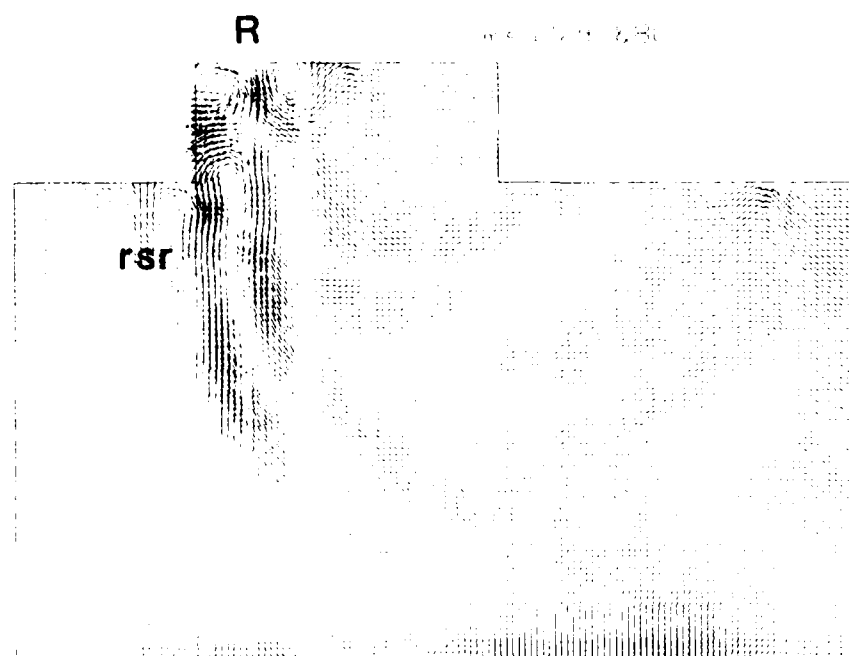


Fig 29: (contd.)

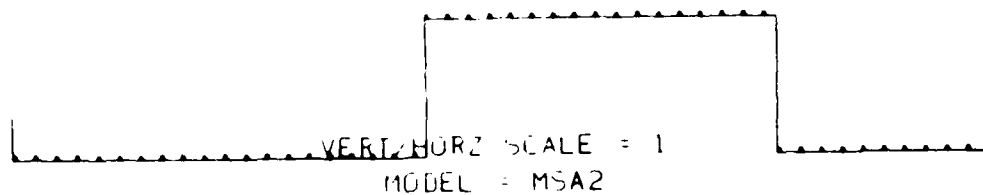
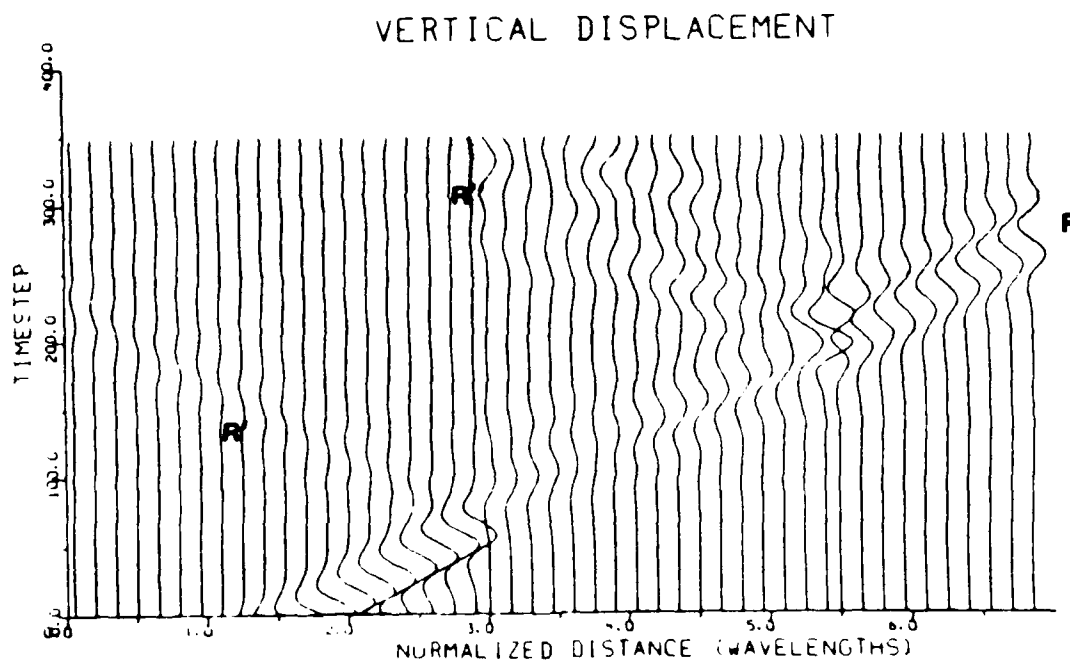
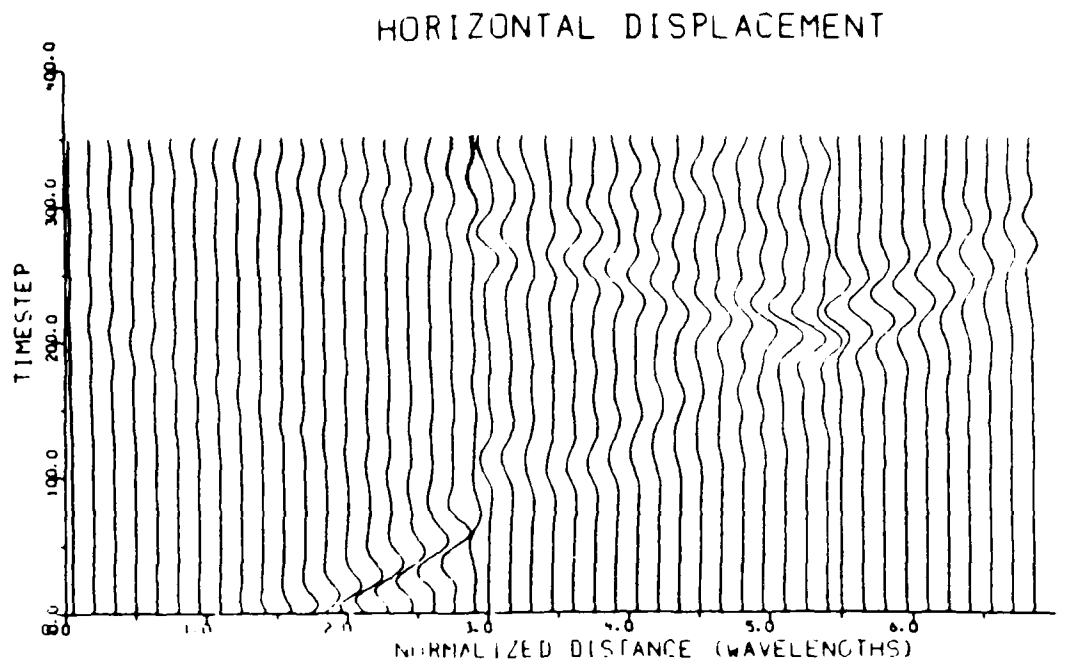


Fig 30: Same as Fig 27, but mesa is $3/2\lambda$ high.

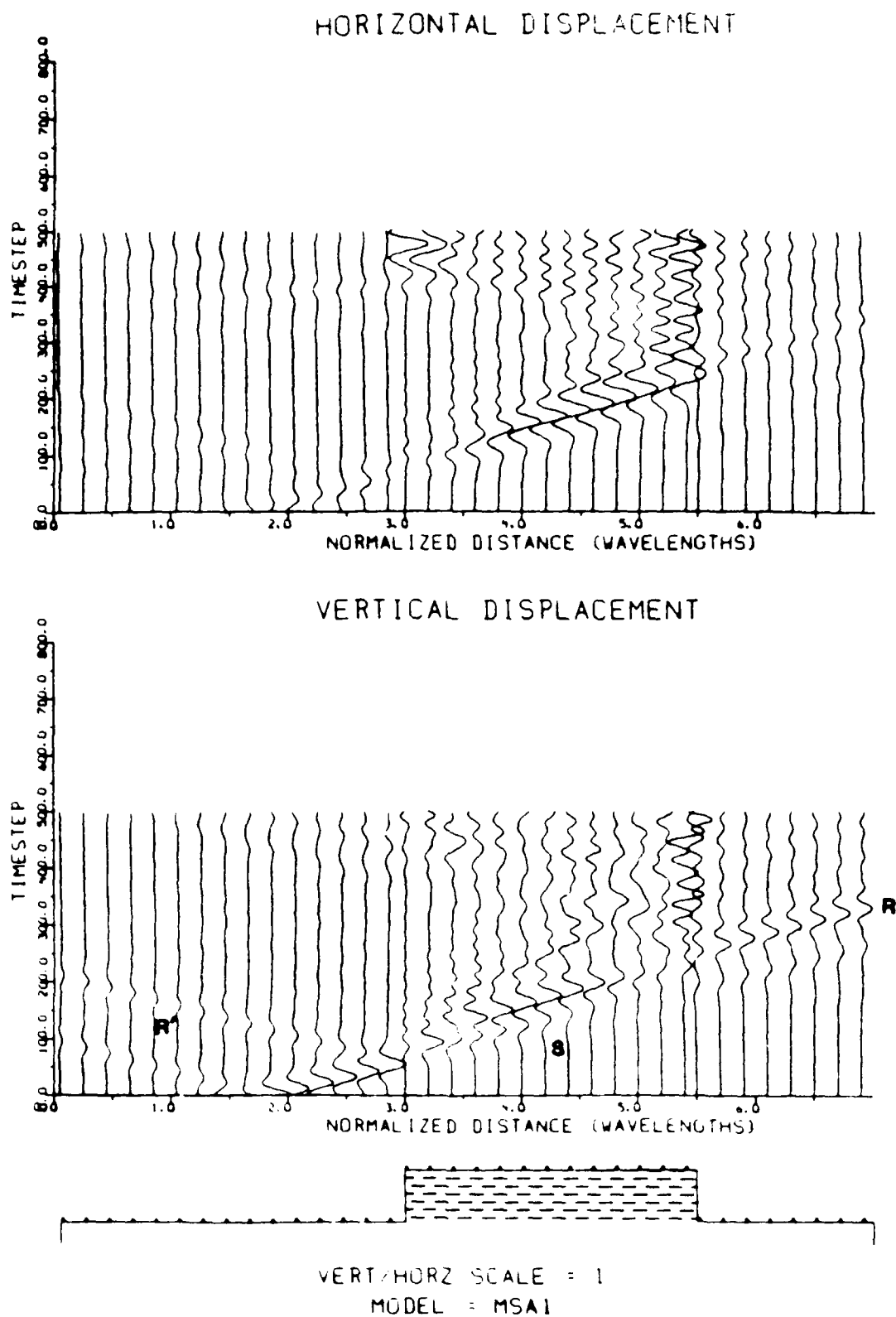
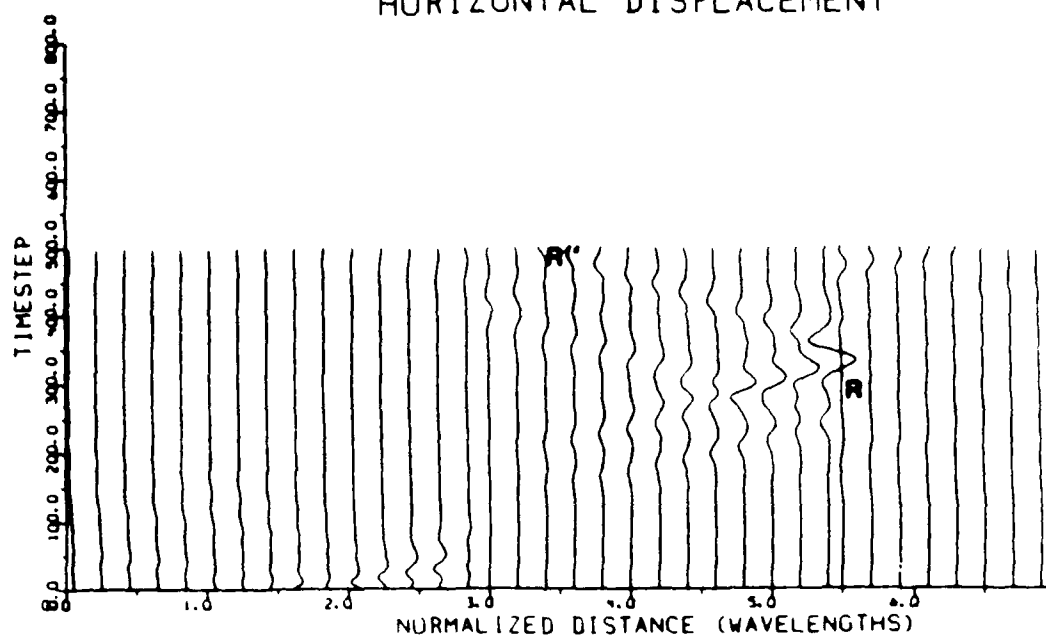
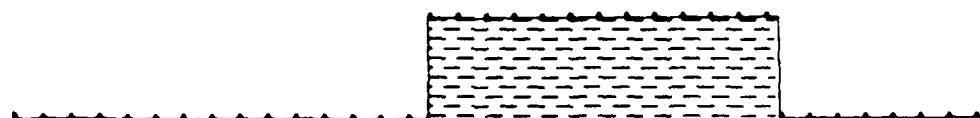
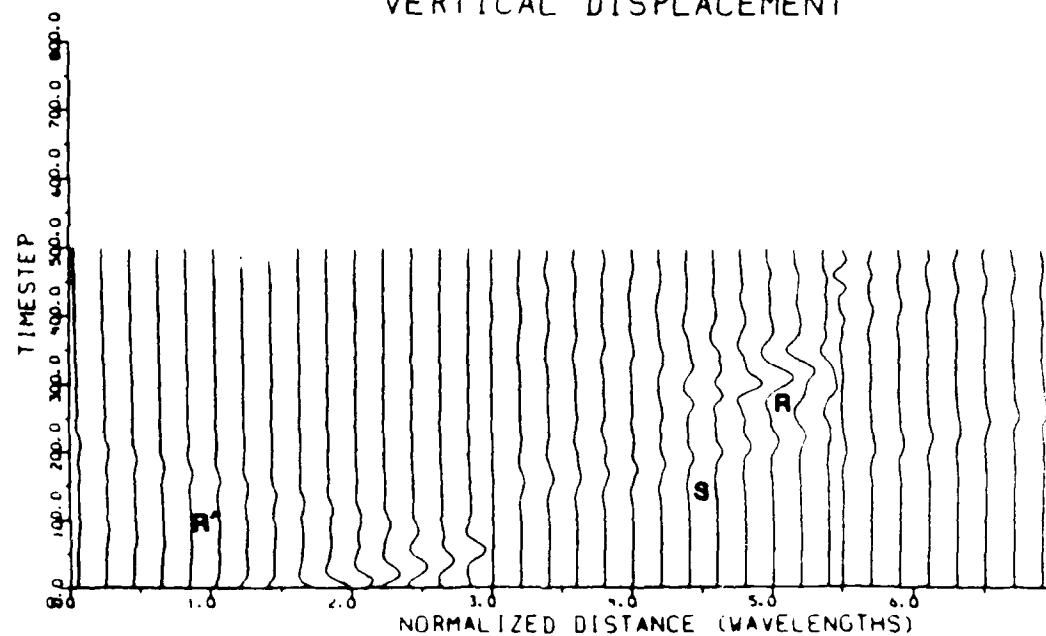


Fig 31: Same as Fig 27, but mesa consists entirely of low velocity material sitting on a high velocity half space. The velocity of the mesa is 44% of the half space velocity.

HORIZONTAL DISPLACEMENT



VERTICAL DISPLACEMENT



VERT/HORZ SCALE = 1
MODEL = MS23

Fig 32: Same as Fig 31, but mesa is 1λ high.

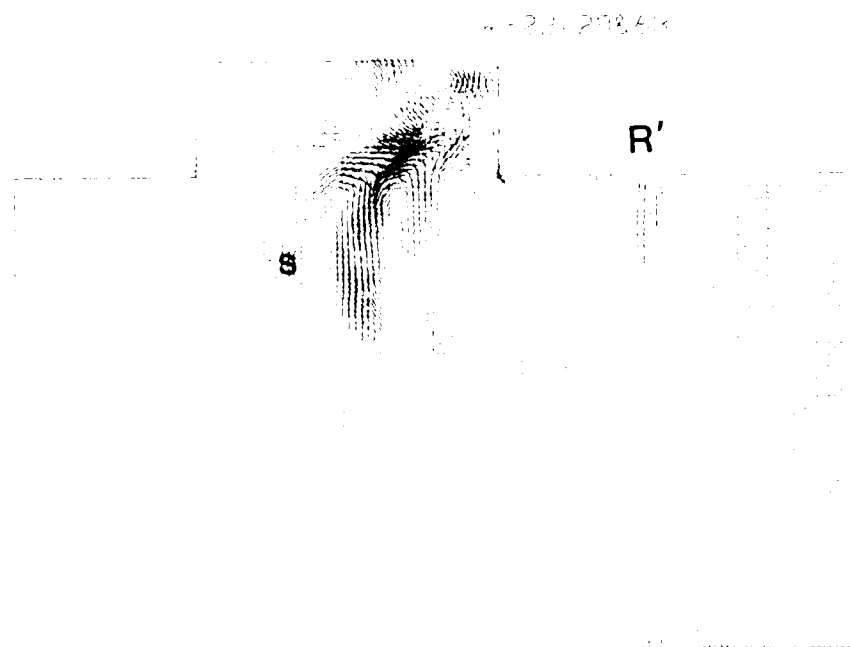
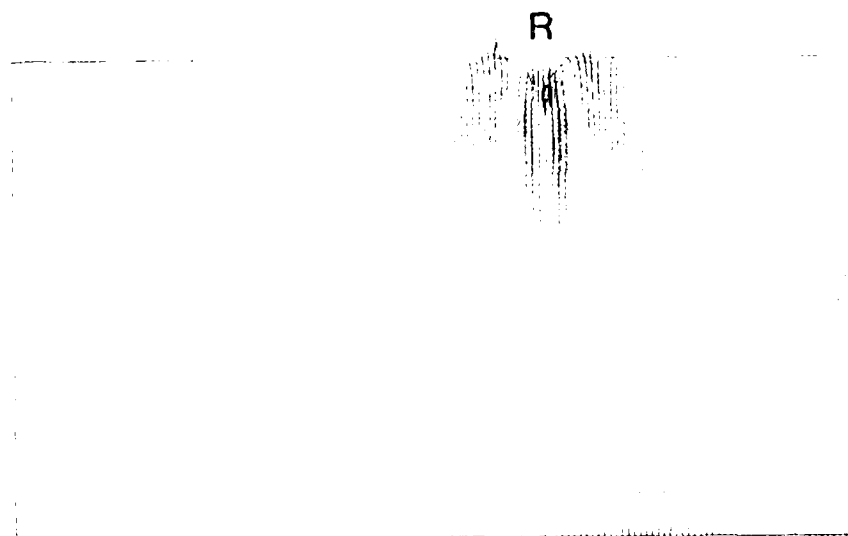
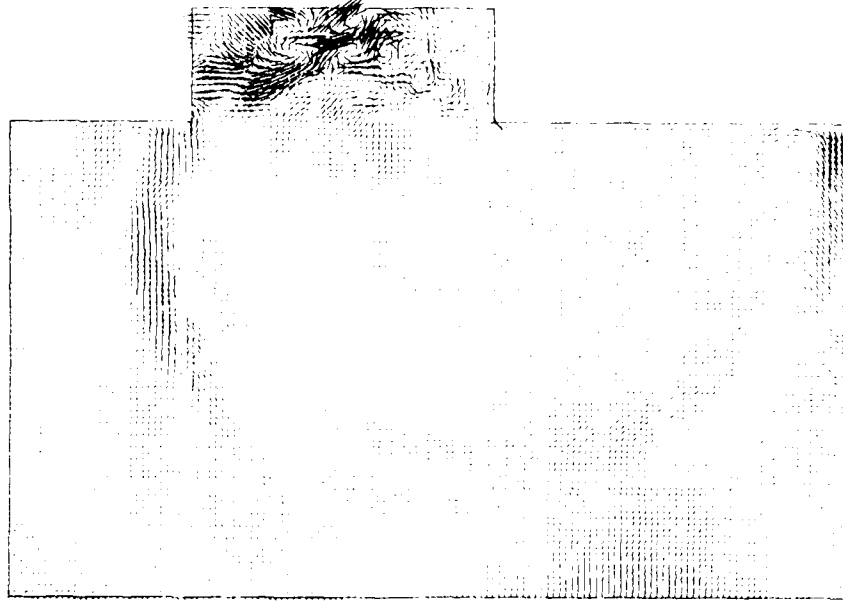


Fig 33: Same as Fig 29, but mesa is constructed of low velocity material as described in Fig 31.

m s22. 328.72



m s22. 368.76

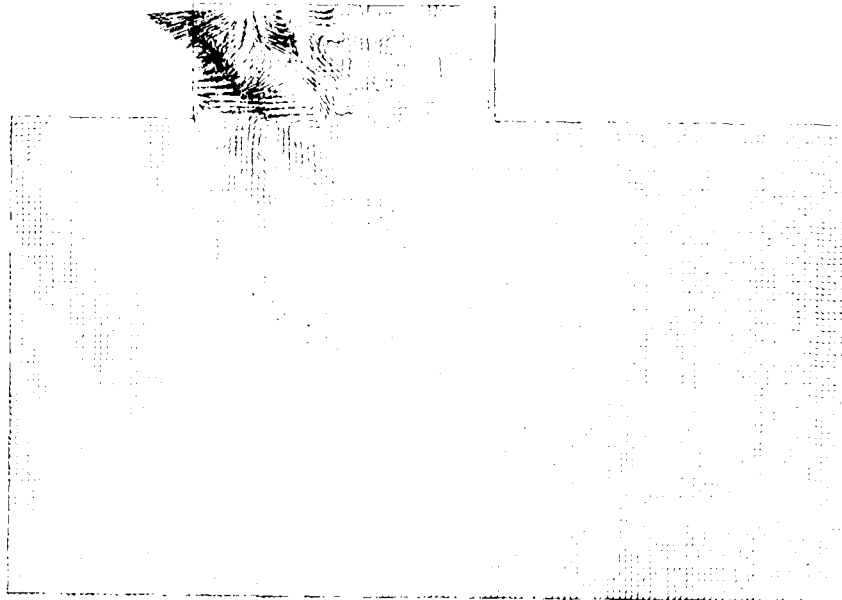


Fig 33: (contd.)

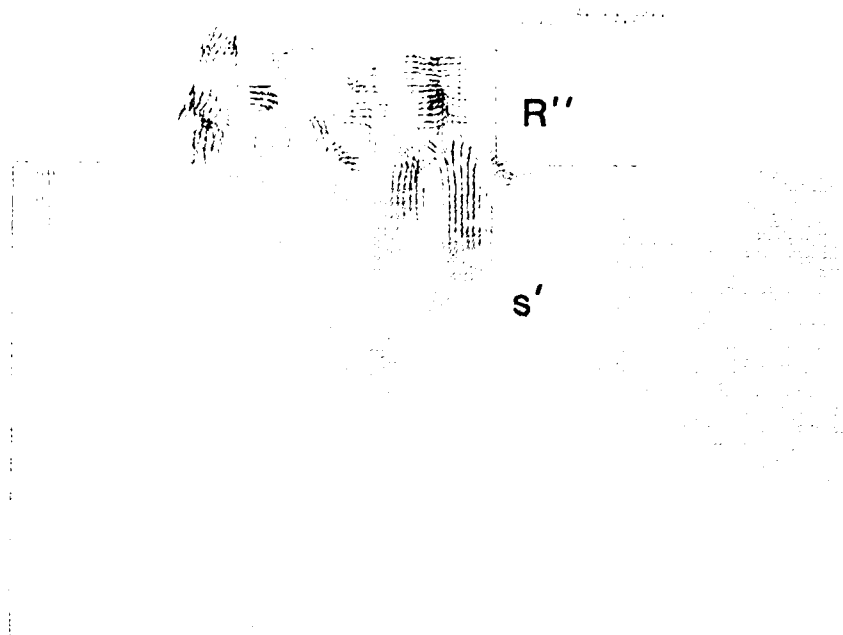
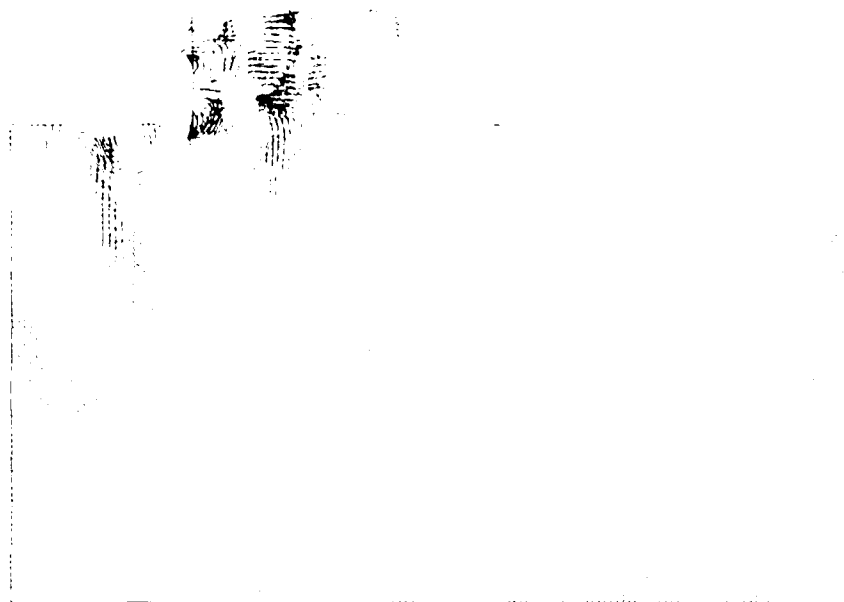


Fig 33: (contd.)

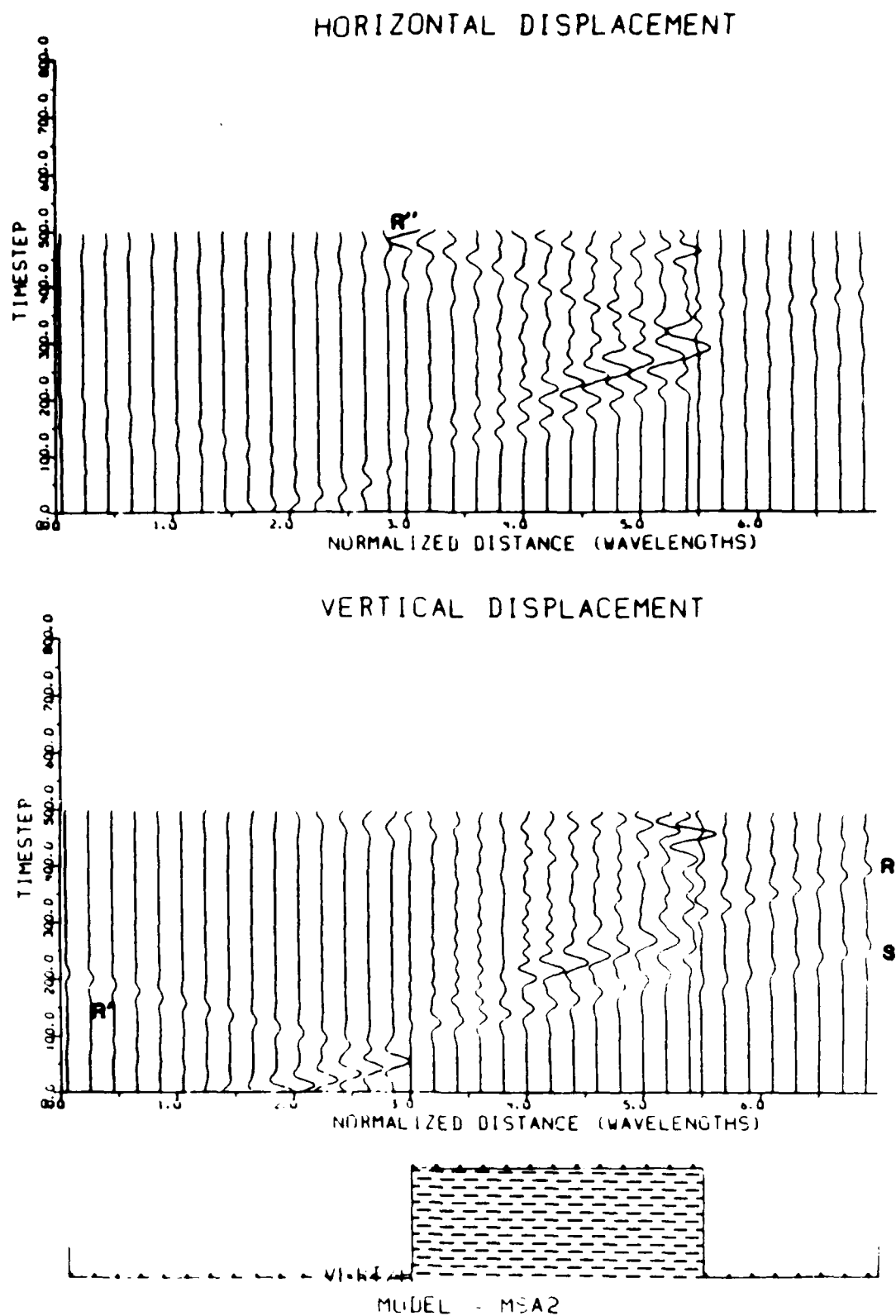


Fig 34: Same as Fig 31, but mesa is $3/2\lambda$ high

produces a larger reflected pulse. In a similar manner to the filled valley, the amplitude of the transmitted Rayleigh wave increases as it enters the low velocity material of the mesa. There is trapping of energy and reverberation within the mesa, as seen in Figure 33. This occurs because most of the energy which enters the mesa is trapped due to the large velocity discontinuity.

IV. COMPARISON BETWEEN PHYSICALLY AND NUMERICALLY MODELED RESULTS

Introduction

The ultimate objective of this study was to compare the results obtained by the two techniques presented in this report. To achieve this, we plot a single finite difference generated synthetic seismogram, similar to those displayed in the last chapter, which we compare to the seismograms generated by the physical modeling. The two columns of seismograms displayed in Figure 35 are seismograms for seven of the geometries we investigated. The geometries are, in descending order from the top of the page:

- (1) 2λ high low velocity mesa.
- (2) 1λ high low velocity mesa.
- (3) The source after traveling across a high velocity half space.
- (4) Unfilled 1λ deep basin.
- (5) Filled 1λ deep basin.
- (6) Unfilled 2λ deep basin.
- (7) Filled 2λ deep basin.

In Figure 35a on the left, the traces show the vertical displacement, generated by the finite difference method, at a single seismometer location as a function of time. Figure 35b on the right is a compilation of the corresponding traces generated by physical modeling.

In comparing the two columns of traces, two traces generated by two different sources cannot necessarily be directly compared; the seismograms should also be compared with the unscattered source function (the third trace in each column). In both

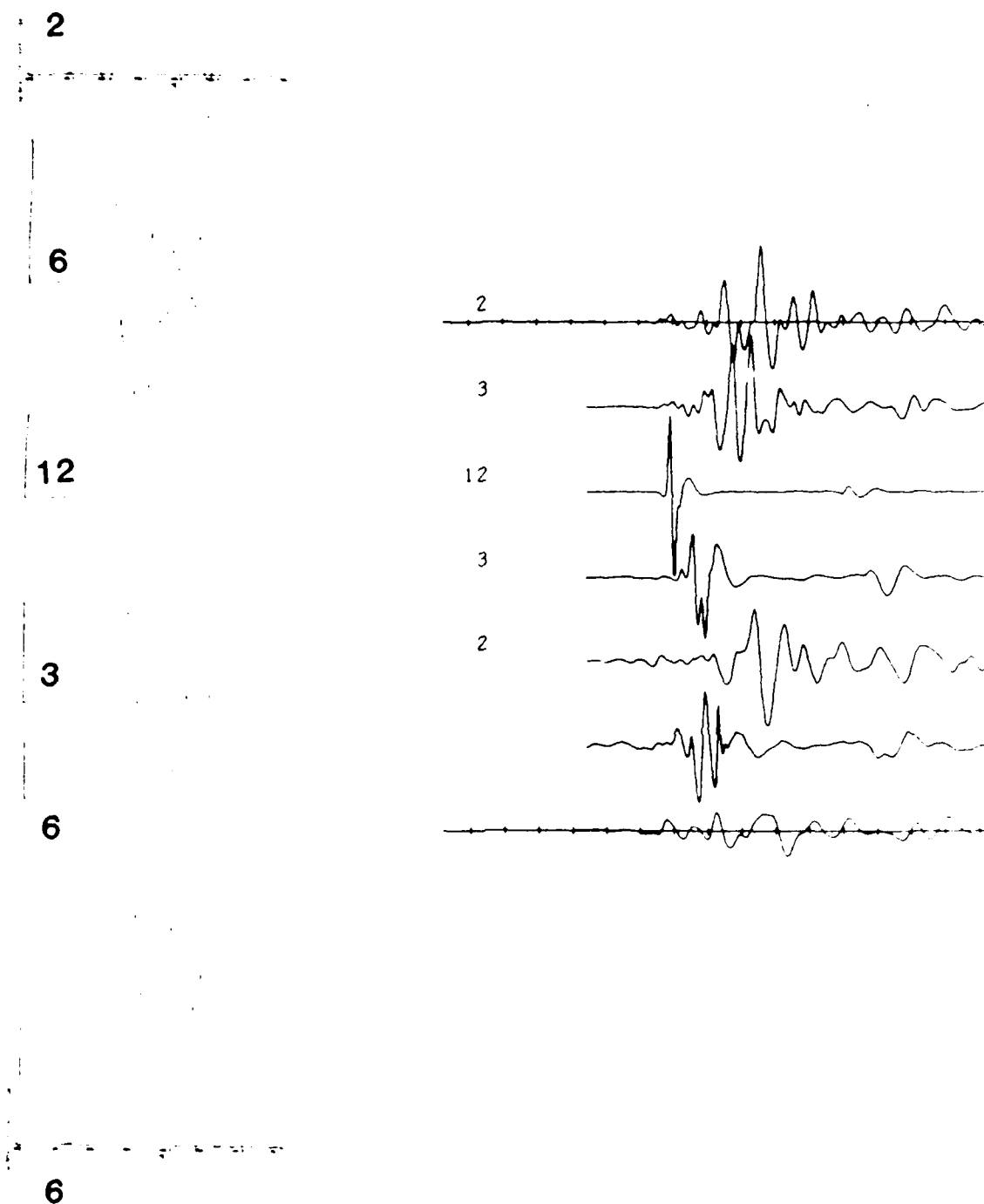


Fig 35: Comparison of synthetic seismograms (a, left) with observed seismograms (b, right). From the top in both (a) and (b) the seismograms are for: 2λ high low velocity mesa; 1λ high low velocity mesa; source; unfilled 1λ deep basin; filled 1λ deep basin; unfilled 2λ deep basin; unfilled 2λ deep basin.

columns of traces, the numbers which appear at the beginning of some traces are attenuation factors. In other words, a trace with an attenuation factor of 4 has been compressed by a factor of four. Also, in comparing the two techniques, note that the physical modeling was carried out in three dimensions, but the numerical calculations could only be done in two dimensions. The significance of this is two-fold: arrivals which come from outside the plane passing between the source and receiver will not appear on the numerically generated traces, and energy which, in three dimensions, leaves the plane between the source and receiver is not allowed to leave this plane in the numerical models.

Low Velocity Mesas

The comparison between the two methods is generally good for the low velocity mesa geometry. The first four arrivals seen in Figure 35b are present in Figure 35a. For the reasons described above the shapes of the two seismograms are different, but the same features are present in both. The early body wave arrivals are clearly seen on both traces. Note that both techniques show a broadening of the input pulse. This is probably due to high frequency components having a lower transmission coefficient for the vertical step geometry. This trend is seen on all the subsequent traces. One important difference between the two modeling techniques is that intrinsic attenuation is not taken into account in the numerical modeling. Since the low velocity composite we constructed is highly absorbent for frequencies in the ultrasonic range, the amplitudes predicted by the numerical models are consistently higher than those obtained from the ultrasonic method.

Unfilled and Filled Valleys

The lower four traces in both columns were generated by Rayleigh waves passing through filled and unfilled valleys. Both methods show the delayed Rayleigh wave and a strong shear wave arrival. It appears at first sight that the results from the numerical technique are different than those from the physical modeling, but the differences are due

to different plot scaling, as shown, by careful measurements. The shapes of the resulting seismograms are different, but the effects of the scatterer on the source pulse are generally consistent. There is one real difference between the seismograms generated by a Rayleigh wave which traveled over a valley filled with low velocity sediments. In the physical models, the peak amplitude for the filled valley is always lower than the unfilled case. The opposite is clearly true for the numerical models. We conclude that this is due to the lack of attenuation in the numerical modeling technique.

Conclusions and Predicted Effects on Regional Seismograms

All the two-dimensional scattering relationships seen in the physical modeling are also present in the numerical modeling. Different models involving the basic step geometry can be investigated quickly using the finite difference technique, and this technique has the advantage that the displacements, and therefore wavefronts, can be seen at all points in the media. The snapshot pictures aid considerably in understanding the complex scattering relationships which are present in a simple two-dimensional step geometry. Ultrasonic modeling has the advantage that the geometries to be studied need not be restricted in size or shape by available computer resources or by limitations in the existing finite difference theory. This technique also has the advantage that attenuation is incorporated into the experiment. Each has important advantages; for this reason we feel it is important to concurrently pursue both types of modeling.

Both the ultrasonic and the finite difference results indicate the importance of scattering in regional seismic propagation and allow some predictions to be made about the expected effects. For 1 Hz Rayleigh waves, such as might be found in the important regional phase Lg, the wavelength is about 3 km. Our results would predict strong attenuation and reverberation, leading to coda formation, from sedimentary basins that might reasonably be encountered. Effects of topography on such waves would not be so

great except in mountainous regions, but higher frequency (shorter wavelength) waves could be strongly affected by normal topography. The studies especially emphasise the importance of near surface low velocity materials on Rayleigh wave scattering because of the concentration of energy in the low velocity material. The results may be particularly relevant to the Nevada Test Site, which lies within basin and range type structure. Finally, the work reported here indicates why seismic station siting can have such an important effect on the character of regional events observed at different stations; in the basin and range, for example, it would be interesting to compare a station on a mesa with one off the mesa.

APPENDIX: NUMERICAL ANALYSIS

Finite Difference: Theoretical Development

Several numerical techniques are available for studying seismic wave propagation. The finite difference method is one of the most popular, as it is relatively simple to program. It is a complete solution to the wave equation, so that reflected, refracted, converted and dispersed phases are included in the solution. Although the finite difference method is valid for 1,2 and 3 dimensions, we will study two-dimensional geometries only, due to computational time and storage limitations.

The technique requires that displacements at all points in the grid be specified at two successive time increments, separated by some Δt . The displacement field is then propagated through the grid by successive discrete approximations to the wave equation. The magnitude of Δt and the distance between neighboring grid points, Δx and Δz , are strictly limited by a stability equation. Discussion of the stability equation will be postponed until a later section.

To minimize computational time and storage, artificial boundaries must be introduced along the "edges" of the grid. The correct specification of these boundary conditions is the most difficult aspect of finite difference modeling.

The Finite Difference Operator

A finite difference is simply a numerical approximation to a continuous differential operator. We will approximate the elastic wave equation, but the technique would be similar for all differential equations. It should be noted that the solution obtained by the finite difference method is not exact; there will be rounding error due to the discrete nature of the computation.

One can use the finite difference technique to obtain an approximation of the derivative for any "reasonably well defined" function $\varphi(x)$. The technique is to first write the function as a Taylor series. By expanding the function in the positive and negative directions about some point x , one can write;

$$\varphi(x + \Delta x) = \varphi(x) + \frac{\partial \varphi}{\partial x} \Delta x + \frac{1}{2} \frac{\partial^2 \varphi}{\partial x^2} (\Delta x)^2 + \frac{1}{6} \frac{\partial^3 \varphi}{\partial x^3} (\Delta x)^3 + O(\Delta x)^4 \quad (1)$$

Then, truncating the appropriate series after the second term and rearranging terms, the first order forward difference can be written as;

$$\frac{\partial \varphi}{\partial x} \approx \frac{1}{\Delta x} [\varphi(x + \Delta x) - \varphi(x)]. \quad (2)$$

Similarly, the first order backward difference is given by;

$$\frac{\partial \varphi}{\partial x} \approx \frac{1}{\Delta x} [\varphi(x) - \varphi(x - \Delta x)] \quad (3)$$

If the expansions for the forward and backwards difference are subtracted before truncation, the result is a central difference formula, accurate to second order. By virtue of sampling on both sides of the point of interest, the central difference formula is more accurate.

$$\frac{\partial \varphi}{\partial x} \approx \frac{1}{2\Delta x} [\varphi(x + \Delta x) - \varphi(x - \Delta x)] \quad (4)$$

The central difference formula for the second derivative operator, $\partial^2 \varphi / \partial x^2$, is also a second order approximation. It is most easily found by first forward differencing, then backward differencing.

$$\frac{\partial^2 \varphi}{\partial x^2} = \frac{\partial}{\partial x} \left[\frac{\partial \varphi}{\partial x} \right] \quad (5)$$

The truncated Taylor series can then be written as;

$$\frac{\partial^2 \varphi}{\partial x^2} \approx \frac{1}{(\Delta x)^2} [\varphi(x + \Delta x) - 2\varphi(x) + \varphi(x - \Delta x)] \quad (6)$$

It should be noted, as is the case with mixed continuous derivatives, the order of differencing has no effect on the outcome. Thus, equation (6) could have been obtained by backward differencing followed by forward differencing.

A more theoretical discussion of the ideas presented above is discussed in Burden et al. (1981). There are many papers on the application of the finite difference method to wave propagation problems; the work of Alterman and Karal (1968), Boore (1972), and Kelly et al. (1976) is often considered the most important early work in this discipline.

Application of the Finite Difference Method to the Elastic Wave Equation

If gravity forces are ignored, the elastic wave equation for an isotropic, inhomogeneous media is given by

$$\rho \frac{\partial^2 \mathbf{u}}{\partial t^2} = \nabla \left[(\lambda + 2\mu) \nabla \cdot \mathbf{u} \right] - \nabla \times (\mu \nabla \times \mathbf{u}) + 2 \left[(\nabla \mu \cdot \nabla) \mathbf{u} + (\nabla \mu) \nabla \cdot \mathbf{u} + (\nabla \mu) \times (\nabla \times \mathbf{u}) \right] \quad (7)$$

where ρ is density, \mathbf{u} is the displacement vector, λ and μ are Lamé's parameters and t is time. Let \hat{x} and \hat{z} be the horizontal and vertical directional unit vectors in rectangular coordinates, with \hat{z} being positive down. For the two-dimensional case in a perfectly elastic and isotropic body, the wave equation can be reduced to two coupled equations in terms u and v , the horizontal and vertical components of the displacement vector (Ewing et al., 1957):

$$\rho \frac{\partial^2 u}{\partial t^2} = \frac{\partial}{\partial x} \left[\lambda \left(\frac{\partial u}{\partial x} + \frac{\partial v}{\partial z} \right) + 2\mu \frac{\partial u}{\partial x} \right] + \frac{\partial}{\partial z} \left[\mu \left(\frac{\partial u}{\partial x} + \frac{\partial v}{\partial z} \right) \right] \quad (8)$$

$$\rho \frac{\partial^2 v}{\partial t^2} = \frac{\partial}{\partial z} \left[\lambda \left(\frac{\partial u}{\partial x} + \frac{\partial v}{\partial z} \right) + 2\mu \frac{\partial v}{\partial z} \right] + \frac{\partial}{\partial x} \left[\mu \left(\frac{\partial u}{\partial x} + \frac{\partial v}{\partial z} \right) \right]$$

These equations fully describe the motion of compressional (P) and vertically polarized (SV) waves within the media. There is no need to consider the horizontally polarized shear (SH) waves in a two-dimensional analysis because SH motion is orthogonal to both P and SV motion. This orthogonality prevents coupling of SH energy to SV and P waves.

The Homogeneous Case

If the physical properties of a medium are invariant, equation (8) can be simplified and written as

$$\frac{\partial^2 u}{\partial t^2} = \alpha^2 \left[\frac{\partial^2 u}{\partial x^2} + \frac{\partial^2 u}{\partial x \partial z} \right] + \beta^2 \left[\frac{\partial^2 u}{\partial z^2} - \frac{\partial^2 u}{\partial x \partial z} \right] \quad (9)$$

$$\rho \frac{\partial^2 u}{\partial t^2} = \alpha^2 \left[\frac{\partial^2 u}{\partial x \partial z} + \frac{\partial^2 u}{\partial z^2} \right] + \beta^2 \left[\frac{\partial^2 u}{\partial x^2} - \frac{\partial^2 u}{\partial x \partial z} \right]$$

where α and β are the P and S wave velocities, $\alpha = \sqrt{\frac{\lambda+2\mu}{\rho}}$ and $\beta = \sqrt{\frac{\mu}{\rho}}$. Since Lamé's parameters are not differentiated at each node, this form of the wave equation is much faster to compute.

For finite difference calculations, the continuous derivatives in equation (9) are replaced with their discrete counterparts:

$$\begin{aligned} u(z, x, t + \Delta t) = & 2(1 - \alpha^2 - \beta^2) u(z, x, t) - u(z, x, t - \Delta t) + \Delta t^2 \times \\ & \times [\alpha^2 (u(z, x+1, t) + u(z, x-1, t)) \\ & + \beta^2 (u(z+1, x, t) + u(z-1, x, t)) \\ & + \frac{\alpha^2 - \beta^2}{4} [u(z+1, x+1, t) - u(z+1, x-1, t) - \\ & u(z-1, x+1, t) + u(z-1, x-1, t)]] \end{aligned} \quad (10)$$

$$\begin{aligned} v(z, x, t + \Delta t) = & 2(1 - \alpha^2 - \beta^2) v(z, x, t) - v(z, x, t - \Delta t) + \Delta t^2 \times \\ & \times [\beta^2 (u(z, x+1, t) + u(z, x-1, t)) \\ & + \alpha^2 (v(z+1, x, t) + v(z-1, x, t)) \\ & + \frac{\alpha^2 - \beta^2}{4} [u(z+1, x+1, t) - u(z+1, x-1, t) - \\ & u(z-1, x+1, t) + u(z-1, x-1, t)]] \end{aligned}$$

These equations constitute an explicit finite difference scheme. That is, the displacements u and v at each point in the grid can be calculated at time step $(t + \Delta t)$

using only the displacements at the two previous time steps t and $(t - \Delta t)$.

The Inhomogeneous Case

For an inhomogeneous medium Lamé's parameters and density as well as the displacements vary spatially. Accordingly, not only displacements but also these physical properties must be differenced at all points in the grid. This adds significantly to the computational burden. For equal sized grids CPU time requirements for the inhomogeneous formulation were between two and three times greater than for the homogeneous case. To reduce run time and storage requirements we assume that density is constant everywhere in the grid. By rearranging terms, expressions involving λ and μ can be replaced by expressions involving α and β . Derivatives involving these velocity variables are solved using the chain rule. Thus,

$$\frac{\partial}{\partial x} \left[\alpha^2(z, x) \frac{\partial u}{\partial x} \right] \quad (11)$$

becomes

$$\frac{\partial \alpha^2(z, x)}{\partial x} \frac{\partial u}{\partial x} + \alpha^2(z, x) \frac{\partial^2 u}{\partial x^2} \quad (12)$$

Terms involving mixed derivatives are solved in a similar way. Evaluating equation (8) with this technique, and replacing continuous derivatives with the corresponding discrete approximations yields:

$$\begin{aligned}
u(z, x, t + \Delta t) = & 2 u(z, x, t) - u(z, x, t - \Delta t) + \Delta t^2 \times \\
& \times \left[\frac{1}{2\Delta x^2} [(\alpha^2(z, x+1) + \alpha^2(z, x))(u(z, x+1, t) - u(z, x, t)) - \right. \\
& \quad \left. (\alpha^2(z, x-1) + \alpha^2(z, x))(u(z, x, t) - u(z, x-1, t))] \right. \\
& + \frac{1}{4\Delta x \Delta z} [(\alpha^2(z, x+1) - 2\beta^2(z, x+1))(u(z+1, x+1, t) - u(z-1, x+1, t)) - \\
& \quad \left. (\alpha^2(z, x-1) - 2\beta^2(z, x-1))(u(z+1, x-1, t) - u(z-1, x-1, t))] \right. \\
& + \frac{1}{4\Delta x \Delta z} [\beta^2(z+1, x)(u(z+1, x+1, t) - u(z+1, x-1, t)) - \\
& \quad \left. \beta^2(z-1, x)(u(z-1, x+1, t) - u(z-1, x-1, t))] \right. \\
& + \frac{1}{2\Delta z^2} [(\beta^2(z+1, x) + \beta^2(z, x))(u(z+1, x, t) - u(z, x, t)) - \\
& \quad \left. (\beta^2(z-1, x) + \beta^2(z, x))(u(z, x, t) - u(z-1, x, t))] \right] \\
\end{aligned} \tag{13}$$

$$\begin{aligned}
u(z, x, t + \Delta t) = & 2 u(z, x, t) - u(z, x, t - \Delta t) + \Delta t^2 \times \\
& \times \left[\frac{1}{2\Delta z^2} [(\alpha^2(z+1, x) + \alpha^2(z, x))(u(z+1, x, t) - u(z, x, t)) - \right. \\
& \quad \left. (\alpha^2(z-1, x) + \alpha^2(z, x))(u(z, x, t) - u(z-1, x, t))] \right. \\
& + \frac{1}{4\Delta x \Delta z} [(\alpha^2(z+1, x) - 2\beta^2(z+1, x))(u(z+1, x+1, t) - u(z+1, x-1, t)) - \\
& \quad \left. (\alpha^2(z-1, x) - 2\beta^2(z-1, x))(u(z-1, x+1, t) - u(z-1, x-1, t))] \right. \\
& + \frac{1}{2\Delta x^2} [(\beta^2(z, x+1) + \beta^2(z, x))(u(z, x+1, t) - u(z, x, t)) - \\
& \quad \left. (\beta^2(z, x-1) + \beta^2(z, x))(u(z, x, t) - u(z, x-1, t))] \right. \\
& + \frac{1}{4\Delta x \Delta z} [(\beta^2(z, x+1)(u(z+1, x+1, t) - u(z-1, x+1, t)) - \\
& \quad \left. \beta^2(z, x-1)(u(z+1, x-1, t) - u(z-1, x-1, t))] \right]
\end{aligned}$$

Accuracy, Boundaries and the Source

Accuracy

Inaccuracy in finite difference calculations is primarily due to grid dispersion and inadequate stability at boundaries. If Δx or Δz is too large, the low frequency component of compressional waves will travel faster across the grid than the high frequency components. This grid dispersion is purely a numerical artifact which can be minimized by keeping grid spacings small. Grid dispersion of shear waves is much more complex. It has been shown that for some combinations of Poisson's ratio and propagation direction, high frequencies will travel faster than low frequencies (Trefethen, 1982; Bamberger et al., 1980).

Sato and Ishihara (1983) studied the effects of grid size on the velocity of various waves traveling in a finite difference grid. They found that the high frequency components in compressional waves travel more slowly than the low frequency components. For shear waves, the behavior is reversed. In addition, they observed that all waves appear to travel faster at angles near 45° to the grid. This is due to the fact that the waves are sampled less frequently as the distance between nodes becomes greater, as happens at 45° . The amount of dispersion depends also on the ratio λ/μ ; dispersion is minimized when this ratio is unity.

The magnitude of Δt has a significant effect on grid dispersion and the amount of high frequency information which is preserved. This is clearly pointed out by examining the effects of discrete differentiation on the harmonic function,

$$\varphi(t) = e^{i\omega t} \quad (14)$$

Differentiating twice yields

$$\frac{\partial^2 \varphi(t)}{\partial t^2} = -\omega^2 \varphi(t) \quad (15)$$

Using the second order central difference formula given in equation (6)

$$\frac{\partial^2 \varphi(t)^o}{\partial t^2} \approx \frac{e^{-i\omega\Delta t} - 2e^0 + e^{i\omega\Delta t}}{(\Delta t)^2} \varphi(t) \quad (16)$$

and applying trigonometric identities reduces equation(16) to

$$\frac{\partial^2 \varphi(t)^o}{\partial t^2} \approx \frac{2\cos\omega\Delta t - 2}{(\Delta t)^2} \varphi(t) = -\frac{4}{(\Delta t)^2} \sin^2\left(\frac{\omega\Delta t}{2}\right) \varphi(t) = -\hat{\omega}^2 \varphi(t) \quad (17)$$

where the apparent frequency $\hat{\omega}$ is given by;

$$\hat{\omega} = \frac{2}{\Delta t} \sin\left(\frac{\omega\Delta t}{2}\right) \approx \frac{2\omega\Delta t}{2\Delta t} = \omega \quad (18)$$

This approximation holds when $\omega\Delta t$ is small. It should be noted that for high frequencies the apparent frequency $\hat{\omega}$ becomes significantly smaller than the true value ω . Thus, high frequency waves will be dispersed more strongly than low frequency waves given the same Δt . This relationship, shown in Figure A1, indicates that frequencies greater than $1/\Delta t$ will not be adequately approximated by the finite difference technique.

The effects of the spatial grid size on stability can be investigated by analyzing the acoustic wave equation

$$\frac{1}{v^2} \frac{\partial^2 u}{\partial t^2} = \frac{\partial^2 u}{\partial x^2} + \frac{\partial^2 u}{\partial y^2} \quad (19)$$

Applying a three-dimensional Fourier Transform, we obtain

$$-\frac{\hat{\omega}^2}{v^2} = -k_x^2 - k_y^2 \quad (20)$$

Applying the second order central difference approximation to equation (19),

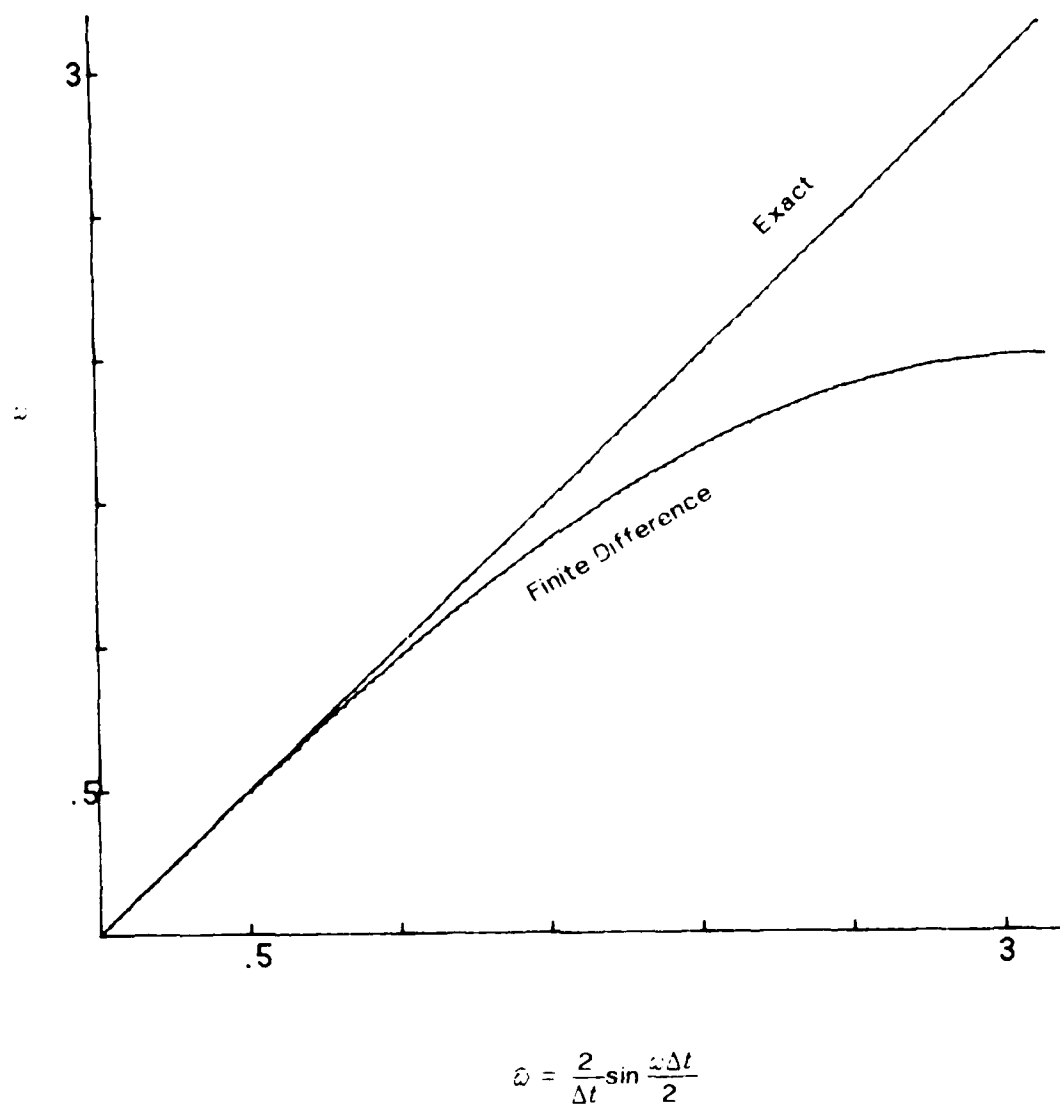


Fig A1: Plot of apparent frequency ω vs true frequency ω . An error free approximation would follow the 45° line. For admissible errors $\omega \Delta t < 1$

$$-\frac{4}{(v \Delta t)^2} \sin^2\left(\frac{\omega \Delta t}{2}\right) = -\frac{4}{(\Delta x)^2} \sin^2\left(\frac{k_x \Delta x}{2}\right) - \frac{4}{(\Delta y)^2} \sin^2\left(\frac{k_y \Delta y}{2}\right). \quad (21)$$

Rearranging terms equation (21) can be written as;

$$\sin^2\left(\frac{\omega \Delta t}{2}\right) = v^2 \frac{(\Delta t)^2}{(\Delta x)^2} \left[\sin^2\left(\frac{k_x \Delta x}{2}\right) + \frac{(\Delta x)^2}{(\Delta y)^2} \sin^2\left(\frac{k_y \Delta y}{2}\right) \right]. \quad (22)$$

Taking the maximum value of the sine as 1 and setting $\Delta x = \Delta z$, equation (22) can be rewritten as

$$\Delta t < \frac{1}{\sqrt{2}} \frac{\Delta x}{v} \quad (23)$$

For the elastic case, this relationship has to be modified slightly to include the shear wave velocity.

$$\Delta t < \frac{\min(\Delta x, \Delta z)}{\sqrt{\alpha^2 + \beta^2}} \quad (24)$$

Equations (23) and (24) are the stability conditions for two-dimensional acoustic and elastic finite difference schemes. In equation (24), α and β are taken to be the largest P and S wave velocities in the grid, Δx and Δz are the distances between grid points in the x and z directions and Δt is the time step necessary to calculate the time derivative accurately. Since the shear wave velocity is always assumed to be less than the P wave velocity, one can see that the elastic form of the stability equation is somewhat more lax than the acoustic form. These stability equations have been shown to be adequate for most explicit finite difference approximations of both the acoustic and the elastic wave equations (Kelly et al., 1976).

From the relationship between frequency, velocity and wavelength the maximum allowable grid size in a finite difference mesh is given by

$$\Delta x = \frac{V_{\min}}{n f_{\max}} \quad (25)$$

where n is the number of points per wavelength, f_{\max} is the maximum frequency, and V_{\min} is the minimum velocity value in the model (the slowest Rayleigh wave velocity occurring in the model).

One would like to maximize the number of points per wavelength in order to preserve as much high frequency information as possible. Doing so, however, forces Δt to be very small, thus increasing the number of time steps necessary to propagate a wave a given distance. This in turn increases computational time and expense. Our analysis indicated that 20 points per wavelength was sufficient to maintain adequate high frequency information for our purposes. Choosing 20 points per wavelength and $\Delta x = \Delta z = \Delta t = 1.0$ required that $\alpha \leq .7$, $\beta \leq \alpha / \sqrt{3}$.

Free Surface Boundaries

Our investigation studied the effects of crustal inhomogeneities on the passage of surface waves. Therefore, a free surface boundary at the top of our grid is needed. By definition, the normal and tangential stresses must vanish at a free surface (Ewing et al., 1957). For a horizontal free surface, this is represented by

$$(\alpha^2 - 2\beta^2) \frac{\partial u}{\partial x} + \alpha^2 \frac{\partial u}{\partial z} = 0 \quad (26)$$

and

$$\frac{\partial u}{\partial z} + \frac{\partial u}{\partial x} = 0 \quad (27)$$

To approximate the horizontal free surface, an additional row of grid points (pseudonodes) is introduced above the free surface. Displacements at the pseudonodes

are found using forward differences, while the displacements at the interior rows are determined with central differences. This will increase accuracy at the nodes within the media. The same general technique is used for vertical free surfaces, except equation (26) is rotated by $\pi/2$.

If the free surface contains 90° or 270° corners the displacements at the corner points are found using the central difference formulation and the displacements at the points adjacent to the corner points are determined using a double pseudonode. This technique is described in more detail by Fuyuki and Matsumoto (1980).

Other Boundaries

Time spent computing a finite difference grid increases rapidly as additional nodes are appended to the grid. For this reason, it is desirable to make the grid as small as possible, without interfering with the topology under study. To accomplish this objective, boundaries are needed at the edges of the grid which appear transparent to outgoing waves, and therefore prohibit inward reflections.

There are three common techniques which have been invoked to achieve the desired behavior at the boundaries. The first technique (Lysmer and Kuhlemeyer, 1969) adds a viscous damping term to the wave equation, to damp the normal and shear components of the stress tensor along the boundaries. This technique works well for compressional waves at all angles, but does not completely attenuate the reflected shear waves. An alternative method was put forth by Smith (1974), in which the full wave equation was solved twice, once with Dirichlet boundary conditions and once with Neumann boundary conditions. The two solutions are then summed to completely annihilate reflections from all incidence angles. The basis of the technique is the result that waves reflecting from zero displacement and zero stress boundaries are equal in magnitude but opposite in sign. Clearly this technique has exactly the attributes that are desired, but the computational

burden of solving the full wave equation twice at each boundary is too great. Clayton and Engquist (1977) derived a formulation which does not completely eliminate reflections from all angles, but takes only the same number of operations as a point on the interior of the grid. They used the paraxial approximation to the full wave equation to separate the in-going and outgoing components of the wave. By doing so, the in-going component can be reduced at the boundary. The combination of efficiency and adequate accuracy led us to chose the Clayton-Engquist formulation for all of our numerical experiments.

The Source

Historically, the Ricker wavelet (Ricker, 1977) has been the most common source function for numerical modeling of surface waves because the displacement field is localized in both the space and wavenumber domains. In the space domain the displacement at the free surface is depicted by Figure A2. In the wavenumber domain the spectrum for the Ricker wavelet is given by

$$S(k) = (k/k_0)^2 \exp[1 - (k/k_0)^2] \quad (28)$$

where k is wavenumber and k_0 is the maximum amplitude wavenumber. Equation (28) is shown graphically in Figure A3.

In this study we define the displacement at time zero at the free surface as the Ricker wavelet and calculate the displacements at all points below the surface using the eigenfunction for a Rayleigh wave on a half space. The source calculation was performed in the wavenumber domain and transformed to the space domain by Fourier transformation. Thus, the initial displacements for all points in the grid can be calculated from

$$u(z, x, t) = \frac{1}{2\pi} \int_{-\infty}^{\infty} E(k) S(k) dk \quad (29)$$

Here $E(k)$ is the half space eigenfunction for Rayleigh wave displacement

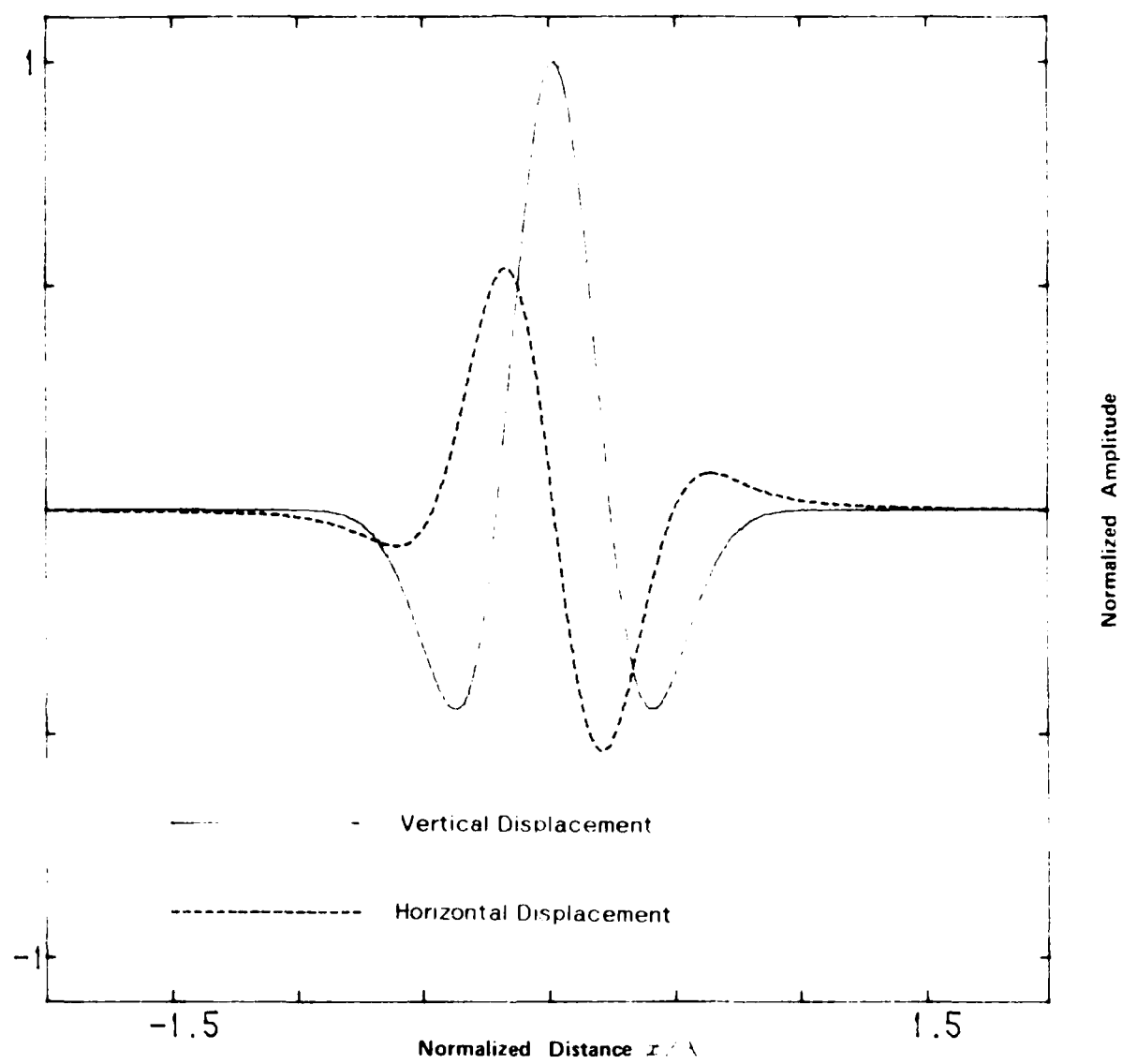


Fig A2: Ricker wavelet in the space domain.

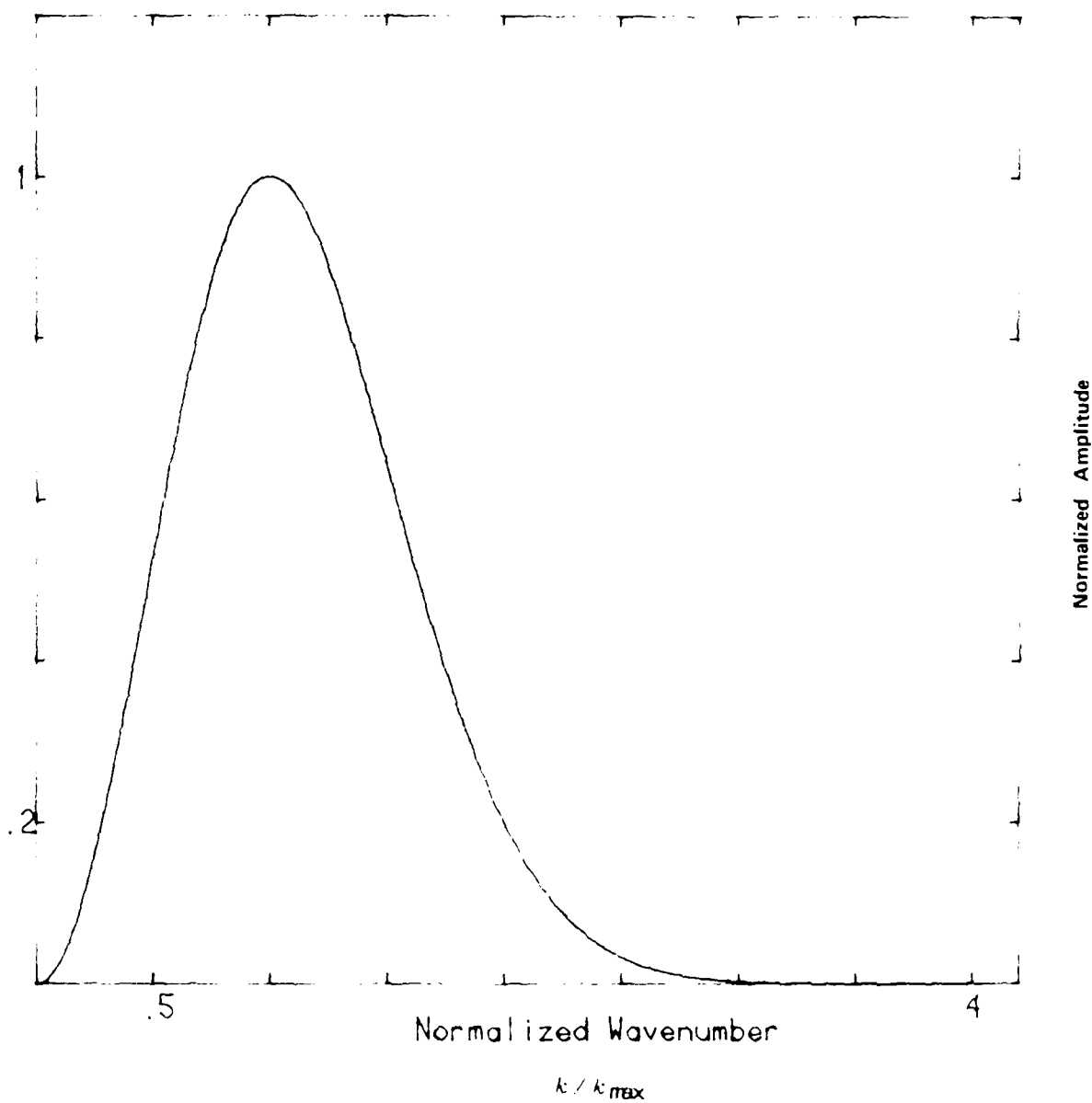


Fig A3: Ricker wavelet in the wavenumber domain.

$$E(k) = \frac{1}{k(i\bar{I} - R_c)} \begin{bmatrix} ik & kIR_s \\ -kR_c & ikI \end{bmatrix} \begin{bmatrix} \exp(-kR_c z) \\ \exp(-kR_s z) \end{bmatrix} \exp(ik(x - V_r t)) \quad (30)$$

where

$$\begin{aligned} R_c^2 &= 1 - \left(\frac{V_r}{\alpha} \right)^2 \\ R_s^2 &= 1 - \left(\frac{V_r}{\beta} \right)^2 \\ \bar{I} &= -2i \frac{R_c}{[1 - R_s^2]} \end{aligned} \quad (31)$$

\bar{I} is the forward wave impedance and V_r is the half space Rayleigh wave velocity.

REFERENCES

- Alterman, Z. and Karal F.C. 1968. Propagation of elastic waves in layered media by finite difference methods. *Bull. Seis. Soc. Am.* 58, 367-398.
- Bamberger, A., Chavent, G. and Lailly, P. 1980. Etudes de schemas numeriques pour les equations de l'elastodynamique lineaire. *Rapports de Recherche*, 41, INRIA, B.P. 105, 78150 Le Chesnay, France.
- Blandford, R.R. 1981. Seismic discrimination problems at regional distances. *Identification of Seismic Sources - Earthquake or Underground Explosion*, Husebye, E.S. and Mykkeltveit, S., Eds., D. Reidel, pp. 695-740.
- Boore, D.M. 1972. Finite difference methods for seismic waves. *Methods in Computational Physics*, v. 11, Bolt, B.A., Ed., Academic Press, New York, NY, pp. 1-37.
- Bullitt, J.T. and Toksöz, M.N. 1985. Three-dimensional ultrasonic modeling of Rayleigh wave propagation. *Bull. Seis. Soc. Am.* 75, 1087-1104.
- Burden, R.L., Faires, J.D. and Reynolds, A.C. 1981. *Numerical Analysis*, PWS Publishers, Boston, MA.
- Chamuel, J.R. 1977. Position sensing readout. U.S. Patent 4,035,762.
- Clayton, R. and Engquist, B. 1977. Absorbing boundary conditions for acoustic and elastic wave equations. *Bull. Seis. Soc. Am.* 67, 1529-1540.
- Ewing, W.M., Jardetzky, W.S. and Press, F. 1957. *Elastic Waves in Layered Media*, McGraw Hill Book Co, New York, NY.
- Fuyuki, M. and Matsumoto, Y. 1980. Finite difference analysis of Rayleigh wave scattering at a trench. *Bull. Seis. Soc. Am.* 67, 1529-1540.
- Kelly, K.R., Ward, R.W., Treitel, S. and Alford, R.M. 1976. Synthetic seismograms: a finite difference approach. *Geophysics* 41, 2-27.
- Lysmer, J. and Kuhlemeyer, R.L. 1969. Finite difference model for infinite media. *J. Eng. Mech. Div., ASCE* 95 EM4, 859-877.
- Nathman, D.R. 1980. Rayleigh wave scattering across step discontinuities. M.S. Thesis, MIT, Cambridge.
- Ricker N.H. 1977. *Transient Waves in Visco-elastic Media*, Elsevier Scientific Publishing Co., New York, NY.
- Sato, Y. and Ishihara, K. 1983. On the numerical calculation of wave propagation by the finite difference method. *Bull. Earthq. Res. Inst. Univ. Tokyo* 58, 163-173.
- Trefethen, L. 1982. Wave propagation and stability for finite difference schemes. Ph. D. Thesis, Stanford University.
- Smith, W. D. 1974. A non-reflecting plane boundary for wave propagation problems. *J. Comp. Phys.* 15, 492-503.

END

DTIC

9-86